

2p3d Resonant Inelastic X-ray Scattering of Cobalt Oxides

PhD thesis
Ru-Pan Wang

Cover design: “Lighting up the world!”
— Marte van der Linden

2p3d Resonant Inelastic X-ray Scattering of Cobalt Oxides
PhD thesis

Ru-Pan Wang
Universiteit Utrecht

ISBN: 978-90-393-7173-2
Printed by Gildeprint

2p3d Resonant Inelastic X-ray Scattering of Cobalt Oxides

2p3d Resonante Inelastische Röntgenverstrooiing van Kobaltoxiden

(met een samenvatting in het Nederlands)

Proefschrift

ter verkrijging van de graad van doctor aan de Universiteit Utrecht op
gezag van de rector magnificus, prof.dr. H.R.B.M. Kummeling, ingevolge
het besluit van het college voor promoties in het openbaar te verdedigen
op maandag 9 september 2019 des middags te 12.45 uur

door

Ru-Pan Wang

geboren op 10 september 1988 te Tainan, Taiwan

Promotor: Prof. dr. F.M.F. de Groot

This doctoral thesis was accomplished with financial support from the European Research Council (ERC Advance Grant 340279).

Contents

1	Introduction	1
2	Charge Transfer Multiplet Analysis of RIXS on Cobalt Sulfide and Halides	19
3	Spin State Competition of Co^{3+} Ions in LaCoO_3 Crystals and Films	49
4	Angular Dependence and Self-absorption of $2p3d$ RIXS in LaCoO_3	73
5	Excitonic Dispersion of the Intermediate-Spin State in LaCoO_3	91
6	Mixed-valence Cobalt Compounds	105
	Summary and Outlook	123
	Nederlandse Samenvatting	127
	Acknowledgements	131
	List of Publications	135
	About the Author	137
	Bibliography	138

Chapter 1

Introduction

The cobalt oxides and cobaltates hold plenty of charming phenomena in the fields of both chemistry and physics because cobalt ion is rich in charge, orbital, and spin degree of freedom. These charge, orbital, and spin characters drive the complex intra- and inter-atomic interactions and reflect on the electronic structure. The electronic structure is studied with various methods, including infrared radiation (IR) spectroscopy, optical absorption spectroscopy, Raman spectroscopy, and nuclear magnetic resonance (NMR). With a high brightness X-ray source available in the synchrotron, scientists can investigate the electronic structure through the X-ray spectroscopy techniques. X-ray absorption spectroscopy (XAS) and X-ray photoemission spectroscopy (XPS) provide elementary selectivity, which have made them popular. In this thesis I focus on a technique involving a *photon-in-photon-out* process, known as resonant inelastic X-ray scattering (RIXS) or resonant X-ray emission spectroscopy (RXES), to gain more insight into the electronic structure. Particularly, the Co $L_{2,3}$ -edge, in which a cobalt $2p$ -electron is excited, has been applied. This introduction is split into three parts:

- i) Introduction of RIXS.
- ii) The theory of electronic structure calculation.
- iii) The materials studied: cobalt oxides, halides and cobaltates.

1.1 $2p3d$ Resonant Inelastic X-ray Scattering

Resonant inelastic X-ray scattering (RIXS) is a technique to investigate the energy, momentum, and polarization change of the scattered photon, which provides electronic structure details of the ground state and the excited states including their charge, spin, and orbital characters. Comparing RIXS to the other techniques (such as optical absorption, Raman scattering and neutron scattering), it has unique features being photon polarization dependent, element specific, orbital specific and bulk sensitive^[1].

In this thesis, I focus on the Co $L_{2,3}$ -edge ($2p3d$) RIXS. Co $2p3d$ RIXS probes both the local and collective excitations within the $3d^n$ manifold of the cobalt cations. In the ionic limit, $2p3d$ RIXS involves a $2p^63d^n > 2p^53d^{n+1} > 2p^63d^n$ transition. In comparison with the metal $1s3d$ (pre K -edge) RIXS, the dipole-allowed $2p3d$ transition shows much stronger scattering intensity involving the $3d$ orbitals when compared to the quadruple $1s3d$ transition. This implies that $2p3d$ RIXS can probe the intra-atomic excitations within the $3d^n$ manifold of $3d$ transition metal cations, see the top panel in Fig. 1.1. These intra-atomic excitations are influenced by the electric field of its neighbors. The shell orbitals of cations can

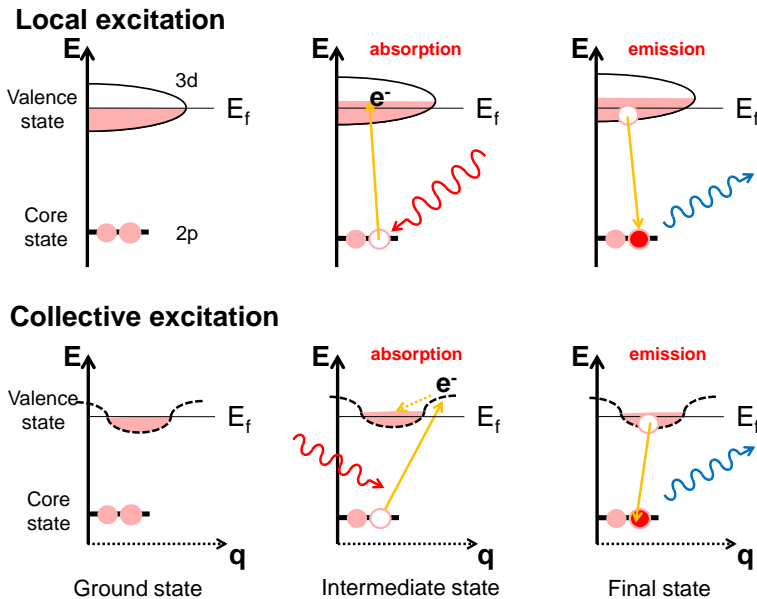


Figure 1.1: A cartoon illustration of $2p3d$ RIXS procedure. Note that core levels have no dispersion, so momentum transfer is not important for XAS.

also hybridize with the neighbors and provide the possibility of electron transfer. In addition, collective behavior of the compounds can be investigated by $2p3d$ RIXS via its momentum dependence, see the bottom panel in Fig. 1.1. The possible elementary excitations obtained by the $2p3d$ RIXS are classified as the dd excitations^[2-7], the charge transfer excitations^[5, 8-11], magnetic excitations or magnons^[12-16], vibrational excitations of molecular bonds^[17], vibrational excitations or phonons in a lattice^[18], and spin-orbit excitations^[4]. Nevertheless, such complex diversity of the features in the $2p3d$ RIXS spectra limited the global understanding on the spectra itself. In the past decade, the improvement of the instrument gives better energy resolution of the $2p3d$ RIXS to distinguish more fine structures induced by a small perturbation. It provides much deeper understanding on the fundamental properties of the material. In following subsections, I will introduce the theory of RIXS scattering cross-section and the experimental set-up.

1.1.1 The Kramers-Heisenberg Equation

The scattering cross-section of RIXS is described with the Kramers-Heisenberg equation and it is written as^[19]:

$$F_{\text{RIXS}}(\omega_{\text{in}}, \omega_{\text{out}}) = r_e^2 \frac{\omega_{\text{out}}}{\omega_{\text{in}}} \sum_f \left| \sum_m \frac{\langle f | V_E | m \rangle \langle m | V_I | g \rangle}{\omega_{\text{in}} + E_g - E_m + i\Gamma} \right|^2 \delta(\omega_{\text{in}} + E_g - \omega_{\text{out}} - E_f). \quad (1.1)$$

Here ω_{in} and ω_{out} are the energies of the incident and the emitted photons; r_e is the classical electron radius; E_g , E_f , and E_m are the eigenvalues of respectively the ground state $|g\rangle$, the final state $|f\rangle$, and the intermediate state $|m\rangle$; Γ gives the lifetime broadening of the intermediate state and V_I (V_E) is the transition operator that describes the X-ray absorption (emission).

Equation 1.1 shows that the RIXS is a *photon-in – photon-out* spectroscopy technique. The matrix elements $\langle m | V_I | g \rangle$ and $\langle f | V_E | m \rangle$ indicate the absorption and emission channels. The experimental geometry including the X-ray polarization is also encoded in the operators V_I and V_E . For $2p3d$ RIXS, the final states $|f\rangle$ in Eq. 1.1 can be represented by an excited state of $2p^63d^n$ configuration in the ionic limit, which is also indicated as $|d_\gamma(r_j)\rangle$ later. The intermediate state $|m\rangle$ is described by the $2p^53d^{n+1}$ electronic configuration. The resonant conditions ($E_g + \omega_{\text{in}} - E_m = 0$) can be met by scanning ω_{in} . This implies that RIXS can emphasize the excitation states specifically by selecting a different ω_{in} .

One can rewrite $\delta(\omega_{\text{in}} + E_g - \omega_{\text{out}} - E_f)$ in a Greens function description as $-1/\pi \times \text{Im} (\omega_{\text{loss}} + E_g - E_f + i\delta)^{-1}$. The model Hamiltonian formula of the

whole system (H) can be rewritten as^[20]:

$$F_{\text{RIXS}}(\omega_{\text{in}}, \omega_{\text{out}}) = -\frac{r_e^2}{\pi} \frac{\omega_{\text{out}}}{\omega_{\text{in}}} \text{Im} \langle g | R^\dagger(\mathbf{q}, \omega_{\text{in}}) \frac{1}{\omega_{\text{loss}} + E_g - H + i\delta} R(\mathbf{q}, \omega_{\text{in}}) | g \rangle, \quad (1.2)$$

where the $\delta \rightarrow 0$. The operator $R(\mathbf{q}, \omega_{\text{in}})$ describes local excitations from the ground state, which is given by

$$R(\mathbf{q}, \omega_{\text{in}}) = V_E \frac{1}{\omega_{\text{in}} + E_g - H + i\Gamma} V_I = \sum_j e^{i\mathbf{q} \cdot \mathbf{r}_j} V_E(r_j) \frac{1}{\omega_{\text{in}} + E_g - H + i\Gamma} V_I(r_j), \quad (1.3)$$

where V_I and V_E are expanded around each cation atom at r_j as $V_I = \sum_j e^{i\mathbf{k}_{\text{in}} \cdot \mathbf{r}_j} V_I(r_j)$ and $V_E = \sum_j e^{i\mathbf{k}_{\text{out}} \cdot \mathbf{r}_j} V_E(r_j)$. $V_{I(E)}(r_j)$ creates (annihilates) a core-hole at site r_j , and the momentum transfer is defined as $\mathbf{q} = \mathbf{k}_{\text{out}} - \mathbf{k}_{\text{in}}$. By inserting the identity matrix of the excited states, which is given by $\sum_\gamma |d_\gamma(r_j)\rangle \langle d_\gamma(r_j)|$, and applying the Fourier transform $d_\gamma(k) = 1/\sqrt{N} \times \sum_j e^{-i\mathbf{k} \cdot \mathbf{r}_j} d_\gamma(r_j)$ to the Eq. 1.2, the matrix components $R_\gamma(\mathbf{q}, \omega_{\text{in}})$ of the operator $R(\mathbf{q}, \omega_{\text{in}})$ can be described as $\langle d_\gamma(r_j) | R(\mathbf{q}, \omega_{\text{in}}) | 2p^6 3d^n \rangle$. In actual calculations with the spin-orbit coupling in the cation $3d$ shell, these states are mixed and γ represents the atomic multiplets. Basing on these modifications, the RIXS amplitude with the transferred momentum \mathbf{q} becomes:

$$F_{\text{RIXS}}(\omega_{\text{in}}, \omega_{\text{out}}, \mathbf{q}) = -\frac{r_e^2}{\pi} \frac{\omega_{\text{out}}}{\omega_{\text{in}}} \text{Im} \sum_{\gamma, \gamma'} R_{\gamma'}^\dagger(\mathbf{q}, \omega_{\text{in}}) \langle d_{\gamma'}(\mathbf{q}) | \frac{1}{\omega_{\text{loss}} + E_{\text{LS}} - H + i\delta} | d_\gamma(\mathbf{q}) \rangle R_\gamma(\mathbf{q}, \omega_{\text{in}}). \quad (1.4)$$

To calculate the RIXS cross-section, the model Hamiltonian (H) and the elements of operator matrix $R_\gamma(\mathbf{q}, \omega_{\text{in}})$ are required. $R_\gamma(\mathbf{q}, \omega_{\text{in}})$ can be obtained by using the ionic model under the experimental geometry, which explicitly includes the $3d$ - $3d$ and $2p$ - $3d$ Coulomb interaction in the full-multiplet form, the crystal field splitting ($10Dq$), and the spin-orbit coupling in the Co $3d$ shell (ζ_d) and the $2p$ shell (ζ_p).

1.1.2 Experimental Set-up

The $2p3d$ RIXS instruments

RIXS is a *photon-in–photon-out* spectroscopy technique. The monochromatic incident photon is chosen by a monochromator and the emitted photon energies

are distinguished by a spectrometer. Over the last 10 years the instrumental resolution of $2p3d$ RIXS has been improved from few thousands meV to few tens meV. Thanks to the high instrumental resolution, more fine structure can be resolved^[2, 21, 22].

In the conventional RIXS design, a better energy resolution is always associated with lower photon intensity. Solutions to increase the intensity include creating an efficient detector, enlarging the accumulation area and enhancing the incident photon intensity. An alternative design uses the concept of the energy-compensation principle^[23]. According to the energy-compensation principle, if there is a coupled monochromator-spectrometer pair with a perfect matching grating profile, the spectrometer will compensate the emitted photon with the same energy as the incident photon source to a mirrored spatial position. In order to reach the energy-compensated condition, a pair of active gratings – the monochromator active grating (AGM) and active grating spectrometer (AGS) – are used instead of the conventional fixed curvature grating both monochromator and spectrometer. An active grating can vary the surface profile to match the desired energy settings. According to the energy-compensation principle, the new design is expected to have better efficiency of the inelastic soft X-ray scattering. This design has been successfully tested at the BL05A of the Taiwan Light Source (TLS)^[24] and will be upgraded for the higher resolution application at the beamline 41A in Taiwan Photon Source (TPS)^[25].

Illustration of the experimental geometry

In RIXS experiments, the geometry is determined by the incident (emitted) photon direction, incident (emitted) photon polarization and the sample orientation. Figure 1.2a illustrates the experimental geometry with all possible angles. The two types of linear polarized incident beam are defined according to the electric field of the photon. The electric field perpendicular to the scattering plane (linear vertical to scattering plane) is defined as σ -polarization ($\epsilon_\sigma // \mathbf{k}_{in} \times \mathbf{k}_{out}$), and also indicated as V-polarization. The electric field of photon that lays in the scattering plane is defined as π -polarization ($\epsilon_\pi // \mathbf{k}_{in} \times \epsilon_\sigma$) and also indicated as H-polarization.

The scattering angle α is defined as the angle between incident and emitted photons. This angle also determine the momentum transfer vector $\Delta\mathbf{q}(= \mathbf{k}_{out} - \mathbf{k}_{in})$. The absolute value of the momentum transfer can be obtained by the Bragg equation $\frac{4\pi}{|q|} \sin\alpha/2 = n\lambda$, where $n = 1$ for first order diffraction and the λ is about 15.9 Å at the Co L -edge ($E \sim 780\text{eV}$). The total $|q|$ -value is about $0.9(\frac{\pi}{a_{cub}})$ for a

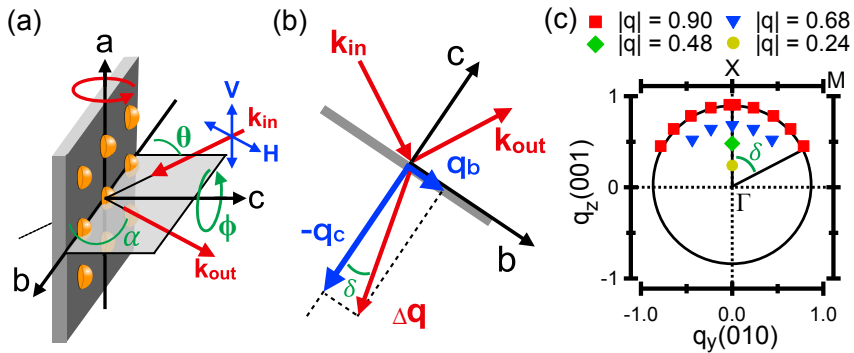


Figure 1.2: (a) Illustration of the experimental geometry. (b) Illustration of momentum projection. (c) The measured \mathbf{q} points of the experiment on LaCoO_3 (unit in $\pi/\text{\AA}$).

LaCoO_3 crystal, where $a_{cub} \sim 3.83 \text{ \AA}$ is the pseudo-lattice constant in a cubic symmetry. The angle θ describes the angle between the incident beam and the sample surface; the azimuthal angle ϕ indicates the rotation angle with respect to the sample \mathbf{c} axis. Through these definitions, an angle $\delta = 90^\circ - (\alpha/2 - \theta)$ can be obtained, which refers to the angle between the sample normal and the momentum transfer vector $\Delta\mathbf{q}$ (cf. Fig. 1.2). $\Delta\mathbf{q}$ can be expressed in the reciprocal units of the sample. Using a cubic lattice as example, the projection of the momentum vector in three axes can be written as $q_a = \Delta\mathbf{q} \times \sin\delta \sin\phi$, $q_b = \Delta\mathbf{q} \times \sin\delta \cos\phi$ and $q_c = \Delta\mathbf{q} \times \cos\delta$. Note here that the unit of the three directions is the same in a cubic symmetry. Figure 1.2c shows the example for the \mathbf{q} points which were measured for the crystal LaCoO_3 in chapter 4 and 5.

In the calculation, the orientations should be defined in a well-defined framework. I use the crystal field orientation as the universal coordinate to describe the geometry. That is, the coordinate axes will be allocated with respect to the sample orientations. Then all the other vectors will be expanded in this coordinate. Note that the polarization of the emitted photon is not analyzed in the measurements, so the calculation takes the sum of emitted photon polarizations into concern.

1.2 Electronic Structure Calculations

According to the Kramers-Heisenberg formula (Eq. 1.1), the scattering intensity of the $2p3d$ RIXS spectra is not only based on the photon geometry but also the model Hamiltonian (H) of the target system. A proper model can provide better understanding on the ground state and the excited states of the system. In this

thesis, the following theoretical models will be employed to analyze the experimental RIXS results. First, the eigenfunctions of the ionic model for a single ionized atom provides the atomic orbital basis set for multi-electron configurations. Second, crystal field theory is considered for describing the symmetry breaking due to the electric potential induced by the neighbors. Third, charge transfer theory will be used in a case that the orbital hybridization should take into account. This is related to molecular orbital theory that describes the hybridization of the cation orbital and anion orbital, which provides the insight into the chemical bonding in transition metal complexes. It is also possible to approximate the induced ligand potential not by a molecular orbital potential but by the point charge potential. The later has the similar quantities as crystal field theory. Finally, the bosonic model is used to describe the electron hopping in a lattice. The excitons in the bosonic model are allowed to travel from the central cation to the nearest cation neighbor. As such the dispersion of excitons can be calculated.

In current section, the basic concepts of the first two model will be introduced. The charge transfer effect will also be described briefly in the section. Further details about the charge transfer theory will be presented and discussed in the chapter 2 by applying the ligand to metal charge transfer (LMCT) calculation. In chapter 3 and 4, I will extend the cluster from a cube to a tetragonal symmetry, in which the beam polarization and system geometry dependence of RIXS spectra will also be demonstrated. Because a multiplet calculation requires many empirical parameters, I apply additional constraints obtained from mathematical arguments in chapter 2 and 3. The bosonic model will be used in the chapter 5 to explain the dispersive excited states.

1.2.1 The Ionic Hamiltonian

For a single ion, the Hamiltonian contains (1) the kinetic energy of the electrons, (2) the electric potential of the nucleus which is assumed as a point charge potential, (3) the spin-orbit coupling and (4) the electron-electron interactions. The Hamiltonian can be described as:

$$H_{ionic} = \sum_N \left(\frac{p_i^2}{2\mu} + \frac{-Ze^2}{r_i} \right) + \sum_N \zeta(r_i) l_i \cdot s_i + \sum_{i>j} \frac{e^2}{r_{ij}}. \quad (1.5)$$

The first term describes the motion of an individual electron in the atom without interacting to each other. The μ is the reduced mass of electron in central field approximation. The motion of an individual electron can be solved as a single

electron Hydrogen-like atom and its eigen functions are^[26]:

$$\psi_{n\ell m}(r, \theta, \phi) = \sqrt{\left(\frac{2}{na_0}\right)^3 \frac{(n-\ell-1)!}{2n[(n+\ell)!]}} e^{-r/na_0} \left(\frac{2r}{na_0}\right)^\ell L_{n-\ell-1}^{2\ell+1}\left(\frac{2r}{na_0}\right) \cdot Y_\ell^m(\theta, \phi). \quad (1.6)$$

The n , ℓ , m are the principal, azimuthal, and magnetic quantum numbers. $a_0 = \frac{4\pi\epsilon_0\hbar^2}{m_e e^2}$ is the Bohr radius and $L_{n-\ell-1}^{2\ell+1}(\dots)$ are the generalized Laguerre polynomials of degree $n - \ell - 1$. For a fermion, specifically an electron here, the total wave function Ψ of N electrons should satisfy the Pauli exclusion principle. It implies that Ψ should be antisymmetric with respect to the interchange of any two of the electrons. The total wave function Ψ can be formulated by the Slater determinant^[27, 28]:

$$|\Psi\rangle = \frac{1}{\sqrt{N!}} \text{Det}\{|\psi_a(1)\rangle|\psi_b(2)\rangle|\psi_c(3)\rangle\dots|\psi_x(N)\rangle\}, \quad (1.7)$$

where a , b etc stand for the quantum numbers necessary to specify a single electron state. In order to obtain the “best” determinant for the ground state, the variational theorem is used to minimize the expectation value of the ionic Hamiltonian (Eq. 1.5) by inserting the Slater determinant (Eq. 1.7), which is known as the Hartree-Fock method. The second term of Eq. 1.5 gives the spin-orbit coupling with a coefficient $\zeta(r_i)$. The spin-orbit interaction is the interaction of a particle’s spin with its motion inside a potential (orbit). In the $2p3d$ transition, the spin-orbit coupling in the $2p$ shell and $3d$ shell are considered. Their spin-orbit coupling coefficients are indicated as ζ_p and ζ_d , respectively.

The third term of Eq. 1.5 stands for the electron-electron interactions. Here, I rewrite Ψ with a simplified presentation, which gives:

$$|\Psi\rangle = |\dots\phi_k(i)|\phi_l(j)\dots\rangle = |i, j\rangle. \quad (1.8)$$

The k and l stand for the quantum numbers of wave function for the i -th and j -th electrons. According to the permutation rule of the Slater determinant, two cases are identified: (1) the electrons stay in their orbitals; and (2) the electrons exchange their positions. The permutations of bra and ket contribute a value $(-1)^{p+p'}$ to the expectation values, where the p and p' are the permutations of bra and ket. For the case of non-exchange electrons, $p = p'$ implies an even value of $p + p'$. So it gives a positive sign to the expectation values. In contrast, when the electrons exchange their positions, $p = p' \pm 1$ gives an odd value of $p + p'$, which implies a negative sign to the expectation values. Thus the expectation

energy of the electron-electron interaction term can be expanded as:

$$\langle \Psi | \sum_{i>j} \frac{e^2}{r_{ij}} | \Psi \rangle = \sum_{i>j} \left[\langle i, j | \frac{e^2}{r_{ij}} | i, j \rangle - \langle j, i | \frac{e^2}{r_{ij}} | i, j \rangle \right]. \quad (1.9)$$

In central field approximation, the interaction is expanded as:

$$\begin{aligned} \frac{e^2}{r_{ij}} &= [r_i^2 + r_j^2 - 2r_i r_j \cos(\omega)]^{-1/2} = \frac{1}{r_>} \left[1 + \frac{r_{<}^2}{r_>} - 2 \frac{r_{<}}{r_>} \cos(\omega) \right]^{-1/2} \\ &= \sum_k \frac{r_{<}^k}{r_{>}^k + 1} \sum_{q=-k}^k (-1)^q C_{-q}^{(k)}(\theta_1, \phi_1) C_q^{(k)}(\theta_2, \phi_2). \end{aligned} \quad (1.10)$$

Applying this expansion to Eq. 1.9 and using the Wigner-Eckart theorem, the expectation energy of the electron-electron interaction term can be rewritten in the spherical expansion as:

$$\langle \Psi | \sum_{i>j} \frac{e^2}{r_{ij}} | \Psi \rangle = \sum_k f_k F^k + \sum_k g_k G^k. \quad (1.11)$$

The F^k and G^k are wave function integrals of the radial part for the direct Coulomb repulsion and the Coulomb exchange interaction. The contributions of the angular parts are collected in f_k and g_k , which can be obtained by using the angular momentum coupling^[28, 29]. F^k is equal to G^k in the equivalent electron case of the single electron model. In addition, there is no $g_k G^k$ contribution for equivalent electrons in a multi-electron configuration, because the multi-electron wave function is already antisymmetric without coordinate permutation^[28]. Thus for equivalent electrons (the states have same quantum number n and l) only the F^k terms are preserved. The electron exchange within the $3d$ shell ($n=3$ and $l=2$) is an example of equivalent electron exchange. The total orbital angular momentum ℓ is equal to 2 and implies that $k = 0, 2, 4$ has to be concerned. Only F^2 and F^4 are affecting the $3d^n$ configurations of a $3d$ transition metal ion. On the other hand, the electron exchange between the $2p$ and $3d$ shells does not preserve the quantum character and the Coulomb exchange interaction term (G^k) should be included. This implies that five independent Slater integrals (F_{dd}^2 , F_{dd}^4 , F_{pd}^2 , G_{pd}^1 , and G_{pd}^3) are used for the $2p^5 3d^n$ configuration. These Slater integrals can be directly obtained from an optimized wave function with the Hartree-Fock approximation. The Hartree-Fock approximation always over estimates the Slater integral values and an ionic Slater integral value is usually considered to be 80% of its Hartree-Fock value^[28, 30]. The Slater integral values can also be described by the Racah

parameters B and C, where the B and C are linear combinations of F^2 and F^4 , alternatively. In the single ionic atoms, they can be expanded as $B = (9F^2 - 5F^4)/441$ and $C = 5F^4/63$ ^[27, 28]. If an external field or additional configurations is involved, the Slater integral values or Racah parameters could be modified due to the state dependent screening effect.

1.2.2 Crystal Field Theory

In solids, ions are not isolated and an effective environmental potential should be added. The Hamiltonian of an ion in an effective environmental potential can be described as:

$$H = H_{ionic} + U_{eff} + H_{int}. \quad (1.12)$$

The effective potential U_{eff} can be considered as the potential induced by the ligands in a molecular or the effective potential of a small cluster in the lattice, respectively the ligand field and the crystal field approach. Hereafter, I only discuss the effective field potential with the crystal field energy. The third term in the Hamiltonian stands for the electron-electron interaction between the central ion and its neighbors. Further discussions about H_{int} are in following chapters. In this thesis, two different approaches are applied, which are the ligand to metal charge transfer calculation (see chapter 2) and the bosonic model calculation (see chapter 5).

In a crystal, the U_{eff} is a simplified environmental potential from the superposition of the ions' potential into a smaller cluster. For this small cluster, the U_{eff} is a superposition of all the effective ligands' potential to the electron at position r_i . Assuming that all ligands are individual point charges, the effective potential can be expanded into a spherical harmonic function by Eq. 1.10. Then the $U_{eff}(r_i)$ becomes:

$$\begin{aligned} U_{ext}(r_i) &= \sum_{\alpha}^{N_{\alpha}} U_{\alpha}(r_i) = \sum_{\alpha}^{N_{\alpha}} \frac{Qe^2}{|R_{\alpha} - r_i|} \\ &= Q_{\alpha}e^2 \sum_k \frac{4}{2k+1} \times \frac{r_{<}^k}{r_{>}^{k+1}} \sum_{m=-k}^k Y_k^m(\theta, \phi)^{\dagger} Y_k^m(\theta_{\alpha}, \phi_{\alpha}) \end{aligned} \quad (1.13)$$

The Q_{α} and R_{α} in the equation are the charge number (unit in $1/4\pi\epsilon_0$) and the bond length to the central ion (units in Å) of α -th ligand ion. The N_{α} is the number of the ligands. For example, in a cubic crystal field, the $U_{eff}(r_i)$ has six ligands which are located along the six axial directions with a consistent distance. This cubic field splits the $3d$ orbitals into two groups, e_g orbitals and t_{2g} orbitals,

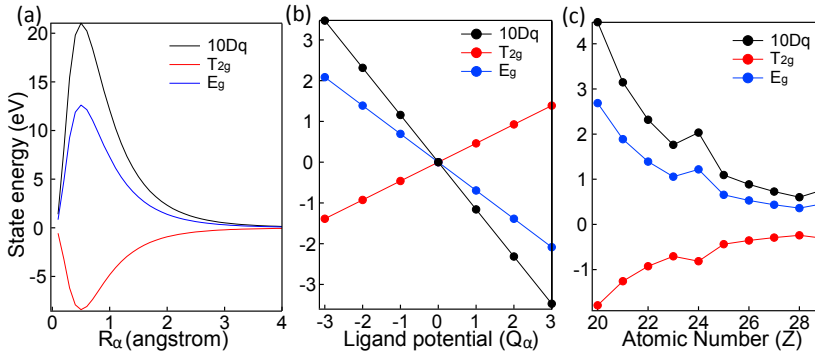


Figure 1.3: The state energy and 10Dq value as a function of (a) ligand bonding length $|R_\alpha|$, (b) ligand charge number Q_α , and (c) atomic number of central ion. The calculations were performed with an electron in $3d$ orbital (d^n , $n=1$). (a) and (b) are obtained from a Ti^{3+} ion. In (b) and (c), $|R_\alpha|=2 \text{ \AA}$.

with an energy difference defined as 10Dq. By using perturbation theory, the $U_{eff}(r_i)$ can be expanded by the wave function basis obtained above.

In the case of single electron in the $3d$ shell, the 10Dq value is proportional to Q_α and $\langle \frac{r_{<}^k}{r_{>}^{k+1}} \rangle$ using the point charge approximation. In which only if $k=4$ expectation values are found when $3d$ orbitals were concerned. There are two extreme conditions: (i) ligands condensing ($r_i \gg R_\alpha$) and (ii) weak ligand field ($R_\alpha \gg r_i$). In the first case ($r_i \gg R_\alpha$), the ligands overlap with the central ion. The $\langle \frac{r_{<}^k}{r_{>}^{k+1}} \rangle$ is replaced by $r_{<} \equiv R_\alpha$ and $r_{>} \equiv r_i$. However, this condition is not real. Most systems have a bonding length (R_α) larger than expecting $3d$ orbital position ($\langle r_i \rangle$). So the second condition ($R_\alpha \gg r_i$) is more plausible. The $r_{>} \equiv R_\alpha$ and $r_{<} \equiv r_i$ are substituted into $\langle \frac{r_{<}^k}{r_{>}^{k+1}} \rangle$ which implies that the 10Dq value is proportional to $\frac{\langle r(Z_c, R_\alpha)^4 \rangle}{|R_\alpha|^5}$. The expecting value $\langle r(Z_c, R_\alpha)^4 \rangle$ of a $3d$ orbital is proportional to $(\frac{1}{Z_c})^4$, where Z_c is the atomic number of the central ion. In summary, for the $3d$ orbitals the crystal field splitting energy 10Dq is proportional to following three factors: the electric charge number (Q_α) of ligands, a function of the bond length ($\frac{1}{|R_\alpha|^5}$) and a function of the atomic number of central ion ($\frac{1}{Z_c})^4$.

Figure 1.3a and b show the calculation results by the program MultiX^[31] for a Ti^{3+} ion ($3d^1$, $Z_c=22$). In Fig. 1.3a, the 10Dq value is presented as a function of bond length ($|R_\alpha|$). A non-trivial relation is shown in the bonding region $R_\alpha \simeq r_i$. Because of both the extreme conditions can not be applied in this region. Also, the case of identical ligands with different charge potentials was tested (Fig. 1.3b). It

shows that the 10Dq value is changed linearly with respect to the charge numbers. Figure 1.3c shows the 10Dq value as a function of Z_c . In comparison, for example, the ratio of 10Dq value between Ti^{3+} ($Z_c=22$) and Co^{8+} ($Z_c=27$) is ~ 0.31 in the calculation and ~ 0.44 from the approximation function $(\frac{1}{Z_c})^4$.

For a RIXS calculation, the elements of $R_\gamma(\mathbf{q}, \omega_{\text{in}})$ are required. These elements can be obtained by the ionic model or the crystal field model described above in conditions according to the experimental geometry. Michel van Veenendaal worked out the polarization dependence behavior of L - and M - edge RIXS by this crystal field calculation^[32]. It shows that with a selected polarization or geometry setting for the RIXS measurement, particular transitions of d -states are emphasised. The orbital selectivity and chemical site selectivity will be used and discussed in the chapters 3, 4 and 6.

1.3 The Materials: Cobalt Oxides, Cobaltates and Cobalt Halides

The cobalt ions in the cobalt oxides and cobaltates can form in a different stoichiometric as divalent (Co^{2+}), trivalent (Co^{3+}), or tetravalent (Co^{4+}) ion. In this section I introduce the general properties of the cobalt systems that will be investigated. The chapter 2 presents the electronic structure hybridization of the Co^{2+} ions in the cobalt dihalides and cobalt sulfide. The Co^{3+} system such as the LaCoO_3 crystal and films will be studied on their electronic structure within the $3d^6$ manifold in chapter 3, 4, and 5. In the chapter 6, mixed-valence compounds will be discussed based on the fundamental knowledge described in the previous chapter.

1.3.1 Binary Cobalt Oxides

The two main binary oxides are CoO and Co_3O_4 . CoO has a cubic NaCl crystal structure^[33] which implies that the Co^{2+} ions in the CoO exhibit an octahedral symmetry (O_h). It has an antiferromagnetic order transition at ~ 290 K associated with a structural transition^[33–37]. Co_3O_4 has a normal spinel structure below 850 K^[38, 39]. The spinel structure can be expressed as a formula AB_2O_4 and classified into two types which are the normal and inverse spinel structure^[40–42]. The normal spinel structure is described by the spinel MgAl_2O_4 : the A site ions contain the divalent metal ions (M^{2+}) in a crystal field induced by tetrahedral coordinated oxygen. The B site ions are formed by the trivalent metal ions (M^{3+}) in an octahedral crystal field. The inverse spinel structure, e.g. Fe_3O_4 , contains trivalent

ions in the A site and the B site have both divalent and trivalent ions. In both types of spinel structures the site occupancy is determined by factors such as the crystal field energy, bond length, charge occupancy, as well as electron hopping and configuration interaction. These quantities reflect on the electronic structure which is linked to the material properties^[39].

I investigate the mixed-valence Co ions in the Co_3O_4 through a site selective technique: Co *L*-edge RIXS. Co_3O_4 is used in applications of magneto-optical information storage^[43, 44], Li-Battery^[45], photocatalysis^[46–51], or as a visible light emitting material^[52]. The electronic structure of Co_3O_4 was characterized by optical absorption^[43, 53–57] and infrared^[58, 59]. Optical absorption finds excitation features at 0.82, 0.93, 1.64, and 2.81 eV^[54]. The infrared results show a set of excitations at ~ 0.5 eV which was assigned to the excitation features of tetrahedral Co^{2+} ions^[59]. It has been shown that, ideally, Co_3O_4 is classified as the normal spinel structure where the tetrahedral Co^{2+} holds a high-spin (HS) configuration ($S=\frac{3}{2}$) and the octahedral Co^{3+} shows the low-spin (LS) configuration ($S=0$)^[39]. The HS tetrahedral Co^{2+} is magnetically active and induces the antiferromagnetic order below 40 K^[60, 61]. The LS octahedral Co^{3+} provides no magnetism. It is noted that alternative interpretations of the spectral shapes have been proposed^[53, 55, 57, 59].

Hibberd *et al.* performed the Co *L*-edge XAS as a sensitive technique to probe the metal valence state, crystal field strength, and coordination geometry^[62]. They shown that the electronic structure of Co_3O_4 can be simulated by reference spectra of well-characterized Co-based polyoxometalates (POMs). *L*-edge XAS, however, is limited by its lifetime broadening of 200 meV and it does not measure the electron transitions within the *3d* shell (*dd* excitations), which implies that it is not sensitive enough to detect small distortions on the local environment of the Co ions, in contrast to *L*-edge RIXS^[62, 63]. From an accurate analysis of high resolution Co *L*-edge RIXS spectra, the energetic fine structure can be revealed including the small distortions^[6, 7, 63] and the *3d* spin-orbit coupling^[4]. For example, van Schooneveld and coworkers have shown that the CoO nanocrystals exhibit a smaller effective crystal field splitting and a broader ${}^4\text{T}_{1g}({}^4\text{F})$ RIXS manifold as compared to the CoO single crystal. It reveals that the small distortion on the sample surface influences the energy splitting caused by the spin-orbit coupling which potentially relates to the antiferromagnetic order^[4]. On the other hand, the Co *L*-edge RIXS has shown a high sensitivity to the crystal-field and the (super)exchange interactions including the Anderson impurity model calculations^[5]. In combination with theoretical models, these results show that Co *L*-edge RIXS can provide more details about the electronic structure of Co_3O_4 .

1.3.2 Cobalt Perovskites

Bulk LaCoO₃

LaCoO₃ is rich in its spin and orbital degrees of freedom, yielding complex magnetic and transport properties that has been studied since the 1960s^[64–66]. LaCoO₃ is a Co³⁺ perovskite with a crystal space group that changes from $R\bar{3}C$ below 650K to $R\bar{3}$ above 1200 K^[65]. In the $R\bar{3}C$ phase (< 650 K), LaCoO₃ exhibits two magnetic-electronic transitions, one near 100 K and a second near 500 K^[67–71]. The first transition switches the magnetism of LaCoO₃ from a diamagnetic phase to a paramagnetic phase^[71, 72]. At the second transition, an insulator-metal transition takes place in combination with a spin-state change^[69, 73]. Traditionally, these crossover has been described as a thermal population of excited atomic multiplets^[71, 72], where the excited atomic multiplets are determined by the competition between the crystal-field energy ($10Dq$) and the coulomb (Hund) exchange interaction energy (Δ_{ex})^[30, 74]. In a single cluster picture, the Co³⁺ in LaCoO₃ is expected to have a $10Dq$ value that is only slightly larger than Δ_{ex} . At low temperature, the nature of the diamagnetic phase in LaCoO₃ is dominated by a low-spin (LS, $S = 0$, $t_{2g}^6 e_g^0$) state. When the temperature increases above the first transition (~ 100 K), the thermal excited high-spin (HS, $S = 2$, $t_{2g}^4 e_g^2$) state of Co³⁺ is considered. Alternative theoretical models provide a similar interpretation^[75, 76]. These interpretations were supported by many experiments, including X-ray diffraction^[64, 65], X-ray spectroscopy^[77] and elastic/inelastic neutron scattering^[72, 78].

Abbate *et al.* presented the XAS and XPS results and found no difference between the spectra at 80 K and at 300 K. They found the change above 500 K and claimed that the LS-HS transition takes place at this temperature^[79]. Inspired by this result, Korotin *et al.* proposed that the transition from the LS state to an intermediate-spin (IS, $S = 1$, $t_{2g}^5 e_g^1$) can be alternative solution due to a strong cobalt-oxygen hybridization through method which combine the local density approximation with Hubbard model (LDA + U)^[80]. A generalized gradient approximation with including the Hubbard energy (GGA + U) calculation also provided a similar interpretation to a single CoO₆ cluster^[81]. In addition, a three level model (LS-IS-HS) was proposed for the properties of LaCoO₃^[82, 83]. Based on these ideas, many experimental studies claimed that they had found evidence for the existence of the IS state at this intermediate temperature region ($100 \text{ K} < T < 500 \text{ K}$)^[84–94]. But many contradictions remained. For example, the electron spin resonance result claimed the evidence of an IS spin-triplet state^[87], but a latter theoretical argument showed that it could also be assigned to a HS $^5T_{2g}$ state^[95].

Inelastic neutron scattering shows the phonon modes at about 10 and 20 meV, assigned to the LS-IS transition^[91, 93], but the observation of a 0.6 meV splitting of the 10 meV phonon indicated that the 10 meV excitation origin from the spin triplet of the HS ${}^5T_{2g}$ state^[95, 96]. A Co $2p$ X-ray absorption study^[97] showed that the spectral change indeed exists and provided the proof for a LS-HS transition scenario, in contrast to other studies^[79, 84, 94]. Other studies proposed a mixture between the IS and HS states^[98–102]. More recently, the RIXS results show that the temperature dependence behavior provides strong evidence for the LS-HS-IS transition scenario^[103].

Another related question is the deformation of Co-O bond lengths in the lattice. Based on the newest X-ray spectroscopy results^[97, 103], the LS-HS-IS (or LS-HS/LS-IS) transition scenario seems more plausible^[104–106]. A coexistence of Co ions in the excited (IS or HS) and ground (LS) states in a lattice is expected to cause a sizable disproportionation of Co-O bond lengths^[106, 107]. An antiparallel spin order (antiferromagnetism) should also exist due to the strong HS-HS (IS-IS) nearest-neighbor interactions. So far, however, most of the experimental evidence suggested no long-range magnetic order below the first spin state transition^[71, 72, 108] and proposed that the formation of a Jahn-Teller distortion induces the orbital order in combination with a homogeneous spin states^[89]. More recently, the dynamic short-range order was observed by the inelastic neutron diffuse scattering and indicated as a collective unit^[109]. Some studies^[110] claimed the presence of spin state disproportionation indirectly, but no long-range ordering was found. In addition, under high magnetic field ($B > 50$ T) conditions, the magnetization measurements of LaCoO_3 show a couple of new distinct phases that cannot be explained by the cluster model^[111, 112]. Accordingly, a new perspective has been proposed that the interactions between different electronic configurations of Co^{3+} ions are involved^[111, 113]. This interactions induce the collective behavior of IS excited states and reflect in the new observed phases^[113]. In conclusion, the experimental evidences indicates that a dynamic model is a more plausible interpretation^[109, 110]. With the $2p3d$ RIXS spectra, the local and collective excitations are probed, which provides new insights into the complex spin-state transition phenomena in LaCoO_3 .

LaCoO₃ films

A long-range ferromagnetic order has been observed in strained LaCoO_3 films^[114–118]. These materials are identified as the ferromagnetic insulators which are important components for dissipationless quantum-spin-tronic devices^[119, 120].

The origin of the ferromagnetic order in LaCoO₃ films has been proposed based on different scenarios: The first idea suggests that the tetragonal distortion bends the Co-O-Co bond angle from $\sim 163^\circ$ to 180° and increases the superexchange interaction ($2J_{ex}$)^[114, 115]. This claim was based on extended X-ray absorption fine structure (EXAFS), but other EXAFS results contradict this view point^[121]. Another possible mechanism is that the tetragonal distortion breaks the ground state symmetry and causes a competition between LS and HS Co³⁺^[121–124]. An unstrained LaCoO₃ shows a LS ($^1A_{1g}$) ground state and two cases can be considered according to the competition between the crystal field energy (10Dq) and the Coulomb interaction. There is no symmetry change if 10Dq is much larger than the crossover point (10Dq_{cross}), which implies only the LS state present. In contrast, if 10Dq is close to the crossover point (10Dq_{cross}), small distortions can induce a ground state change. Hence, the ground state of Co³⁺ is formed from a competition between three different symmetries, respectively $^5B_{2g}(D_{4h})$, $^5E_g(D_{4h})$, and $^1A_{1g}(O_h)$. The long-range ferromagnetic order has also been found in cuboidal(D_{2h}) and trigonal(D_{3d}) distorted LaCoO₃ films^[116, 117, 125].

The mechanisms above are based on the exchange interaction between LS and HS Co³⁺ ions. The strain induced magnetism seems can not explain the experimental fact that the magnetic moment per ion increases with thickness^[114, 124, 126], because above a critical thickness (h_c), the LaCoO₃ film can not sustain the substrate-imposed lattice spacing^[127]. Structural defects have been observed by scanning transmission electron microscopy (STEM)^[127–129] and one of the possible interpretations is that there exists oxygen vacancy order in the defect structures. This oxygen vacancy also implies that Co²⁺ ions could be the origin of the long-range magnetic order in LaCoO₃ films^[124, 130], because the Co²⁺ ions are always found in a magnetically active HS state. Recently, Fumega and Pardo supported this interpretation through a density functional theory calculation and proposed that the ferromagnetic state is more stable in this case^[131]. On the other hand, the defect structures can also be interpreted from a stripe structure^[128]. For a HS Co³⁺ ion, both the e_g and t_{2g} orbitals can hybridize with the oxygen ligands. This leads to the intensity change of the oxygen K -edge spectra which was observed in the STEM image^[128]. Furthermore, a recent RIXS result also shows that the HS Co³⁺ ions exist in the cuboidal(D_{2h}) and trigonal(D_{3d}) distorted LaCoO₃ films^[125]. More recently, Meng *et al.* indicated that a large amount of oxygen vacancies ($>10\%$) can strongly reduce the magnetism^[120]. In conclusion, the mechanism of the long-range ferromagnetic order in the LaCoO₃ films is still not well understood yet.

Doped LaCoO₃ systems

Elemental substitution is an alternative method to manipulate the conductivity and the magnetism of LaCoO₃. Replacing the lanthanum (La) ions with europium (Eu) ions can gradually shift the spin-state transition temperature from 100 K to a higher temperature^[69]. Another spin-state transition combined with the insulator-metal transition at the high temperature is also affected^[69]. This behavior was also observed by replacing different rare-earth ions^[92]. One of the possible explanations is a three step model which describes that the transition start from a LS ground state and passes through a LS/HS mixture phase at the middle temperature region and then to a metallic IS phase^[106]. This also implies a collective nature of the spin state transition^[106, 132]. A similar insulator-metal transition associated with the spin character change is observed in other mixed-valence cobaltites such as the heavily doped ($x > 0.2$) La_{1-x}SrCoO₃^[133, 134], La_{1-x}CaCoO₃^[135], and Pr_{1-x}CaCoO₃^[136, 137]. In this thesis, I focus on one of the newest species in the cobalt perovskite family, which is formulated as (Pr_{1-y}R_y)_{1-x}Ca_xCoO₃ (R=Nd, Sm, Eu, Gd, Tb, Y). (Pr_{1-y}R_y)_{1-x}Ca_xCoO₃ shows a magnetic transition simultaneously with the insulator-metal transition at ~ 64 K ($x=0.3$, $y=0.075$) similar to the heavily doped Pr_{1-x}CaCoO₃^[136, 138].

1.3.3 Cobalt Halides

The transition-metal dihalides MX₂ (X: F, Cl, Br) have been studied in relation to their structural phase transitions^[139–143]. The changes in bond length from fluoride to bromide are related to hybridization modifications. The inter-atomic charge transfer effect is one of the critical quantities to interpret the band gap and conductivity of the *3d* transition metal compounds^[144].

The cobalt dihalides have been chosen as prototype materials to investigate the inter-atomic charge transfer effect in the *2p3d* RIXS spectra. CoF₂ has a tetragonal rutile-type crystal structure (*P4₂/mnm*) in the ambient environment^[145–147]. By increasing the pressure, a couple of structural phase transitions have been observed^[142, 143]. CoCl₂ and CoBr₂ have a similar structure as CdCl₂ and CdI₂, respectively^[139, 145, 148]. The metal-ligand bond lengths were reported as ~ 2 Å, ~ 2.4 Å, and ~ 2.6 Å for the compound CoF₂, CoCl₂, and CoBr₂, respectively [142, 145, 147, 149]. The interatomic distances are related to the local cluster structure and the hybridization properties that they will reflect on the crystal energy and the charge transfer energies (Δ). XPS is a technique that is sensitive to the Δ value because it can probe the features induced by the screening^[150–154]. The XPS results on the transition-metal dihalides still show considerable variation^[154].

All cobalt halides were found with an antiferromagnetic order below their Néel temperatures (T_N). The T_N values of CoF_2 , CoCl_2 , and CoBr_2 are ~ 37.7 K^[155–158], ~ 25 K^[148, 159], and ~ 19 K^[148, 159], respectively. This antiferromagnetic order strongly correlates with the electric potential induced by the neighbor ions which is the consequence of the structural difference^[148, 149, 160–164]. Despite the different crystal structures, the effective electric potential induced by local environment of the cobalt ions in a single cluster can approximately be described in an octahedral symmetry^[148, 149]. The effective electric potential from the neighbors, known as the crystal field potential, was widely investigated by the optical absorption^[165–169], infrared radiation (IR) spectroscopy^[170] and Raman spectroscopy^[163, 171]. There are only few experimental results on the Co L -edge XAS spectra^[172–174] and no Co L -edge RIXS result is available for the cobalt halides. I use L -edge RIXS to refine the Δ values simultaneously with the crystal field energies (10Dq) in chapter 2.

Chapter 2

Charge Transfer Multiplet Analysis of RIXS on Cobalt Sulfide and Halides

Ligand to metal charge transfer (LMCT) is an important quantity in the discussion of the ligand-metal hybridization as well as of the electron transport properties. For a LMCT multiplet calculation, there are two main empirical parameters: the crystal field energy and the charge transfer energy. Because the $2p3d$ RIXS spectrum can provide the direct observation of the orbital excitations together with the charge transfer excitations, their relation can be discussed. In addition, I determine both the crystal field energy and charge transfer parameters of CoF_2 , CoCl_2 , CoBr_2 and CoS . They reflect the nature of the ground state electronic structure of the Co^{2+} ions with respect to symmetry and hybridization. These parameters are more accurate as those derived from X-ray absorption (XAS) and X-ray photoemission (XPS). The analysis results show that the crystal field energy decreases with increasing ligand covalency. Moreover, the L_2 -edge RIXS spectra show that the intensity of the (Coster-Kronig induced) non-resonant X-ray emission is an alternative measure of ligand covalency.

This chapter is based on the publication:

R.-P. Wang, B. Liu, R. J. Green *et al.*, “Charge-Transfer Analysis of $2p3d$ Resonant Inelastic X-ray Scattering of Cobalt Sulfide and Halides”, **J. Phys. Chem. C** **121**, 24919 (2017)

2.1 Charge Transfer Multiplet Analysis of RIXS

The ground state electronic configuration influences the intrinsic chemical and physical properties of a system, including conductivity, magnetism and chemical bonds. In the ligand-metal charge transfer (LMCT) model, the $3d$ states of a transition metal ion are assumed to be strongly correlated, where the Co^{2+} ions are approximated with a $3d^7$ ionic configuration. The $3d^7$ configuration is affected by the crystal field interaction and it interacts with the $3d^8\bar{L}$ configuration via LMCT. The LMCT model has been introduced to classify the $3d$ transition metal compounds into different types of insulators or conductors according to values of the Hubbard energy (U) and the LMCT energy (Δ)^[144]. The electronic structure can be investigated with infrared spectroscopy (IR)^[149], optical absorption spectroscopy^[74, 165–167], Raman spectroscopy^[163] and X-ray photoemission spectroscopy (XPS)^[154].

$2p3d$ resonant inelastic X-ray scattering (RIXS) is a bulk-sensitive, state and element selective measurement able to accurately investigate atomic, crystal field and charge transfer information^[5, 9, 175]. Earlier $2p3d$ RIXS experiments had energy resolutions in the range of 200 to 500 meV^[176–179], which has improved to 30 to 100 meV in recent years^[8, 180, 181]. The increased resolution implies that dd excitations and charge transfer excitations can be analyzed in more detail^[182]. In addition, the low-energy excitations (phonons and magnons) become visible, but this is not analyzed in the present chapter.

We have chosen cobalt dihalides and CoS as prototype materials to investigate the power of $2p3d$ RIXS experiments. These systems have been investigated by XPS^[150–154]. The charge transfer parameters influence the Neel temperature (T_N) and are correlated with the crystal structure^[145, 147, 148, 162, 164]. Cobalt chalcogenides are widely used as electrodes of pseudocapacitors^[183, 184], hydrogen production catalyst^[185, 186], and quantum dot sensitized solar cells^[187]. Its essential understandings, such as local atomic structure, oxidation state, or chemical composition, are complicated by various amorphous and nano-structures. Recently, Kornienko *et al.* used Raman spectroscopy and X-ray absorption spectroscopy (XAS) to investigate the amorphous cobalt sulfide catalysts^[185], but the electronic structure of the cobalt ions were not discussed in detail. We note that, unlike the cobalt dihalides, cobalt sulfides show metallic behavior^[187, 188].

In this chapter, the $2p3d$ RIXS spectra of CoF_2 , CoCl_2 , CoBr_2 and CoS compounds are analyzed systematically using the LMCT model. Although all the crystal structures are different^[145, 147, 162], the cobalt ions in these compounds are surrounded by six ligands in a (distorted) octahedral geometry^[150, 152]. From the

LMCT analysis, we derive relations between covalency, crystal field strength and peak positions.

2.2 Methodology

2.2.1 Experimental Details and Sample Preparation

Cobalt(II) fluoride (powder, >99%, $\rho=4.43 \text{ g}\cdot\text{cm}^{-3}$), anhydrous cobalt-(II) chloride (beads, -10 mesh, 99.999% trace metals basis, $\rho=3.36 \text{ g}\cdot\text{cm}^{-3}$) and anhydrous cobalt(II) bromide (beads, -10 mesh, 99.99% trace metals basis, $\rho=4.91 \text{ g}\cdot\text{cm}^{-3}$) were obtained from Sigma-Aldrich. Cobalt sulfide (powder, 99.5%, $\rho=5.45 \text{ g}\cdot\text{cm}^{-3}$) was obtained from City Chemical LLC. The powders were applied on carbon tape and attached to the sample holder in an argon atmosphere glovebox and transferred in an anaerobic environment to the RIXS measurement chamber using a dedicated transfer tool designed for the ADDRESS beamline^[189].

XAS and RIXS spectra were measured at the ADDRESS beamline of the Swiss Light Source (SLS)^[180]. The Co $2p$ ($L_{2,3}$ -edge) XAS spectra were measured through the drain current and by a photodiode for total electron yield (TEY). The incident energy scale was calibrated measuring the cobalt $2p$ XAS spectra of the cobalt monoxide powder and comparing it with literature values^[190]. The $2p3d$ RIXS spectra were measured with the use of the high resolution Super Advanced X-ray Emission Spectrometer (SAXES)^[191] of the ADDRESS beamline^[180]. A scattering geometry (cf Fig. 1.2a) was used in which the angle between the incoming light vector and the outgoing one was 90° (i.e. $\alpha = 90^\circ$). The incoming light was polarized in linear parallel mode (H-polarization) to the scattering plane with a grazing incident angle of 20° (i.e. $\theta = 20^\circ$). The total resolution of the $2p3d$ RIXS spectra were calibrated by measuring the elastic scattering of a non-cobalt containing and amorphous reference with the incoming energy from 765 to 785 eV. The combined energy resolution of the RIXS zero-loss peak was found to be 160 meV of full width at half maximum (fwhm) at the Co L_3 -edge (780 eV). The experiments were performed at room temperature and with a pressure below 10^{-9} mbar. The spectra were summed over 6 to 15 partial spectra that were acquired from 40 to 120 seconds each (varying to avoid detector saturation). The spot size of the beam was 4 by $52 \mu\text{m}^2$ and the incident flux was estimated as 5×10^{12} ph/s. Using the spectral acquisition times given in Table 2.1 and the freely available Matlab script XASskindose^[192], the skin doses for each CoF_2 , CoCl_2 , CoBr_2 , and CoS spectrum were estimated to vary between 2.0–4.5, 1.9–4.9, 0.9–3.8, and 2.5–7.8 teragray (TGy), respectively. The accumulated skin doses will be

Table 2.1: Total acquisition times for each RIXS spectrum.

Excitation energy	Total exposure time (s)					
	A	B	C	D	E	F
CoF ₂	600	600	600	600	600	600
CoCl ₂	900	400	400	350	900	900
CoBr ₂	360	450	450	450	900	900
CoS	1200	-	900	900	1200	1200

three times higher since typically two different sample spots were used to acquire spectra at six excitation energies. Sample integrity was confirmed by repeated measurements of the $2p$ XAS spectral shape.

2.2.2 LMCT Multiplet Calculations

The LMCT effect was calculated by employing the Single Impurity Anderson Model (SIAM)^[193, 194]. The SIAM can describe the interaction between configurations d^n and $d^{n+1}\underline{L}$, where an electron has been transferred from the ligand valence band while preserving spin and symmetry. The eigenstates of configurations d^n and $d^{n+1}\underline{L}$ are denoted as $|d^n\rangle$ and $|d^{n+1}\underline{L}\rangle$. They can be obtained individually by the crystal field calculation as described in the section 1.2. The charge transfer energy (Δ) is the energy difference between the two ionic configurations and the electron hopping integrals (T) describe their coupling. This coupling in SIAM yields an interacting operator H_{int} . The system Hamiltonian matrix can be described as:

$$H' = H + H_{int} = \begin{bmatrix} E(d_j^n) & T_j \\ T_j & E(d_j^{n+1}\underline{L}) + \Delta \end{bmatrix}, H_{int} = \begin{bmatrix} 0 & T_j \\ T_j & \Delta \end{bmatrix}. \quad (2.1)$$

The symbol j presents the irreducible symmetry group of the state, for example, the E_g and T_{2g} states in octahedral symmetry. The single electron orbital with respect to the states are described as e_g and t_{2g} states. The energy difference between two configurations within the same symmetry group is defined as $dE_j = E(d_j^{n+1}\underline{L}) - E(d_j^n)$. The eigenenergies ($E_{\pm,j}$) and wave functions ($|\Psi_{\pm}\rangle$) of this new Hamiltonian are:

$$E_{\pm,j} = \frac{1}{2} \left(2E(d_j^n) + dE_j + \Delta \pm \sqrt{(dE_j + \Delta)^2 + 4T_j^2} \right), \quad (2.2)$$

$$\text{and } |\Psi_{\pm,j}\rangle = \alpha_{\pm,j}|d_j^n\rangle + \beta_{\pm,j}|d_j^{n+1}\underline{L}\rangle. \quad (2.3)$$

The solution with a negative (positive) sign has a lower energy and corresponds to the bonding (anti-bonding) state. The wave functions were simplified as $|\Psi_{GS}\rangle = \alpha|d^n\rangle + \beta|d^{n+1}\underline{L}\rangle$ with an eigenenergy E_{GS} . The value $dE_j + \Delta$ can be defined as an effective charge transfer energy Δ_{eff} . The energy difference between bonding and anti-bonding states of the same orbital symmetry is approximately linear to Δ_{eff} . The hybridization percentages of the two states are obtained from $|\alpha_{\pm}|^2$ and $|\beta_{\pm}|^2$. However, more generally, the multi-electron configuration should be concerned. The actual states will be linear combinations of few configurations with different orbital symmetries. In an octahedral symmetry, the strong field configuration projections can be described in terms of e_g and t_{2g} orbitals. For a Co^{2+} ion in an octahedral field, the bonding state of configuration yields:

$$|\Psi_{-}\rangle = \sum \alpha_{-,s} |e_g^{7-s} t_{2g}^s\rangle + \sum \beta_{-,t} |e_g^{8-t} t_{2g}^t \underline{L}\rangle, \quad \text{and} \quad (2.4)$$

$$\begin{cases} P(d_i^7) &= |\alpha_{-}|^2 = \sum_{6 \geq s \geq 3} |\alpha_{-,s}|^2 = P(e_g^{7-s} t_{2g}^s) \\ P(d_i^8 \underline{L}) &= |\beta_{-}|^2 = \sum_{6 \geq t \geq 4} |\beta_{-,t}|^2 = P(e_g^{8-t} t_{2g}^t \underline{L}). \end{cases} \quad (2.5)$$

Where the indices s and t are the number of electrons in the t_{2g} states and P gives the corresponding population of the states. As mentioned above, the actual states will be linear combinations of $e_g^{7-s} t_{2g}^s$ configurations due to multiplet effects and spin-orbit coupling. From this, the covalency of the e_g and t_{2g} states can be calculated from these electron distributions.

According to the Eq. (2.2), the difference between two states with different symmetry group k and l is given by:

$$\Delta E_{l-k} = \frac{1}{2} \left\{ \Delta E(10Dq_{ion}) - \left(\sqrt{(dE_k)^2 + 4T_k^2} - \sqrt{(dE_l)^2 + 4T_l^2} \right) \right\} \quad (2.6)$$

, where

$$\Delta E(10Dq_{ion}) = 2E(d_k^n) - 2E(d_l^n) + dE_k - dE_l. \quad (2.7)$$

In a single electron model, k and l are replaced by e_g and t_{2g} states, respectively. The energy difference between e_g and t_{2g} states is defined as a crystal field splitting energy ($10Dq_{eff}$). So ΔE_{l-k} can be defined as $\Delta E(10Dq_{eff})$. In addition, the term $2E(d_k^n) - 2E(d_l^n) + dE_k - dE_l$ is defined as $\Delta E(10Dq_{ion})$, which is the energy difference of the ionic states and is determined only by a given ionic crystal field splitting energy ($10Dq_{ion}$). Subtracting this ionic contribution from $\Delta E(10Dq_{eff})$ and replacing k as e_g and l as t_{2g} , yields a part that remain dependent on Δ . Thus, energy difference can be rewritten as:

$$\Delta E_{CT}(\Delta) = \frac{1}{2} \left\{ \sqrt{(dE_{t_{2g}} + \Delta)^2 + 4T_{t_{2g}}^2} - \sqrt{(dE_{e_g} + \Delta)^2 + 4T_{e_g}^2} \right\}. \quad (2.8)$$

Equation (2.8) shows an extra energy difference between e_g and t_{2g} states and implies that the crystal field of our system is affected. In a weak charge transfer system (i.e., $\Delta \gg |T_{t_{2g}}| \simeq |T_{e_g}|$), the value of ΔE_{CT} is negligible. Under these conditions, this system can be treated as ionic case. More general, all the $e_g^{7-s}t_{2g}^s$ configurations should be considered in a multi-electron model. Equation (2.8) would be extended with more Δ -depending terms. Nevertheless, a linear function can approximate this relation when the energy difference is small. As a result, the effective splitting energy ($10Dq_{eff}$) between the t_{2g} and the e_g states is dependent on the Δ . From this, it follows that expression 2.6 can be rewritten as:

$$\Delta E(10Dq_{eff}) = \Delta E(10Dq_{ion}) + \Delta E_{CT}(\Delta). \quad (2.9)$$

2.2.3 RIXS Spectra Simulation Procedure

Recalling the Kramers-Heisenberg formula in the matrix format (Eq. 1.1), the RIXS scattering cross-section is written as^[5, 191]:

$$F_{\text{RIXS}}(\omega_{\text{in}}, \omega_{\text{out}}) = r_e^2 \frac{\omega_{\text{out}}}{\omega_{\text{in}}} \sum_f \left| \sum_m \frac{\langle f|V_E|m\rangle \langle m|V_I|g\rangle}{\omega_{\text{in}} + E_g - E_m + i\Gamma} \right|^2 \delta(\omega_{\text{in}} + E_g - \omega_{\text{out}} - E_f) \quad (2.10)$$

For $\text{Co}^{2+} 2p3d$ RIXS, the state vectors $|g\rangle$, $|m\rangle$, and $|f\rangle$ refer to the configurations $2p^63d^7$, $2p^53d^8$ and $2p^63d^7$, respectively. If the LMCT hybridization is included, the initial ground state $|g\rangle$ becomes the linear combination between the ionic configuration ($3d^7$) and configuration with ligand hole ($3d^8\bar{L}$). Using incident energies at various energies of the L_3 -edge, it is possible to analyze the details of the dd excitations and the charge transfer excitations in the $2p3d$ RIXS spectra^[5, 9, 175].

LMCT calculations were used to study the $2p$ XAS and $2p3d$ RIXS spectral shapes^[175, 195, 196]. A modified version of the code was applied to obtain exact solutions of the charge transfer Hamiltonian^[197]. XAS calculations were performed with CTM4XAS^[198]. The charge transfer RIXS calculations were performed with the use of a dedicated Matlab program^[199]. CTM4DOC was used to project the states to their individual basis and to analyze the expansion coefficients in terms of different basis sets^[200]. The experimental $2p3d$ RIXS spectra were measured with a H-polarized incident beam and a 90° scattering geometry. This setting was simulated as the sum of $[V_{\text{in}} \text{ to } H_{\text{out}}]$ and $[H_{\text{in}} \text{ to } V_{\text{out}}]$ polarizations for powder samples, because $\varepsilon_{\text{in}} \cdot \varepsilon_{\text{out}} = 0$ when scattering angle at 90° .

We remark that two important phenomena in RIXS are correlated with the LMCT hybridization within a $3d$ transition metal ion: (a) the ligand hybridization

influences the metal t_{2g} and e_g states differently^[175]; and (b) bonding and anti-bonding states between original ionic states $|d^n\rangle$ and ligand hole states $|d^{n+1}\underline{L}\rangle$ are created that give rise to respectively the dd excitations and charge transfer excitations^[5, 175]. According to the relation Eq. 2.6 and 2.9, these two phenomena can be discussed in terms of (a) the crystal field energy $10Dq$ and (b) the charge transfer energy Δ .

In order to discuss these phenomena, the $2p3d$ RIXS spectra were simulated according to following general procedure:

- (1) We calculate the atomic parameters for the Co^{2+} ion, using the common approach in CTM4XAS of using 80% of the Hartree-Fock calculated values for the Slater integrals plus the spin-orbit couplings as calculated for the free ion.
- (2) We use the $2p3d$ RIXS spectra of each compound to determine the value of $10Dq$.
- (3) We use the $2p3d$ RIXS spectra of each compound to determine Δ .
- (4) Keeping the optimized $10Dq$ and Δ , the atomic parameters were optimized to obtain the best fit for both the $2p$ XAS and all $2p3d$ RIXS spectra, where the same parameters are used for all four systems.

The final experimental and simulated results will be presented in the coming two section. In addition, the details on determination of the simulation parameters according to these general procedure will also be discussed there.

2.3 Results

2.3.1 Experimental $2p3d$ XAS and RIXS Spectra

Figure 2.1-2.4 demonstrate the experimental and simulated results. The top panels of them are the $2p$ XAS spectra for CoF_2 , $CoCl_2$, $CoBr_2$, and CoS , respectively. All four spectra show the clear signature of a 4T_1 high-spin Co^{2+} ground state, equivalent to CoO ^[4, 5]. One can observe that the multiplet states are more and more compressed in the series $CoF_2 < CoCl_2 \sim CoBr_2 < CoS$. To measure the $2p3d$ RIXS spectra, the incident photon energies were selected according to the $2p$ XAS spectra and labelled with capital symbols A-G as illustrated in figures. These chosen incident energies correspond to the different peaks/features of the XAS spectra, as indicated in the figures. The incident energies A to F correspond to the L_3 ($2p_{3/2}$) edge. At the L_2 ($2p_{1/2}$) edge, only the energy G was selected for the $2p3d$ RIXS measurements. In the case of CoS the multiplet states are compressed, which makes peak B invisible and therefore no $2p3d$ RIXS was measured

at energy B for CoS.

The bottom panels are the experimental and the LMCT simulated $2p3d$ RIXS spectra, where the intensity of the simulation was normalized to the first dd excitation at approximately 0.7 eV. For CoF_2 a series of sharp features are observable over the whole energy range from 0.0 to 9.0 eV. In fact the peaks continue above 9.0 eV, but the spectra are limited to this energy range to make the low-energy peaks better visible. CoBr_2 and CoS also contain the same series of sharp peaks, but they are limited to the range between 0.0 and 3.0 eV. Between 3.0 eV and 7.0 eV broader features are visible. The $2p3d$ RIXS final states relate to excitations of the ${}^4\text{T}_1$ Co^{2+} ions. One can make a direct comparison to optical spectroscopy and relate the sharp peaks with dd excitations and the broad peaks with charge transfer excitations. A difference with optical spectroscopy is that the dd excitations are dipole forbidden in direct optical absorption, which makes them weak in intensity^[74, 165–167]. But $2p3d$ RIXS is a dipole excitation plus dipole decay transition, the dd excitations are stronger and sharper in intensity than the charge transfer excitations. This behavior is clearly observed on the RIXS spectra of CoF_2 and CoCl_2 .

2.3.2 Simulated $2p3d$ XAS and RIXS Spectra

The simulations were performed according to the procedure as described in last section. Based on the simulations, we analyzed the nature of the excitation states of the $3d^7$ configuration that are given with their Mulliken group symbols in Fig. 2.1-2.4. These state energies obtained from experiments and simulations are listed in Table 2.2. The yellow blocks in the figures indicate the region of the charge transfer excitations, where a large charge transfer energy Δ shifts them to higher excitation energies. They have been indicated as ${}^3\text{A}_2$ states and the states with an energy higher than it (Table 2.2). The charge transfer peaks provide a determination for the hybridization information and will be further discussed in section 2.3.5 and 2.4.2. In general, the energy and shape of the excitations are well reproduced, especially in the first 2 eV. The peaks at higher excitation energies above 3.0 eV were not simulated as accurate, which is related to the approximations to the $3d^8\bar{\text{L}}$ charge transfer band due to limitations in computer power. The full charge transfer band has been approximated with three charge transfer states instead of a band that yields sharp features at energies above 3.0 eV.

The spectral features were resonating differently with varying incident photon energies according to the Kramers-Heisenberg formula. At energies A to E, the dd excitations of the spin quartet states (${}^4\text{T}_1$, ${}^4\text{T}_2$, ${}^4\text{A}_2$) dominated the spectra. For

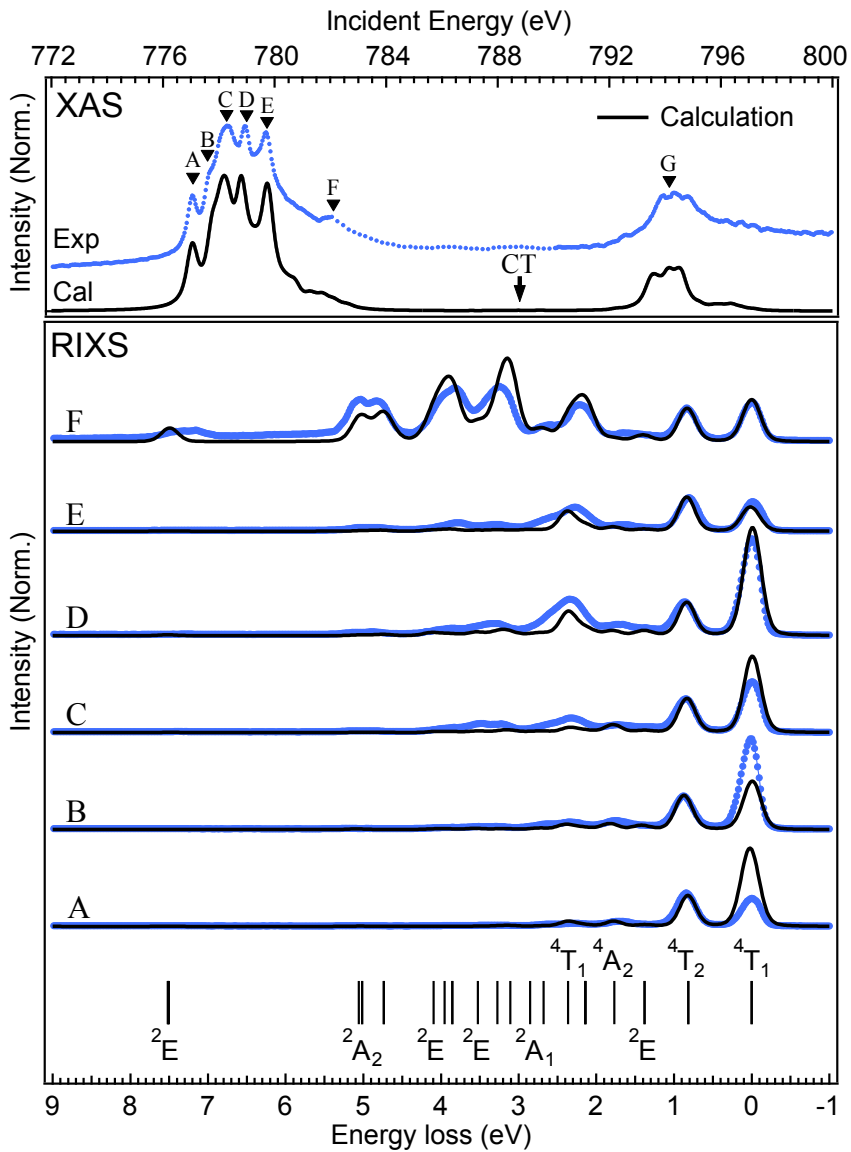


Figure 2.1: The experimental and simulated spectra of CoF_2 . The top and bottom panels are the $2p$ XAS and $2p3d$ RIXS spectra, respectively. The black sticks are indicated the states energies in term of Mulliken group symbols.

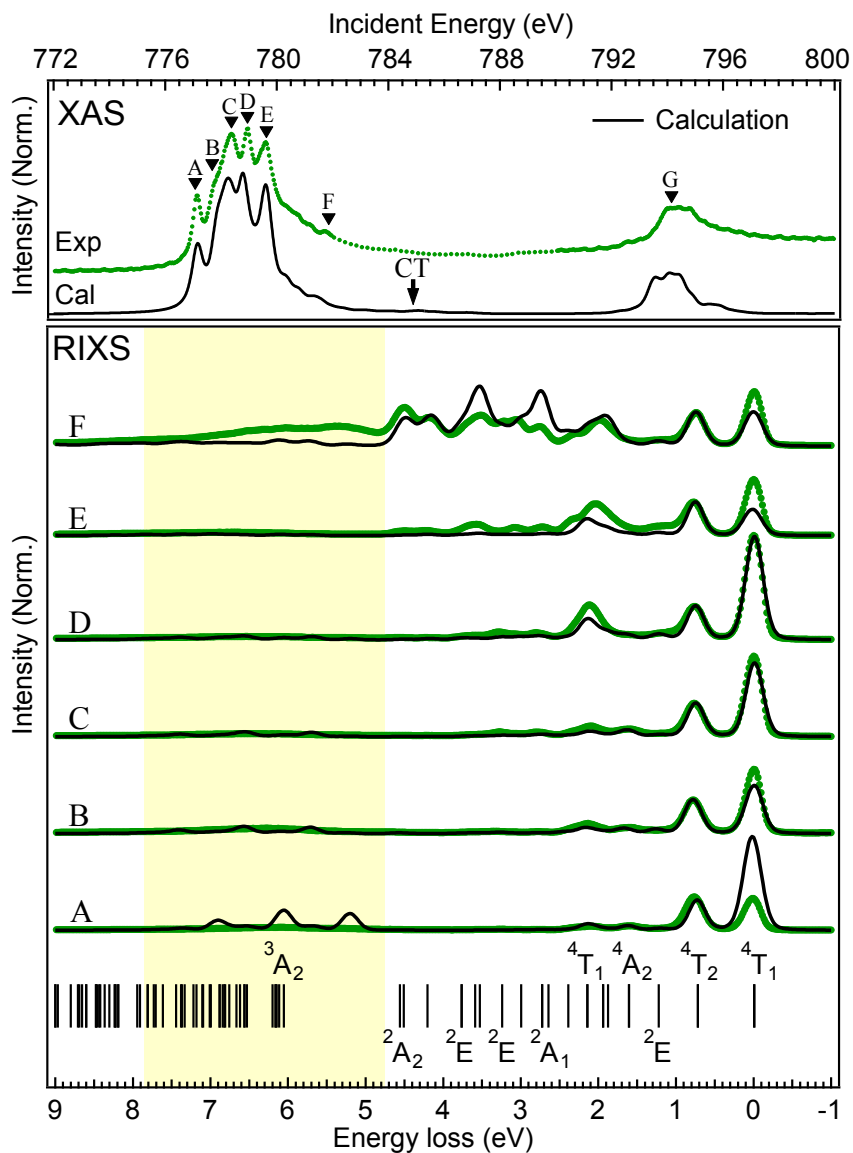


Figure 2.2: The experimental and simulated spectra of CoCl_2 . The top and bottom panels are the $2p$ XAS and $2p3d$ RIXS spectra, respectively. The black sticks are indicated the states energies in term of Mulliken group symbols.

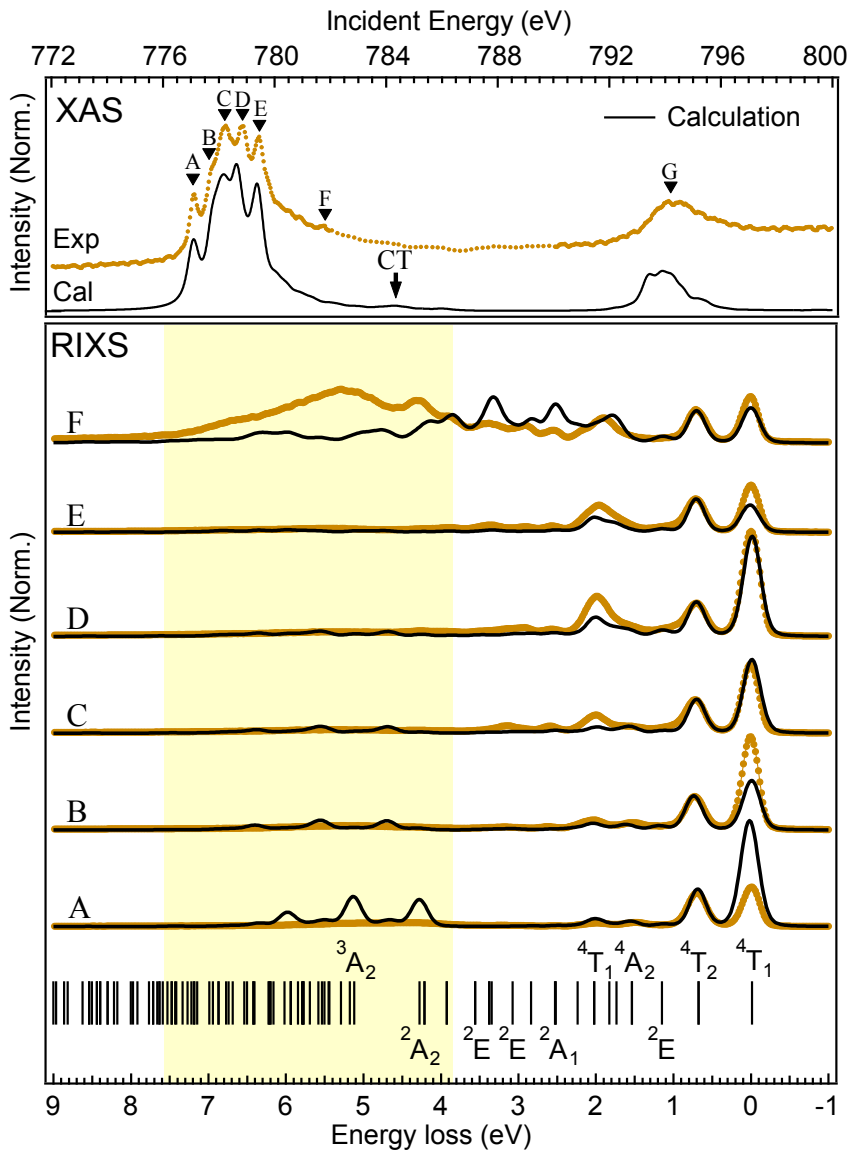


Figure 2.3: The experimental and simulated spectra of CoBr_2 . The top and bottom panels are the $2p$ XAS and $2p3d$ RIXS spectra, respectively. The black sticks are indicated the states energies in term of Mulliken group symbols.

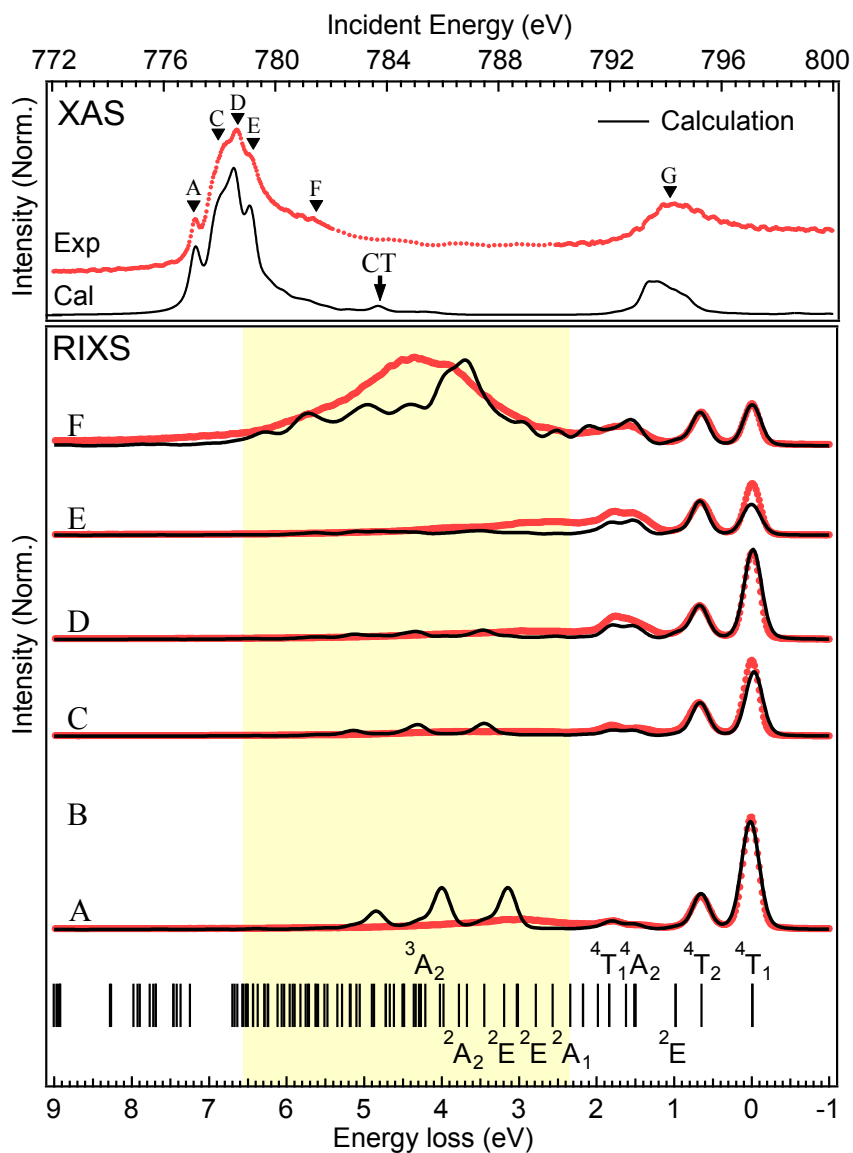


Figure 2.4: The experimental and simulated spectra of CoS. The top and bottom panels are the $2p$ XAS and $2p3d$ RIXS spectra, respectively. The black sticks are indicated the states energies in term of Mulliken group symbols.

Table 2.2: The RIXS state symmetry term labels and energies (in eV) derived from experiments and calculations.

	CoF ₂		CoCl ₂		CoBr ₂		CoS	
	Exp	Cal	Exp	Cal	Exp	Cal	Exp	Cal
Quartet								
⁴ T ₁	0.00	0.00	0.00	0.00	0.00	0.00	0.00	0.00
⁴ T ₂	0.85	0.81	0.77	0.72	0.71	0.68	0.67	0.65
⁴ A ₂	1.71	1.76	1.60	1.61	1.52	1.54	1.44	1.51
⁴ T ₁	2.27	2.35	2.11	2.14	1.98	2.02	1.79	1.83
Doublet								
² E	1.33	1.37	1.21	1.22	1.11	1.15	-	0.98
² T ₁	-	2.13	-	1.93	-	1.83	-	1.62
² T ₂	-	2.13	-	1.87	-	1.74	-	1.49
² T ₁	2.63	2.67	2.25	2.38	2.15	2.20	-	1.98
² A ₂	-	2.84	-	2.63	-	2.51	-	2.33
² T ₂	-	3.09	2.76	2.72	2.59	2.52	2.13	2.16
² T ₁	3.25	3.26	3.10	2.98	2.94	2.83	2.59	2.56
² E	3.50	3.51	3.24	3.23	3.15	3.06	-	2.77
² T ₂	-	3.84	-	3.51	-	3.33	-	3.01
² T ₁	3.84	3.94	3.57	3.57	3.38	3.36	2.98	3.00
² E	-	4.08	-	3.74	-	3.54	3.19	3.18
² T ₂	4.88	4.72	4.12	4.18	3.95	3.91	-	3.43
² T ₁	-	4.99	4.49	4.46	-	4.19	-	3.65
² A ₂	5.15	5.04	4.63	4.54	4.30	4.25	-	3.76
² E	7.30	7.47	5.40	-	-	-	-	-
LMCT								
³ A ₂	11.50	11.26	6.12	6.11	5.30	5.30	3.94	4.20

example, at the energy A, mainly the 1.7 eV feature (⁴A₂ states) contributes the intensity in CoF₂(Fig. 2.1). Whereas, other possible states, the spin doublet states (Table 2.2), can be observed with a higher incident energy. For instance, a feature about 1.3 eV is appeared at energy F in CoF₂. This new appearing feature is the ²E states of the d⁷ configuration. Similar behavior can also be observed for CoCl₂ and CoBr₂(Fig. 2.2 and 2.3)). By comparing the features between the spectra at different incident energies, more orbital information can be obtained. With Fig. 2.5 we emphasize this excitation selectivity. At incident energies A, B, C, D and E, the 0 to 2 eV excitations dominate, but at incident energy F more intensity

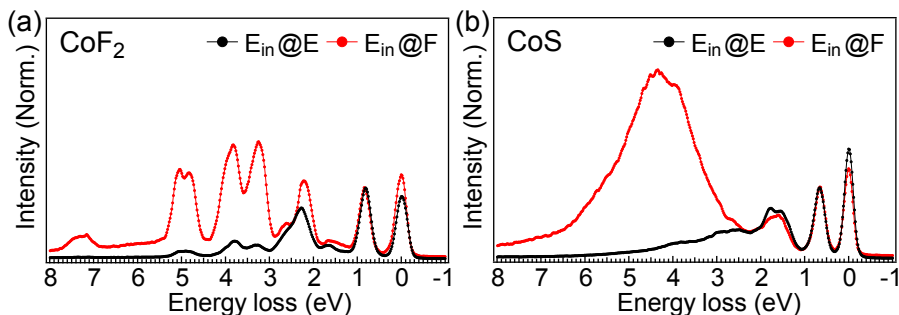


Figure 2.5: Experimental results at incident energies E and F of (a) CoF_2 and (b) CoS .

is found at the higher excitations energies. In the case of CoF_2 , the spectra at energy F gives dd excitations in the whole energy loss region between 0 and 8 eV (Fig.2.5a). In comparison, the spectra at energy F of CoS shows a large and broad feature at about 4 eV (Fig. 2.5b), which should not be the localized orbital excitations. This broad feature now is assigned to charge transfer excitations.

2.3.3 General Simulation Conditions

All LMCT calculations were performed in C_4 symmetry at 300 K using a small exchange field ($M \sim 2$ meV) to take the anti-ferromagnetic order ($T_N \sim 10-40$ K) into account^[148, 162, 164]. The 300 K results were calculated by considering the first six energy states and summing them with a Boltzmann distribution weighting. Because of the contraction of the $3d$ wave function due to the core hole, the 10Dq value is reduced with 15% for the intermediate state^[201]. The charge transfer parameters include the charge transfer energy Δ , the Hubbard Coulomb repulsion between the $3d$ electrons U_{dd} (U), the core hole potential U_{pd} (Q), and the electron hopping parameters T . In this work, the parameters were fixed by using $U = 6$ eV, $Q = 7$ eV, $T_{t_{2g}} = 1$ eV, and $T_{e_g} = 2$ eV. Note that $2p$ XAS and $2p3d$ RIXS are not sensitive to the values of U and Q , but only to their energy difference. For Co^{2+} , only $3d^7$ and $3d^8\bar{L}$ configurations were considered in the calculations. The $3d^9\bar{L}^2$ and $3d^{10}\bar{L}^3$ configurations were neglected when reproducing the $2p$ XAS and the $2p3d$ RIXS spectral shapes^[63]. In addition, the charge transfer excitations are a “band-like” features and consequently broadened by a width W . In simulation, the best simulated W was 2.2 eV obtained from the center of mass of the antibonding states. Due to limitations in calculating power, only 3 splitting states were considered to calculate W instead of a band (infinite states should be considered). For

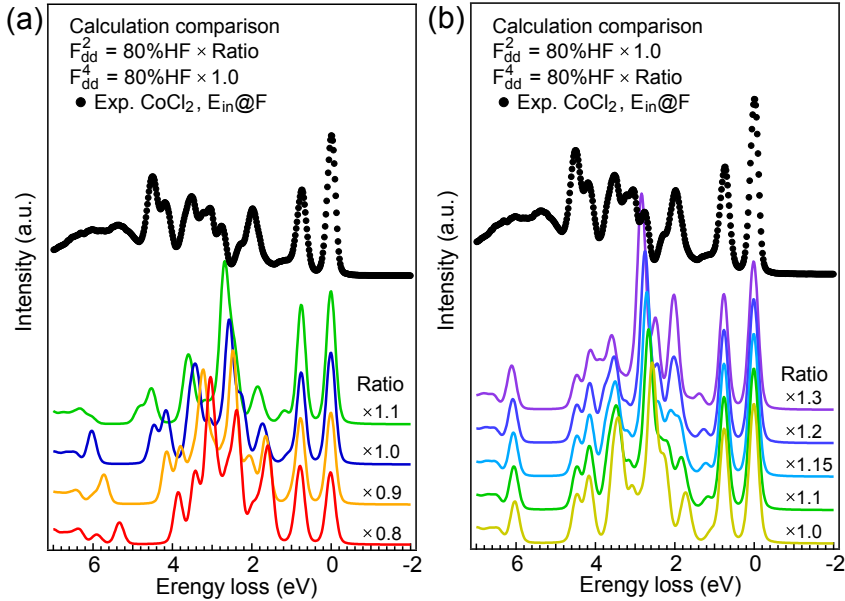


Figure 2.6: The optimization process of F_{dd}^2 and F_{dd}^4 (target on RIXS spectra of CoCl₂). (a) Fixed F_{dd}^4 and free the F_{dd}^2 values. (b) Fixed F_{dd}^2 and free the F_{dd}^4 values.

Table 2.3: The Slater integral and spin-orbit coupling energies in the simulation (in eV).

	F_{dd}^2	F_{dd}^4	F_{pd}^2	G_{pd}^1	G_{pd}^3	ζ_p	ζ_d
$2p^6d^7$	9.470	6.805	-	-	-	-	0.066
$2p^6d^8\bar{\underline{L}}$	8.512	6.072	-	-	-	-	0.059
$2p^5d^8$	10.115	7.276	6.389	4.318	2.701	9.748	0.083
$2p^5d^9\bar{\underline{L}}$	-	5.830	3.895	3.895	2.435	9.750	0.075

example, 3 separated peaks about 3, 4, 5 eV appear in the calculation results for CoS (Fig. 2.4). These 3 states can represent the LMCT effect on the lowest, the central, and the highest edge of the band.

In the $2p3d$ RIXS spectra, the combination of (a) its 160 meV resolution, (b) the multiple resonant spectra and (c) the large number of spectral features, allows for a further refinement of the atomic interaction parameters. As described in subsection 2.2.3, the initial calculations were performed with atomic Slater integrals, defined as 80% of their Hartree-Fock value. Keeping the $10Dq$ and Δ

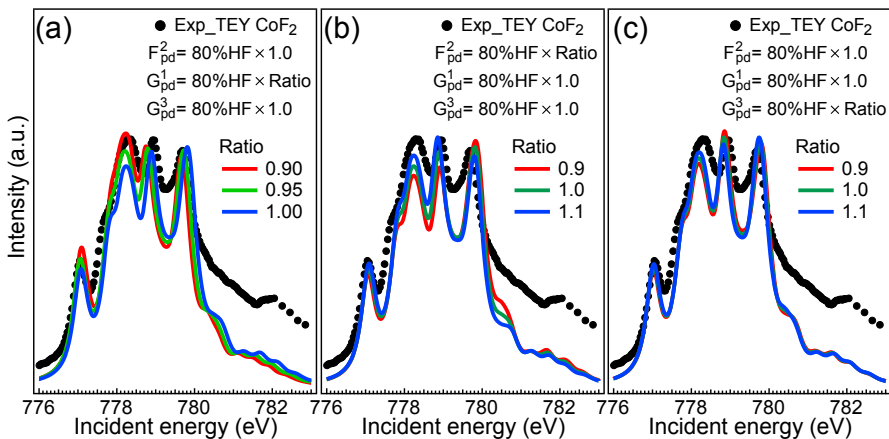


Figure 2.7: The optimization for F_{pd}^2 , G_{pd}^1 , and G_{pd}^3 values (target on XAS spectra of CoF_2). The panels focus on finding the value of (a) G_{pd}^1 , (b) F_{pd}^2 , and (c) G_{pd}^3 .

Table 2.4: The first dd excitation energy with respect to $10Dq_{ion}(=10Dq_{eff})$.

$10Dq_{ion}$	4T_1	$10Dq_{ion}$	4T_1	$10Dq_{ion}$	4T_1	$10Dq_{ion}$	4T_1
0.3	0.32	0.6	0.57	0.9	0.83	1.2	1.13
0.4	0.39	0.7	0.65	1.0	0.93	1.3	1.18
0.5	0.47	0.8	0.75	1.1	1.01		

values obtained above, the atomic parameters were optimized to obtain the best fit for both the $2p$ XAS and all $2p3d$ RIXS spectra, where the same parameters are used for all four systems. Figure 2.6 shows the simulation processes for searching the F_{dd}^2 and F_{dd}^4 , which were optimized as 82% and 94% of the Hartree-Fock values, respectively. On the other hand, the F_{pd}^2 , G_{pd}^1 , and G_{pd}^3 were optimized according to $2p$ XAS and the values are 88%, 80%, and 88% of the Hartree-Fock respectively (Fig. 2.7). These optimized values are given in Table 2.3, where we note that in O_h symmetry the exchange interaction for e_g and t_{2g} states is not exactly the same^[202]. The F_{dd}^2 and F_{dd}^4 are not necessarily reduced by the similar reduction values due to the state dependent screening effect.

The lifetime of the $2p$ core states is approximately constant for the L_3 -edge^[203, 204] and the lifetime broadening (L) of the $2p$ core hole is approximately 0.4 eV fwhm^[5, 205]. The final states of $2p3d$ RIXS relate to dd excitations that are known from optical spectroscopy^[74, 165–167]. The lifetime of the dd excitations varies depending on the spin state. We use a broadening of 50 meV fwhm for

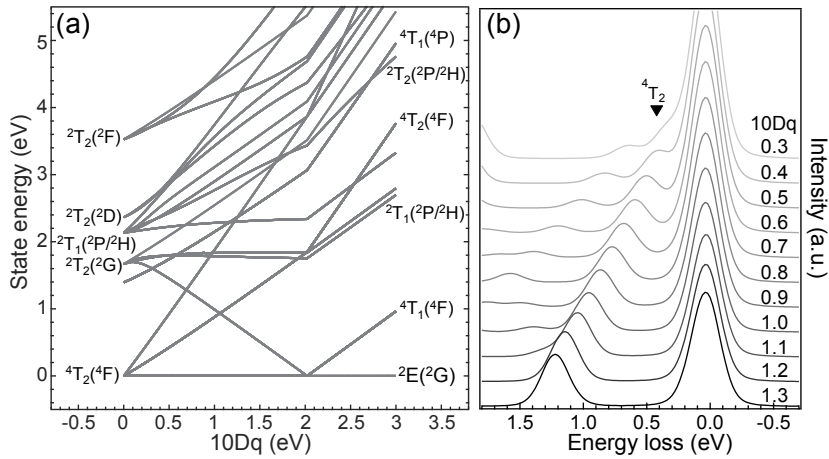


Figure 2.8: (a) The Tanabe-Sugano diagram of the d^7 configuration without considering spin-orbit coupling and LMCT effect. Note that the Slater integrals values F_{dd}^2 , F_{dd}^4 , F_{pd}^2 , G_{pd}^1 , and G_{pd}^3 are 82%, 94%, 88%, 80%, and 88% of the Hartree-Fock values, respectively. (b) The $2p3d$ RIXS simulated spectra at a constant excitation energy with $10Dq_{ion}$ floating from 0.3 to 1.3 eV without charge transfer effect. Note here that because of the spin-orbit coupling has been included in (b), so the 4T_2 peak positions are a bit higher than the lowest 4T_2 state in (a).

lifetime of dd excitations. To simulate the experimental broadening, a Gaussian broadening of 160 meV fwhm was applied on both incoming and outgoing beams. This experimental broadening implies an overall broadening of the elastic peak about ~ 250 meV. The elastic 4T_1 peak is split into 12 individual states spread over 100 meV^[4], which is beyond the resolving ability.

2.3.4 The Determination of the Crystal Field Value $10Dq$ from $2p3d$ RIXS Experiments

In our LMCT simulation, $10Dq$ and Δ are the only two free parameters that are used in addition to the fixed atomic parameters. From the Tanabe-Sugano diagram^[74] it is known that the effective value of $10Dq$ is close to the splitting between the ground state and the first dd excitations. In other words, the first peak in the dd excitations will be close to the value of $10Dq$. We will investigate the relation between the first dd excitation energy and $10Dq$. In the Co^{2+} ($3d^7$) Tanabe-Sugano diagram (Fig. 2.8a), the energy difference between the 4T_1 and 4T_2 states is linear in $10Dq$ between 0.2 and 1.3 eV. This energy difference corresponds to the first dd excitation in the $2p3d$ RIXS spectra. As such, one can track

the $10Dq$ value by locating the first dd excitation peak (Fig. 2.8b), which is more reliable than fitting the $2p$ XAS spectrum^[63]. The energy difference between the 4T_1 and 4T_2 states has been collected in Table 2.4 and Fig. 2.9. Note that in a model without charge transfer, $10Dq_{ion}$ is the same as $10Dq_{eff}$. In other words, the first dd excitation (4T_1 to 4T_2 excitation) can be directly related to $10Dq_{eff}$. However, more generally, the multi-electron configuration should be concerned. From these data points, the following relation regarding the crystal field splitting was derived:

$$10Dq_{eff} \equiv \Delta E_{{}^4T_1-{}^4T_2} \simeq 0.865 \times 10Dq + 0.0534. \quad (2.11)$$

This equation shows that the difference between 4T_1 and 4T_2 states is not exactly equal to $10Dq$ but they are correlated with a linear relationship. The standard errors of linear fit are about ± 0.006 and ± 0.005 for coefficients 0.865 and

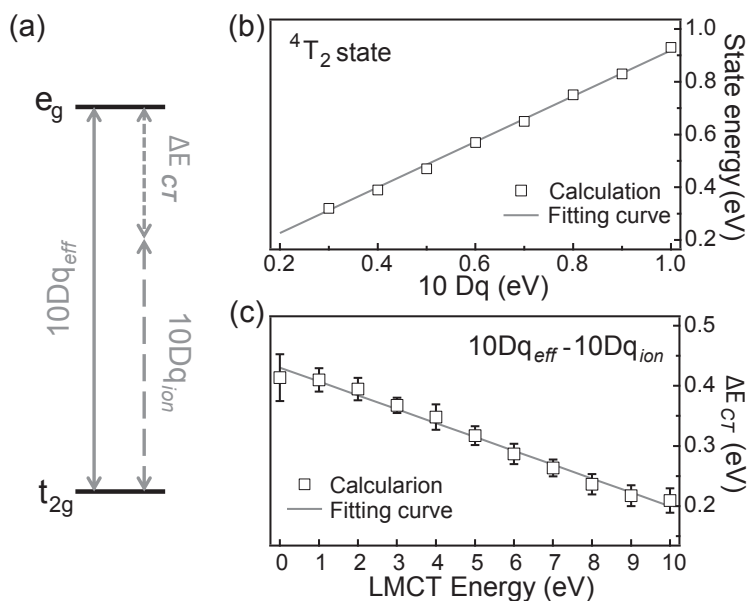


Figure 2.9: (a) The conceptual contributions of $10Dq_{eff}$ (Eq. 2.9). (b) The energy difference between the ground state (4T_1) and the first dd excitation (4T_2) as a function of $10Dq$ without LMCT effect. (c) ΔE_{CT} correlation with respect to LMCT energy Δ . The fitted straight lines in (b) and (c) provide the values given in Eq. 2.11 and 2.12, respectively. The error bars in panel (c) is the root mean square error of the difference from average of the sets $10Dq_{ion} = 0.5, 0.75,$ and 1.0 eV.

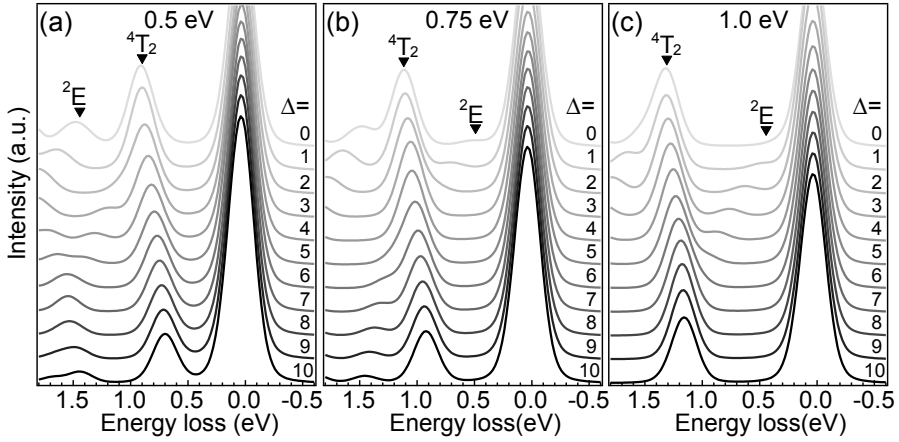


Figure 2.10: $2p3d$ RIXS spectra at a constant excitation energy with floating Δ and $10Dq_{\text{ion}}$ fixed at (a) 0.5 eV, (b) 0.75 eV, and (c) 1.0 eV.

Table 2.5: Energy maximum of the first dd peak in the RIXS calculations with different $10Dq_{\text{ion}}$ and Δ . $10Dq_{\text{eff}}$ and ΔE_{CT} were obtained from Eq. 2.11 and 2.12, respectively.

Δ	$10Dq_{\text{ion}} = 0.5$			0.75	1.0
	4T_1	$10Dq_{\text{eff}}$	ΔE_{CT}	ΔE_{CT}	ΔE_{CT}
0	0.86	0.932	0.432	0.414	0.395
1	0.85	0.921	0.421	0.414	0.395
2	0.83	0.898	0.398	0.391	0.395
3	0.80	0.863	0.363	0.367	0.372
4	0.78	0.844	0.344	0.356	0.349
5	0.75	0.805	0.305	0.321	0.325
6	0.73	0.782	0.282	0.298	0.279
7	0.72	0.770	0.270	0.263	0.256
8	0.69	0.735	0.235	0.240	0.233
9	0.67	0.712	0.212	0.229	0.210
10	0.66	0.701	0.201	0.217	0.210

0.0534 respectively. From this relation we can determine the $10Dq$ value experimentally from the first dd excitation of the $2p3d$ RIXS spectra. The peak maximum of the first dd excitations are 0.85, 0.77, 0.71 and 0.67 eV for CoF_2 , CoCl_2 ,

CoBr₂ and CoS, respectively. In all cases the first peak relates to the ⁴T₂ state (Fig. 2.11a)^[4, 5, 74, 163, 165–167]. The 10Dq_{eff} values of the compounds were converted using Eq. 2.11 and they are 0.92, 0.81, 0.75 and 0.70 eV for CoF₂, CoCl₂, CoBr₂ and CoS, respectively.

2.3.5 The Ionic and Covalent Contribution to the Crystal Field Splitting

When the LMCT effect is considered, the charge transfer contributes to the e_g-t_{2g} splitting, i.e. the overall effective crystal field is caused by both ionic and charge transfer contributions. The total crystal field splitting (10Dq_{eff}) should be reconsidered as the effect from two components (cf. Eq. 2.9):

(1) *The ionic crystal field value (10Dq_{ion})*

(2) *The charge transfer contribution (ΔE_{CT})*

Figure 2.9a shows the ionic and charge transfer contributions of the crystal field splitting. In the simulations we relate the first *dd* peak to the total crystal field splitting, which implies that after the determination of the charge transfer energy Δ, we have to adjust 10Dq_{ion}. Figure 2.9c shows the results for a series of calculations as a function of Δ. One can observe a linear trend between the value of Δ and (10Dq_{eff} - 10Dq_{ion}). This implies a linear relation between the charge transfer contribution (ΔE_{CT}) and Δ (cf. Fig. 2.9c):

$$\Delta E_{CT} = 10Dq_{eff} - 10Dq_{ion} \simeq 0.43 - 0.0239 \times \Delta. \quad (2.12)$$

The standard errors of linear fit are about ±0.006 and ±0.001 for coefficients 0.43 and 0.0239 respectively. The Fig. 2.9c are the average of three cases that the 10Dq_{ion} values are equal to 0.5, 0.75, and 1.0 eV, respectively (Fig. 2.10).

Table 2.6: The experimental 1st-*dd* excitation and its relation to different 10Dq values and Δ.

	1st- <i>dd</i> Exp.	10Dq _{eff} ⇒ Eq. 2.11	10Dq _{ion}	10Dq _{CT} Eq. 2.12 ⇐	Δ
CoF ₂	0.85	0.92	0.70	0.22	8.8
CoCl ₂	0.77	0.81	0.47	0.34	3.6
CoBr ₂	0.71	0.75	0.38	0.37	2.4
CoS	0.67	0.70	0.29	0.41	0.8

We selected the 4T_2 state and used Eq. 2.11 in next subsection to convert the excitation energy back to $10Dq_{eff}$. Then the ΔE_{CT} values could be worked out by subtracting the $10Dq_{ion}$ from $10Dq_{eff}$. All these ΔE_{CT} values are given in Table 2.5.

We optimized the Δ values by comparing the calculated charge transfer peak to the experimental spectra. In Table 2.6 the Δ and ΔE_{CT} values are given and after applying Eq. 2.12 the ionic crystal energy $10Dq_{ion}$ was obtained. We note that the Eq. 2.12 implies that ΔE_{CT} is only dependent on the Δ value. Moreover, the linear model only gives a small error after applying different Δ values.

2.4 Discussion

In Fig. 2.11, we compare the spectra of four compounds at the incident energy A. Figure 2.11a focus on the first 1.5 eV region. An interesting observation is that the width of the elastic peak in CoF_2 (fwhm ~ 280 meV) is larger than that in CoS (fwhm 230 meV), whereas the experiment resolution was 160 meV with an uncertainty of less than 10 meV. In other words, the observed elastic peak broadenings are larger than experiment resolution. It will be discussed in the subsection 2.4.1. Figure 2.11b shows the trend of charge transfer excitations as a function of Δ in both experimental and simulated spectra. The LMCT energies were determined according to these charge transfer excitations. The obtained Δ values were 8.8, 3.6, 2.4, and 0.8 eV with respect to the CoF_2 , CoCl_2 , CoBr_2 , and CoS samples, which are listed in Table 2.6. Figure 2.12 summaries the contributions of $10Dq_{eff}$ (filled bars), $10Dq_{ion}$ (gradient bars), and ΔE_{CT} (slides bars) in a graphical presen-

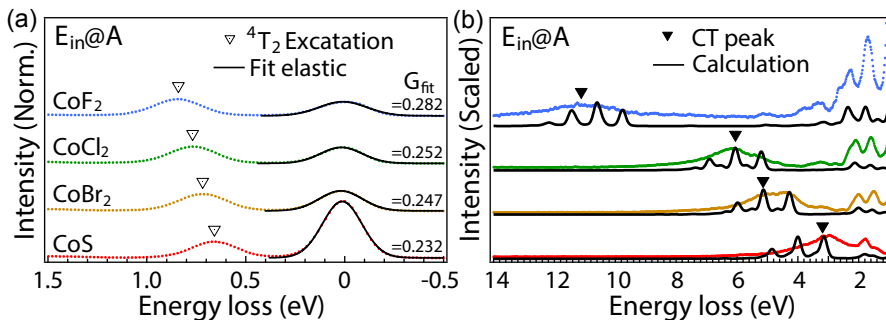


Figure 2.11: Zoom of the $2p3d$ RIXS spectra at incident energy A in (a) the low energy loss region (between -0.5 and 2 eV) and (b) the charge transfer excitation region.

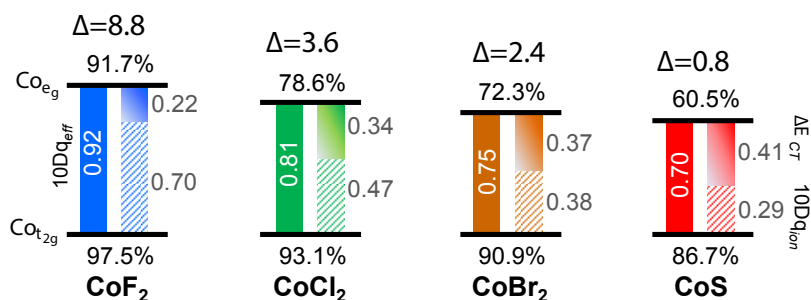


Figure 2.12: A graphical representation for the conceptual effective crystal field energy splitting and the cobalt ionic orbital covalence in a function of Δ .

tation. It also shows the covalency values of e_g and t_{2g} orbitals. These covalency values were defined as the expecting population of electrons in the Cobalt e_g and t_{2g} orbitals. Further detail will be discussed in subsection 2.4.2.

2.4.1 The Width of the Elastic Peak

The observed elastic peak broadenings are larger than experiment resolution implies that there are additional broadening mechanisms due to (1) $3d$ spin-orbit coupling, (2) magnetic exchange, (3) symmetry distortions and/or (4) vibrations. The effects (1), (2) and (3) split the 4T_1 ground state^[4]. Infrared spectroscopy results^[149] show that the highest energy of the spin-orbit coupling peak (interacting with the exchange field) is 0.173 eV for CoF_2 , while the energies for CoCl_2 and CoBr_2 are 0.148 eV and 0.143 eV, respectively, confirming the 0.03 eV broadening difference in Fig. 2.11a.

One possible reason for this effect is that when the Δ value is smaller, the d^n and $d^{n+1}\underline{L}$ configurations are more hybridized, leading to an effective reduction of the $3d$ spin-orbit coupling (Fig. 2.13a). Whereas, the atomic $3d$ spin-orbit coupling is small and if it is fully quenched, the maximum energy shift is approximately 0.05 eV while the energy shift in the experimental 1st- dd excitation is ~ 0.2 eV. An alternative scenario is that, the more ionic the compound, the larger the effect of a crystal field distortion. This implies side peaks surround the elastic peak at higher energies compared to less ionic cases. Fig. 2.13b shows the broadening and intensity change of elastic peak as a function of a crystal field distortion D_s . When the distortion is large enough, the elastic peak envelope reveals a shoulder. A combination of the above effects can explain the observed experimental broadening of the quasi-elastic features in Fig. 2.11a.

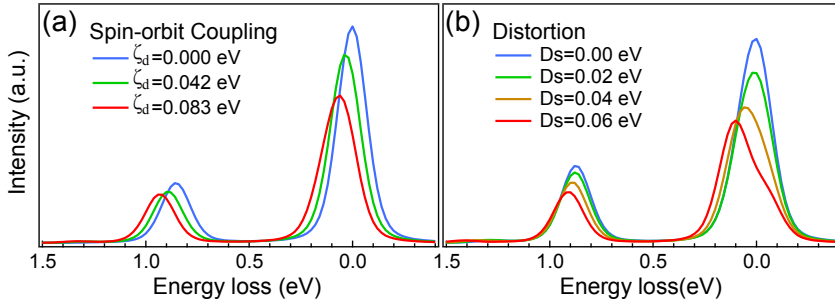


Figure 2.13: Theoretical RIXS spectra with varying (a) $3d$ spin-orbit coupling magnitudes and (b) D_s values. The crystal field value $10Dq = 1$ eV and the magnetic exchange coupling $M = 10$ meV. The Gaussian broadenings are set at 0.1 eV for both the incoming and outgoing beam.

2.4.2 Ground State Analysis and Differential Orbital Covalency

A trend of the charge transfer excitations is visible as a function of Δ (see Fig. 2.11b). The obtained Δ values were 8.8, 3.6, 2.4, and 0.8 eV with respect to the CoF_2 , CoCl_2 , CoBr_2 , and CoS samples. The center of the features were extracted from the spectra and are given in Table 2.2. A smaller Δ value leads to a stronger hybridization of ground state between the $3d^7$ and $3d^8\bar{L}$ configurations, in which the ground state can be described by $|\Psi_{GS}\rangle = \alpha|3d^7\rangle + \beta|3d^8\bar{L}\rangle$ with the population coefficient values α and β . It gives the hybridization percentages of the original multiplet ($|\alpha|^2$) and the ligand hole multiplet configuration ($|\beta|^2$).

To obtain the hybridization percentages, the microstates of the ground state are projected into separate $3d^7$ and $3d^8\bar{L}$ configurations of specific orbitals derived from symmetry (in octahedral symmetry, for example, in terms of e_g and t_{2g} orbitals)^[200]. The results are shown in Table 2.7. It is observed therein that the percentage of the $|3d^7\rangle$ states on the cobalt ion decreases with decreasing Δ . The percentage of ligand-hybridized $|3d^8\bar{L}\rangle$ states for CoS is $\sim 30\%$. From these numbers, the metal covalency of the e_g and t_{2g} orbitals can be estimated. Here we only consider one-electron hopping from the ligand to the metal ion e_g or t_{2g} orbitals. Hence only the $3d^7$ ground state $|t_{2g}^5 e_g^2\rangle$ and the ligand hole e_g $|t_{2g}^5 e_g^3\bar{L}\rangle$ and t_{2g} $|t_{2g}^6 e_g^2\bar{L}\rangle$ states are taken into account. The covalence fraction of cobalt within e_g orbitals is then given by

$$C(e_g) = 100\% - \left(\frac{3}{2}\right) \frac{P_{t_{2g}^5 e_g^3}^5}{P_{t_{2g}^5 e_g^2}^5 + P_{t_{2g}^5 e_g^3\bar{L}}^5 + P_{t_{2g}^6 e_g^2\bar{L}}^6}, \quad (2.13)$$

Table 2.7: Orbital occupation and covalency analysis of CoF₂, CoCl₂, CoBr₂ and CoS. The expectating charge number $\langle n \rangle$ are 7.06, 7.16, 7.21, and 7.30 with respective to these four compounds.

	$ d^7\rangle$		$ d^8\mathbf{L}\rangle$			Metal Covalency		
	$ t_{2g}^5 e^2\rangle$	$ t_{2g}^4 e^3\rangle$	$ t_{2g}^6 e^2\mathbf{L}\rangle$	$ t_{2g}^5 e^3\mathbf{L}\rangle$	$ t_{2g}^4 e^4\mathbf{L}\rangle$	T _{2g}	E _g	DOC
CoF ₂	85.3	8.6	0.8	5.1	0.3	97.5	91.7	5.8
CoCl ₂	75.7	8.3	2.1	12.9	1.0	93.1	78.6	14.4
CoBr ₂	71.0	8.1	2.7	16.7	1.4	90.9	72.3	18.6
CoS	62.5	7.4	4.0	23.8	2.3	86.7	60.5	26.2

where $\frac{3}{2}$ is a renormalization factor (2 out of 3 holes in the d_7 configuration are in e_g orbitals) and $P_{t_{2g}^x e_g^y}$ are the percentages for configuration $t_{2g}^x e_g^y$ as given in Table 2.7. This implies that the covalence fraction of cobalt within the e_g orbitals is reduced from 100%, by the corresponding fraction of ligand character within these e_g orbitals. Similarly, the covalence fraction of cobalt in the t_{2g} orbitals is then given by

$$C(t_{2g}) = 100\% - \left(\frac{3}{1}\right) \frac{P_{t_{2g}^6 e_g^2}}{P_{t_{2g}^5 e_g^2} + P_{t_{2g}^5 e_g^3\mathbf{L}} + P_{t_{2g}^6 e_g^2\mathbf{L}}}. \quad (2.14)$$

It follows that, when going through the series from CoF₂ to CoS, the cobalt ion character in the e_g orbitals decreases faster than that in the t_{2g} orbitals (Fig. 2.12). In octahedral symmetry, the ligand $2p$ orbitals overlap strongly with the cobalt $3d$ e_g ($d_{x^2-y^2}$ and d_{z^2}) orbitals, thus ligand hybridization is affecting e_g orbitals more than t_{2g} orbitals. By subtracting the e_g from the t_{2g} orbital covalency one obtains the differential orbital covalency (DOC)^[206] as given in Table 2.7. The DOC values are dependent on crystal field symmetry and strength, as well as charge transfer hopping energies. Note that we obtain a similar DOC value for CoS as obtained for $[\text{FeCl}_6]^{3-}$ with similar symmetry and charge transfer settings^[206]: CoS ($\Delta = 0.8$ eV; $T_{e_g} : T_{t_{2g}} = 2:1$) and $[\text{FeCl}_6]^{3-}$ ($\Delta = 0.1$ eV; $T_{e_g} : T_{t_{2g}} \simeq 2:1$) have DOC values of 25-27%.

2.4.3 Charge Transfer Parameters Derived from $2p3d$ RIXS Compared with $2p$ XPS

By comparing the Δ values in Table 2.6 with XPS-derived Δ values^[154] only the value for CoF₂ is found to be equal (RIXS: 8.8 eV vs. XPS: 8.6 eV). CoCl₂ (RIXS: 3.6 eV vs. XPS: 4.5 eV) and CoBr₂ (RIXS: 2.4 eV vs. XPS: 3.5 eV) show less agreement. For CoS a small Δ value (0.8 eV) was found, which is related

to the sample exhibiting metallic behavior^[144, 187]. First, a simulation including the third configuration $3d^9\bar{L}^2$ has been tested. In the case of CoBr_2 (Fig. 2.14), the bonding state shows no remarkable difference between two and three configurations simulations and the $3d^9\bar{L}^2$ configuration contribution can be ignored if only the bonding state is considered. On the other hand, the simulation with three configurations gives a smaller anti-bonding state energy, compared to the two configuration solution at fixed Δ . The three configuration calculation shifts the charge transfer excitation ~ 0.3 eV lower than the two configuration calculation with the same Δ value. In other words, the Δ value should be ~ 2.7 eV ($2.4 + 0.3$) for CoBr_2 when we consider the third configuration. This brings the Δ value a bit closer but smaller to the XPS value (3.5 eV). Note that we used zero width for the configuration with ligand hole. In this simplified case, it reduces the calculating loading but still represent the shift of the anti-bonding states.

Figure 2.15 displays the final state configurations of the XAS, XPS, and RIXS processes. It shows the energy differences between the ionic configuration and the two charge transfer configurations. The notations EG and EF refer to a ground and final states, respectively. The numbers 1 to 3 refer to configurations with zero, one, and two ligand hole(s), respectively. The charge transfer configurations show that the core-hole potential (Q) needs to be taken into account in the case of XAS and XPS spectra. This implies that we have to optimize Q (in addition to Δ) to simulate the XAS/XPS spectra. Due to the larger screening effects, at least three charge transfer configurations need to be taken into account for XPS spectra^[150, 207]. On the other hand, the relative final state energy of the first LMCT configuration in

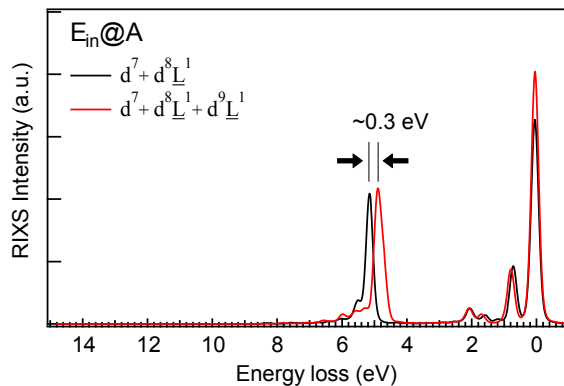


Figure 2.14: $2p3d$ RIXS simulations with two (black) and three (red) configurations using the reported CoBr_2 parameters.

valence RIXS is Δ . Being independent of Q , the core-hole will not contribute to the relative configuration energy in $2p3d$ RIXS, where we note that via its influence on $2p$ XAS Q could influence the intensities. We ignore the second LMCT configuration in the RIXS calculations. As indicated in Fig. 2.15, the relative initial and final state energies of the second LMCT configuration is $2\Delta+U$ in RIXS. In the vast majority of cases, its relative energy will be significantly higher than that of the first LMCT configuration and will play a negligible role in the spectral shape. Finally, we note that our Δ and $10Dq_{ion}$ determinations are in line with LMCT analysis of CoO $2p3d$ RIXS by Magnuson *et. al.*^[5].

We conclude that RIXS is more accurate for the determination of Δ due to (1) the sharper experimental features and (2) the smaller (non-local) screening effects. Note that the uncertainty in the atomic parameters (and in $10Dq$) is also present in XPS, but due to the absence of spectral features it is not possible to gain experimental information regarding their exact values. Because $2p$ XAS and $2p3d$ RIXS are not sensitive to the separate values of U and Q , a full electronic structure determination would ideally consist of $2p3d$ RIXS combined with $2p$ XPS, or another (resonant) photoemission/Auger experiment.

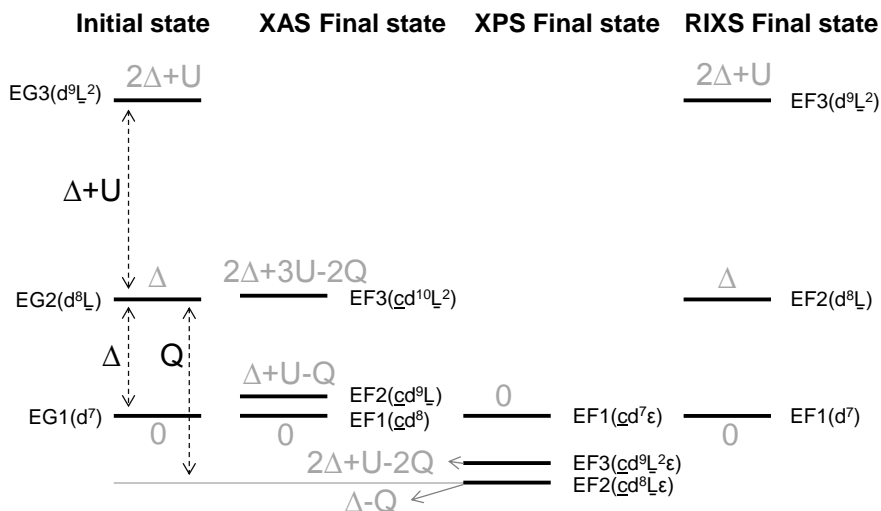


Figure 2.15: The initial ground and final state energy configurations of XAS, XPS, and RIXS.

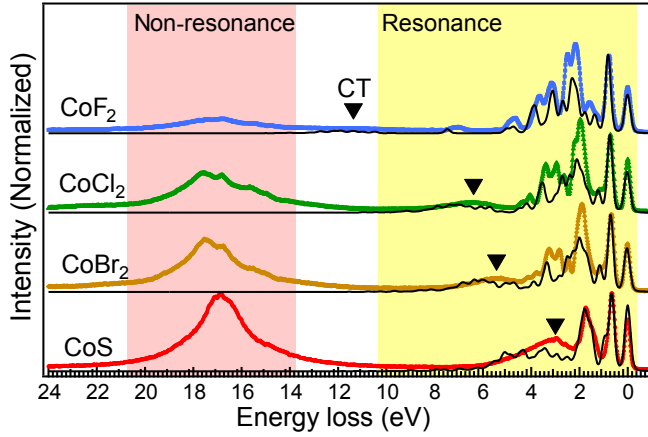
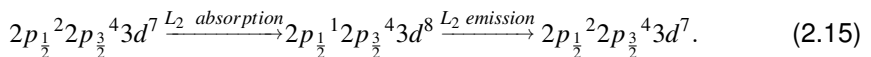


Figure 2.16: Experimental (color marks) and simulated (black lines) RIXS spectra at incident energy G.

2.4.4 The Use of the Coster-Kronig Auger Channel

In this subsection, the L_2 -edge ($2p_{1/2}3d$) RIXS spectra are discussed. In comparison with the L_3 -edge ($2p_{3/2}3d$) RIXS spectra, the L_2 -edge RIXS spectra give the resonant spectra of $3d2p_{1/2}(L_2)$ emission and in addition the non-resonant spectra of $3d2p_{3/2}(L_3)$ emission. Figure 2.16 shows the experimental and calculated results. Between 0 and 10 eV the spectra show the dd excitations and the charge transfer excitations, reproduced with the same procedure as discussed above. New features were observed in the high energy loss region. These features relate to X-ray emission from the $3d2p_{3/2}$ channel. The integrated intensity ratio between non-resonant (9eV – 25eV) and resonant (-2 eV – 8.5 eV) emissions (L_3/L_2) are ~ 0.55 , 1.06, 1.22, and 1.71 for CoF_2 , CoCl_2 , CoBr_2 , and CoS , respectively.

In order to explain these features, the core hole decay was simplified in two groups: radiative decay (X-ray emission) and non-radiative or electronic decay (Auger). In case of $2p$ core holes in $3d$ transition metal ions, the electronic decay channels constitute more than 99% of the total decay and they dominate the life time^[9, 182, 204]. These Auger channels are dominated by the $2p3p3p$, $2p3p3d$ and $2p3d3d$ decays. In the resonant $2p_{1/2}3d$ X-ray emission, the RIXS signal follows the process:



The scattering cross-section is proportional to the radiative decay. In case of the non-resonant channel, a Coster-Kronig Auger channel is involved in the first step of the decay process^[182]:



The $3d2p_{3/2}$ X-ray emission intensity is proportional to the strength of the Coster-Kronig Auger channel, where the other Auger channels are equivalent in strength for the L_3 - and the L_2 - edges^[181, 193, 203]. The large L_3 X-ray emission for CoS implies that the Coster-Kronig channel is strong, which is correlated with the large charge transfer effects. This behavior has also been studied on cobalt clusters in SiO_2 ^[193] and iron based superconductors^[208–210]. Our conclusion is that the intensity of the Coster-Kronig induced non-resonant X-ray emission is a measure of the covalency of a system, where further study is required to quantify this effect for different elements.

2.4.5 Comparing the Calculation with and without LMCT Effect

Here, we also compare the simulated results with and without LMCT effect. The calculations with LMCT effect has been obtained above. In the LMCT simulations, the Slater integrals values F_{dd}^2 , F_{dd}^4 , F_{pd}^2 , G_{pd}^1 , and G_{pd}^3 are 82%, 94%, 88%, 80%, and 88% of the Hartree-Fock values, respectively. The calculation without LMCT effect were generated by reducing the Slater integrals, which is known as the nephelauxetic effect. The initial setting of atomic initial Slater integral values were given as: $F_{dd}^2 = 9.284$ eV and $F_{dd}^4 = 6.678$ eV for $2p^6 3d^7$ configuration and $F_{dd}^2 = 9.917$, $F_{dd}^4 = 7.140$, $F_{pd}^2 = 5.808$, $G_{pd}^1 = 3.886$, and $G_{pd}^3 = 2.455$ eV for $2p^5 3d^8$ configuration. These values have been reduced by 80% from the Hartree-Fock approximation. The F_{dd} reduction percentages were used as 95%, 85.5%, 83.1%, and 71.3% for CoF_2 , CoCl_2 , CoBr_2 , and CoS , respectively.

The main features of $2p$ XAS were reproduced well in both simulations, see Fig. 2.17. We remark that the peak F in the XAS result should not be the main characteristic feature from the LMCT contribution, because it can also be simulated without applying LMCT effect. The LMCT satellite peaks (indicated as CT in the figures), which are not found in the pure ionic simulations. However, these peaks were not clearly visible due to the considerable ligands p band broadening of $2p^5 3d^8 \underline{L}$ configuration, where 2.2 eV was used in the calculations.

Figure 2.18 shows that the RIXS spectra can emphasize the LMCT features even we probe the system at pre-edge (energy A). The calculations without charge

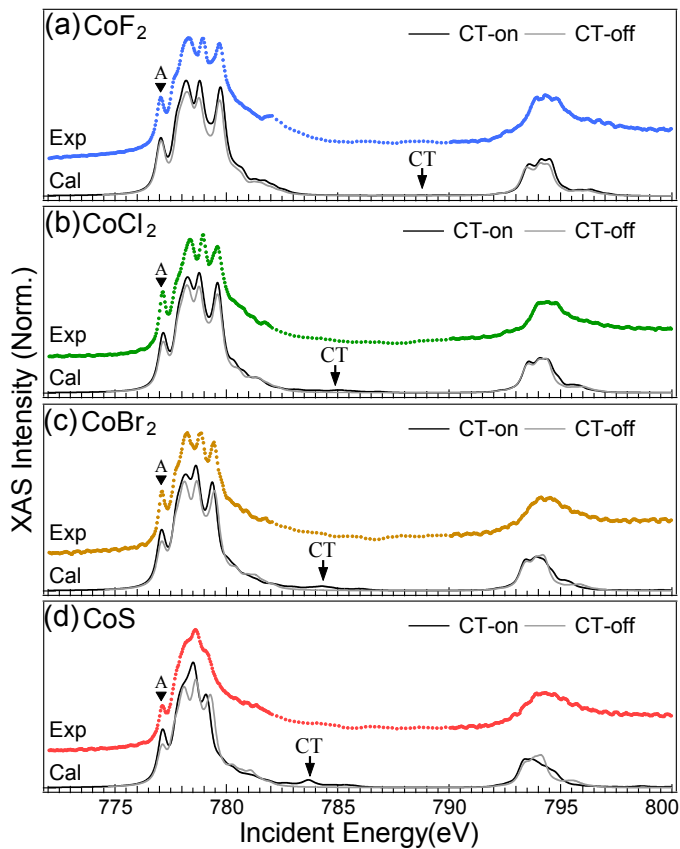


Figure 2.17: Comparisons of calculated $2p3d$ XAS spectra with experimental spectra of (a) CoF_2 , (b) CoCl_2 , (c) CoBr_2 , and (d) CoS . The black and gray lines are the simulation with and without the charge transfer effect, respectively.

transfer effect give no anti-bonding features although the bonding features can be reproduced well. This implies that RIXS might be able to investigate the bond's properties in a complex structure. With a proper selected incident energy, the LMCT features can be enhanced (cf. Fig. 2.5).

2.5 Conclusions

We have measured high resolution $2p3d$ RIXS results of CoF_2 , CoCl_2 , CoBr_2 and CoS . Charge transfer multiplet calculations are able to accurately reproduce the spectral shapes. The analysis revealed accurate values of the charge transfer energy Δ and the crystal field value $10Dq$, where the crystal field is split into

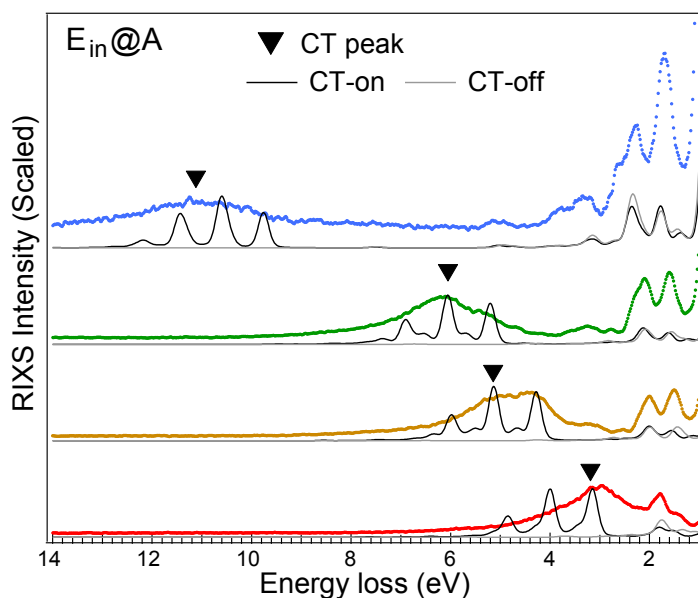


Figure 2.18: Comparisons of calculated $2p3d$ XAS spectra with and without charge transfer effect to the experimental spectra.

ionic and charge transfer contributions. In comparison with XPS, $2p3d$ RIXS is a more accurate method to determine the charge transfer energy (Δ). In addition, it is more precise regarding the crystal field value $10Dq$ and also to determine the atomic electron-electron interactions (Slater integrals). From the simulations, the orbital occupancies of the different states are given and the corresponding differential orbital covalency analysis confirms that CoS is significantly more covalent than CoF_2 . It is observed experimentally, that the broadening of the quasi-elastic peak become gradually smaller while going from ionic CoF_2 to covalent CoS, either due to an effective reduced $3d$ spin-orbit coupling and/or symmetry distortions.

The L_2 -edge RIXS spectra are analyzed with respect to the integrated intensity ratio between resonant ($2p_{1/2}3d$) and non-resonant ($2p_{3/2}3d$) X-ray emissions, which are ~ 0.55 , ~ 1.06 , ~ 1.22 , and ~ 1.71 for CoF_2 , CoCl_2 , CoBr_2 , and CoS, respectively. These numbers show that the Coster-Kronig channel is stronger in CoS and we conclude that the ratio between resonant and non-resonant decay is a potential tool to probe the effects of electron delocalization.

Chapter 3

Spin State Competition of Co^{3+} Ions in LaCoO_3 Crystals and Films

Distinguishing the ground state electronic structure of Co^{3+} in LaCoO_3 is a challenge because the ground state is close to the spin state transition point. In this Chapter, I present 90 meV resolved Co $2p3d$ resonant inelastic X-ray scattering linear dichroism spectra of strained LaCoO_3 films and a LaCoO_3 single crystal. A polarization dependent low energy excitation is observed at ~ 0.2 eV on the tensile-strained $\text{LaCoO}_3/\text{SrTiO}_3$ film, while it is not observed in neither bulk LaCoO_3 nor the compressive-strained $\text{LaCoO}_3/\text{LaAlO}_3$ film. Guided by cluster calculations, it is possible to distinguish the spin state manifolds close to transition point of Co^{3+} ions in LaCoO_3 systems. Through a polarization analysis, I show that the spin state can easily flip from a low-spin $^1A_{1g}$ state in an octahedral symmetry to the high-spin $^5B_{2g}$ or 5E_g states with a small tetragonal distortion. The mixture of spin states suggests that the high-spin Co^{3+} plays an important role in long-range ferromagnetic order on both tensile- and compressive- strained LaCoO_3 films.

This chapter is based on the publication:

R.-P. Wang, J. Geessinck, H. Elnaggar *et al.*, “Low Energy Orbital Excitations in Strained LaCoO_3 films”, **submitted to Phys. Rev. B**

3.1 Introduction

The interaction between the charge, orbital and spin degrees of freedom is important in strongly correlated systems and as such they determine the physical properties of the $3d$ transition metal oxides. An example of a metal oxide with complex magnetic behavior is the perovskite LaCoO_3 . A diamagnetic to paramagnetic transition at ~ 100 K has been observed in bulk LaCoO_3 and discussed as a spin crossover from a low-spin state (LS, $S=0$) to a high-spin state (HS, $S=2$) or alternatively to an intermediate-spin state (IS, $S=1$)^[79, 82, 90, 95, 97, 211]. Long-range ferromagnetic order has been observed in epitaxially strained LaCoO_3 thin films^[114–118], which implies that these LaCoO_3 thin films are ferromagnetic insulators for potential application in spintronic devices and therefore of technological relevance^[119, 120].

The ferromagnetic order in LaCoO_3 films is still under debate. Initially, it was described as being caused by the exchange interaction between LS and HS Co^{3+} ions^[114–117]. Within this exchange, two mechanisms were proposed: (i) The tetragonal distortion bends the Co-O-Co bond angle from $\sim 163^\circ$ to 180° and increases the superexchange interaction ($2J_{ex}$)^[114, 115]; (ii) The tetragonal distortion breaks the ground state symmetry and causes a competition between LS and HS Co^{3+} ions^[121–124], as illustrated in Fig. 3.1a-d. Fumega and Pardo proposed that the ferromagnetic state is more stable in structures with an oxygen vacancy order, which implies that Co^{2+} ions can be involved in a double exchange type interaction between Co^{3+} and Co^{2+} ^[130, 131]. The existence of Co^{2+} ions is consistent with the experimental evidence that the magnetic moment of the LaCoO_3 film increases with thickness^[124, 126, 127, 212]. Both oxygen vacancies (i.e. Co^{2+}) and HS Co^{3+} have been used to explain the structural defects observed (dark lines) using scanning transmission electron microscopy (TEM)^[127–129]. But large Co^{2+} concentrations have not been found in X-ray absorption spectroscopy (XAS) or TEM with electron energy loss spectroscopy (EELS) measurements. Moreover, it has been found that a large amount of oxygen vacancies ($>10\%$) strongly reduce the magnetism^[120].

In order to contribute to the debate about the origin of magnetism in LaCoO_3 , we employ $2p3d$ Resonant Inelastic X-ray Scattering ($2p3d$ RIXS) to study the complex electronic configuration of the Co ions in a LaCoO_3 single crystal and strained thin films. $2p3d$ RIXS probes both the local^[2–5, 8–11, 213] and collective excitations^[12–18, 214], including small lattice distortions^[6, 7, 125]. In the case of LaCoO_3 , the $2p3d$ RIXS process in the ionic limit can be described as $3d^6 > 2p^5 3d^7 > 3d^6$ transitions of Co^{3+} ions, which allows us to distinguish the spin

state manifolds. An bulk LaCoO_3 system (with Co in octahedral oxygen network) has a LS ${}^1A_{1g}(\text{O}_h)$ ground state at low temperature, whereas small tetragonal distortions cause a ground state change when the crystal field energy ($10Dq$) is close to the crossover point ($10Dq_{\text{cross}}$) as demonstrated in Fig. 3.1b. In con-

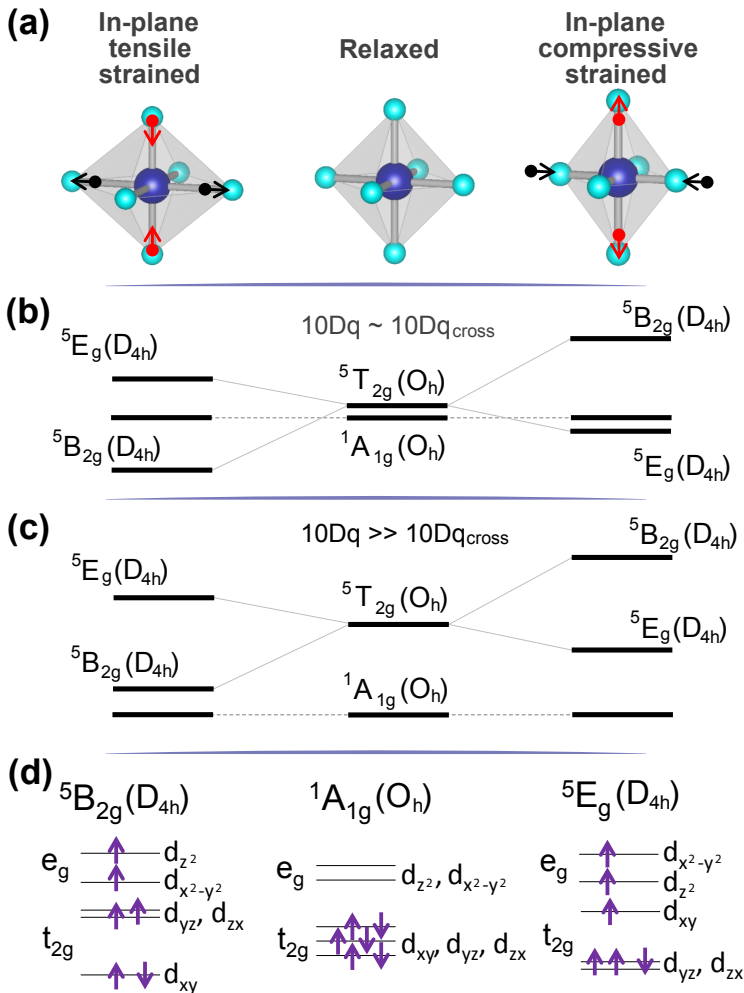


Figure 3.1: (a) Octahedral oxygen network surrounding Co in relaxed and with in-plane compressive/tensile tetragonal distortions. (b)-(c) The energy levels splitting of the ${}^5T_{2g}(\text{O}_h)$ state on Co^{3+} due to the tetragonal distortions when (b) $10Dq \sim 10Dq_{\text{cross}}$ and (c) $10Dq \gg 10Dq_{\text{cross}}$. (d) Electronic configurations for the three ground states ${}^1A_{1g}(\text{O}_h)$, ${}^5B_{2g}(\text{D}_{4h})$, and ${}^5E_g(\text{D}_{4h})$.

trast, if $10Dq$ is much larger than $10Dq_{\text{cross}}$, no symmetry change is observed (Fig. 3.1c). The three possible electronic configurations in tetragonal (D_{4h}) symmetry are respectively $^1A_{1g}$, $^5B_{2g}$ and 5E_g (Fig. 3.1d). We note that the term symbols are correlated to the distortions, thus we marked the 5E_g states as $^5E_g(O_h)$ and $^5E_g(D_{4h})$ to distinguish different symmetries. Experimentally, the single crystal LaCoO_3 measurement indicates that the spin state population is varying as a function of temperature, which suggests that the ground state is close to a degeneracy of LS $^1A_{1g}(O_h)$ and HS $^5T_{2g}(O_h)$ states^[103, 214]. Furthermore, different composition mixtures of LS and HS states have been found in the cuboidal (D_{2h}) and trigonal (D_{3d}) distorted LaCoO_3 films through $2p3d$ RIXS^[125], which agrees with x-ray diffraction^[117].

In this chapter, incident photon polarization analysis is presented to gain better insight into the electronic configurations. The polarization dependence was not discussed in the published RIXS papers on the LaCoO_3 films^[125] and the LaCoO_3 crystal^[103]. Guided by simulations, we can identify the observed RIXS features with a polarization dependent analysis. We show that the dichroism intensities are related to the ground state symmetries and change as a function of the distortion parameters from a tensile- to a compressive- strained LaCoO_3 .

3.2 Method

3.2.1 Experiment

Sample preparations and characterizations

The distortion effect of LaCoO_3 was studied on three different samples: an unstrained LaCoO_3 single crystal, a tensile-strained LaCoO_3 film on (001)- SrTiO_3 , and a compressive-strained LaCoO_3 film on (001)- LaAlO_3 . The LaCoO_3 single crystal was grown in O_2 gas flow by the floating-zone method at the department of physics in Tohoku University. It was prepared from a polycrystalline sample obtained by a stoichiometric mixture of high purity powders of La_2O_3 and Co_3O_4 as described in the supplementary material of reference [103]. The LaCoO_3 thin films were fabricated at the MESA+ institute of the University of Twente using pulsed laser deposition combined with situ reflection high-energy electron diffraction (RHEED) to monitor the growth process. The films were grown under a 0.2 mbar O_2 background pressure and at a deposition temperature of 750 C and a laser fluence of 1.9 J/cm^2 . Two 55 nm LaCoO_3 films were prepared on the (001)- SrTiO_3 and (001)- LaAlO_3 substrates, respectively, where the thickness was measured by X-ray reflectivity.

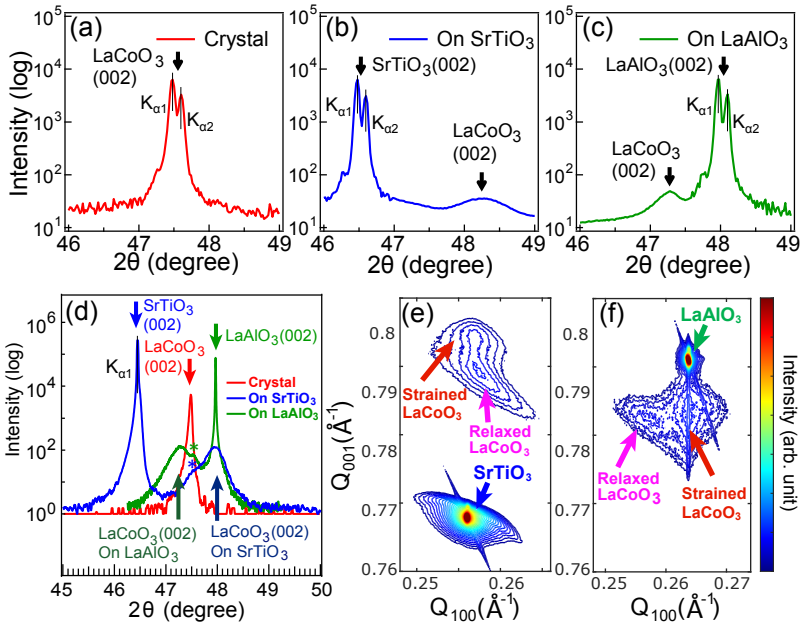


Figure 3.2: (a)-(c) The X-ray diffraction patterns (θ - 2θ scans) of (002) feature for the LaCoO_3 single crystal (a) and 55 nm LaCoO_3 film on the substrates SrTiO_3 (b) and LaAlO_3 (c). The beam source includes copper $K_{\alpha 1}$ and $K_{\alpha 2}$ emission. (d) The monochromatic beam source at the copper $K_{\alpha 1}$ emission. (e)-(f) The 2D reciprocal space map of the (103) feature for (e) the $\text{LaCoO}_3/\text{SrTiO}_3$ film and (f) the $\text{LaCoO}_3/\text{LaAlO}_3$ film. The reciprocal space was scanned along the momentum Q_{100} (horizontal axis) and Q_{001} (vertical axis).

The lattice constants were determined by X-ray diffraction measured along the surface normal orientation (out-of-plane), as indicated in Fig. 3.2a-d. Figure 3.2a-c present the measurements which were performed by a 4-circle diffractometer at Department of Physics in Tamkang University. The small splitting of the peaks correspond to copper $K_{\alpha 1}$ and $K_{\alpha 2}$ emission. Their wavelengths are ~ 1.5406 and ~ 1.5444 Å, respectively. We indicate the diffraction in cubic symmetry, where the pseudocubic lattice constant of the crystal $\mathbf{a}_{\text{cub}} \sim 3.83$ Å was obtained by the projection from $R\bar{3}C$ (012) to cubic (001), see Fig. 3.2a. The lattice constant shows good agreement with the value reported^[114, 115, 215]. For the films, the out-of-plane lattice constants (\mathbf{c}_{LCO}) are ~ 3.78 Å and ~ 3.84 Å for the films on SrTiO_3 and LaAlO_3 substrates, see Fig. 3.2b,c. The in-plane lattice constants of the LaCoO_3 films (\mathbf{a}_{LCO}) are assumed to be similar to the lattice constants of the substrates, which are 3.91 Å and 3.79 Å for the films on SrTiO_3 and LaAlO_3

Table 3.1: The lattice constants as obtained from X-ray diffraction (length in Å). V refers to the calculated volume of the pseudo-cubic unit cell.

	2θ ($K_{\alpha 1}/K_{\alpha 2}$)		Lattice constants			
	Substrate	LaCoO ₃	Substrate	LaCoO ₃	V	ϵ
				a	c	
Crystal	-	47.47/47.60	-	~3.83	~56.2	0%
On SrTiO ₃	46.48/46.60	~48.3*	~3.91	~3.78	~57.8	~2.0%
On LaAlO ₃	47.97/48.90	~47.3*	~3.79	~3.84	~55.2	~-1.0%

substrates, respectively. The lattice constants of the LaCoO₃ film on LaAlO₃ are very close to the single crystal, where smaller strain is found. This induces an in-plane tensile strain on SrTiO₃ substrate ($\mathbf{a}_{\text{LCO}} = \mathbf{a}_{\text{STO}} > \mathbf{a}_{\text{cub}}$) and in-plane compressive strain on LaAlO₃ substrate ($\mathbf{a}_{\text{LCO}} = \mathbf{a}_{\text{LAO}} < \mathbf{a}_{\text{cub}}$). We find that the in-plane tensile strain ($\epsilon \sim 2\%$ on SrTiO₃) compresses the out-of-plane lattice constant and the compressive strain ($\epsilon \sim -1\%$ on LaAlO₃) does the opposite, where ϵ is defined as $\epsilon = (\mathbf{a} - \mathbf{a}_{\text{cub}})/\mathbf{a}_{\text{cub}}$. They are both in the elastic deformation limit ($-1\% < \epsilon < 2\%$)^[115, 124, 216–218] and their volume difference is less than 3% with respect to the single crystal, in other words the conserved volume is consistent with a fully strained film. We thus conclude that the compressive- and tensile-strained films were well characterized for the RIXS measurements. Table 3.1 lists the lattice constants extracted from the diffraction results. Figure 3.2d presents the monochromic X-ray diffraction results and confirms the previous results. The measurements were performed at the MESA+ institute of the University of Twente. Furthermore, the monochromic X-ray diffraction results show additional features as indicated by stars (Fig. 3.2d) in both the films. In order to gain insight into the new features, we measured the two-dimension (2D) reciprocal space map of the LaCoO₃/LaAlO₃ film because its split at $\sim 47.5^\circ$ is more clear. Figure 3.2e and 3.2f shows clearly the features of the strained LaCoO₃ and unstrained LaCoO₃ features in the 2D reciprocal space map. It indicates that the additional features seem to be the contributions from the unstrained LaCoO₃ and point out that there is a compositions mixture of unstrained and strained LaCoO₃ in the films^[124]. For the strained LaCoO₃, the match of in-plane momentum magnitude (along Q_{100}) shows that the in-plane lattice constants (\mathbf{a}_{LCO}) are similar to the lattice constants of the substrates, which supports our assumption.

The paramagnetic to diamagnetic transition of the LaCoO₃ single crystal occurs at ~ 100 K, which has been reported in reference [103]. The saturated mag-

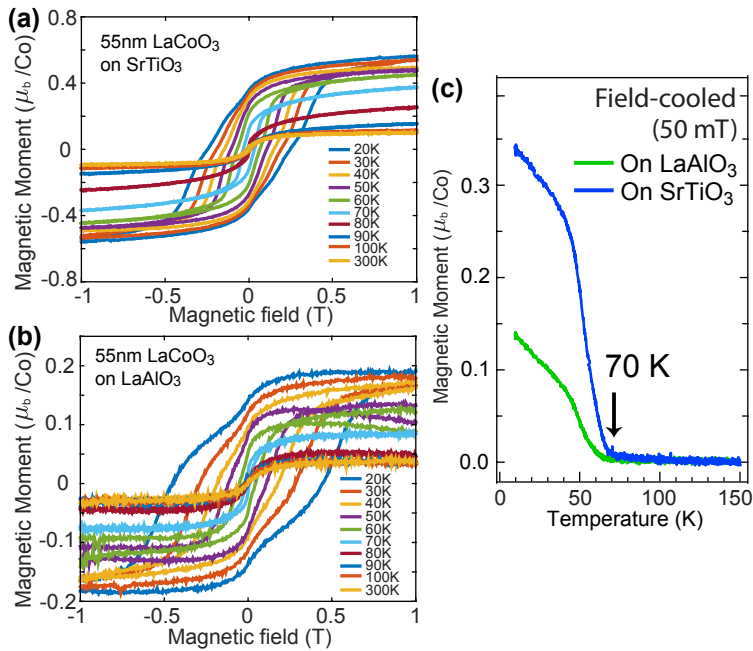


Figure 3.3: The magnetic hysteresis loop of the 55 nm LaCoO₃ films on the substrates (a) SrTiO₃, and (b) LaAlO₃. Above the transition (~ 70 K), the signals were affected by the substrates. (c) The field-cooled measurement in 50 mT as a function of temperature. The magnetic moments above 150 K is not shown here.

netic moment of the 55 nm LaCoO₃ films on SrTiO₃ and LaAlO₃ were measured in-plane via vibrating sample magnetometry (VSM). Figure 3.3a,b show the magnetization data after subtracting a linear background, obtained by performing a linear fit to the data at fields above saturation. The moment was normalized to the thickness of LaCoO₃. The observed two-component hysteresis behavior could be contributed by the combination of ferromagnetic LaCoO₃ films and intrinsic magnetic property of the substrate, where the magnetism of the SrTiO₃ and LaAlO₃ crystals can be either paramagnetic (weak ferromagnetic) or diamagnetic [219, 220]. Below the Curie temperature, the hysteresis loop of the films is the summation of a ferromagnetic-like hysteresis loop and a paramagnetic-like hysteresis loop. Above the Curie temperature, the magnetic behaviors at high temperature are dominated mainly by the substrates, where paramagnetic- and diamagnetic-like hysteresis loop were shown. The onset transition temperature (~ 70 K) can be determined by measuring the magnetic moment while cooling down the sample from 305 K to 10 K under an applied field of 50 mT (Fig. 3.3c).

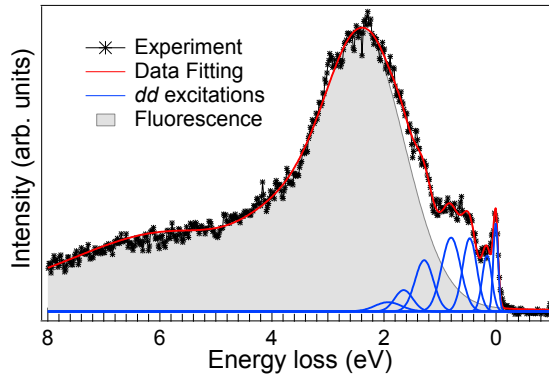


Figure 3.4: The fitting treatment of the RIXS spectra for the $\text{LaCoO}_3/\text{SrTiO}_3$ film. The gray feature is a combination of four Gaussian functions to simulate the fluorescence profile. The blue peaks are the elastic feature and the dd excitations, where the broadening changes from 0.1 to 0.4 eV (fwhm) with increasing energy loss.

RIXS experiments

The XAS and RIXS results were carried out at the 05A RIXS beam line in Taiwan Light Source, where the AGS-AGM system provides a 90 meV (in full width half maximum, fwhm) experimental RIXS resolution at the cobalt L_3 edge^[24]. The incident photon energy broadening is determined by the gap of the slit after the monochromator. In the RIXS measurements, the value of slit gap was 100 μm which provides an incident energy broadening 1 eV (fwhm). Thanks to the energy compensation principle, the wide incident energy broadening will not change the experimental RIXS resolution^[23]. Partial fluorescence yield XAS was also collected using a Silicon photo-diode to calibrate the incident photon energy. During XAS measurements, the incident photon energy resolution was ~ 0.6 eV fwhm (slit gap ~ 50 μm), which is smaller than the line width of the L_3 edge of LaCoO_3 ^[97]. All incident energies were identified with respect to the maximum of the L_3 edge. The precision of the energy calibration is not changed upon increasing the gap of the slit to obtain more flux in the RIXS experiment.

The intensity of the RIXS spectra is influenced by the ion concentration, the exposed area of the sample and the probing path, which implies that different samples cannot be directly compared to each other. In order to compare the spectra acquired from different samples in a consistent approach, we normalized the experimental spectra according to both the exposure time and the area of the fluorescence profile. Figure 3.4 presents a fitting treatment of the RIXS spectra for the

LaCoO₃/SrTiO₃ film as an example. The elastic peak and few distinct excitations were fitted by Gaussian functions with energy losses 0, ~0.2, ~0.4, ~0.8, ~1.3, ~1.5 and ~2.0 eV. The fluorescence profile was modelled by combination of four Gaussian functions (gray area) and used for the normalization. For the simulated spectra, we normalized to the intensities of the charge transfer features, which effectively represent the fluorescence.

3.3 Simulation Model

Cluster calculations were performed including charge transfer and tetragonal distortion using the Quanty program. This program can solve the many-body problem including the configuration interactions^[31, 175, 202]. The Hamiltonian of a single cluster is written as:

$$H = H_{ionic} + V_{CF} + H_{mix}, \quad (3.1)$$

where H_{ionic} describes the intra-atomic interactions, such as the Coulomb interaction and the spin-orbit coupling. The operator H_{mix} calculates the interaction between the three configurations d^n , $d^{n+1}\underline{L}$, and $d^{n+2}\underline{L}^2$ using the Single Impurity Anderson Model (SIAM)^[175, 194]. This configuration interaction mimics the charge transfer effect. The symmetry characteristic of the target cluster is considered in the operator V_{CF} , which also determines the crystal field energy. For tetragonal distorted clusters, the $3d$ orbitals split into the a_1 , b_1 , e , and b_2 states. The energy splitting of these states can be determined by the additional parameters D_t and D_s in comparison with the unstrained cubic crystal in the simulation^[175]. It induces more degrees of freedom in the parameters to simulate the electronic structure.

To reduce the number of the parameters, we applied constraints by assuming that the local cluster will preserve its volume. This assumption is based on the diffraction results which indicate a $< 3\%$ difference in volume (Table 3.1) of a pseudo-cubic unit cell (CoO₆ cluster). Model calculations were performed using the program MultiX^[31], where the energy levels can be calculated with a spherical Wigner local density approximation(LDA) atomic radial function in a potential environment constructed by point charges^[31, 202]. Assuming that the distortion effect is independent of the electron-electron interaction, we simulated the distortion effect for the case of a single electron in a $3d$ shell ($3d^1$). In this model calculation, the metal-ligand bond (d) was set to 2 Å for a non-distorted cluster ($d \sim 1.9$ Å for SrTiO₃)^[115]. The volume restriction is fixed at $d_x \times d_y \times d_z$

$= 8 \text{ \AA}^3$, where the d_x , d_y , and d_z are the bonds along the x , y , and z axes. Based on the values of energy levels, the crystal field parameters Dq , Ds , and Dt can be extracted [175]. We introduce an effective $10Dq$ ($10Dq_{eff}$) parameter, which is defined as the energy difference between the average energy of the e_g and t_{2g} states, i.e., $10Dq_{eff} = \frac{1}{2}(E_{b_1} + E_{a_1}) - \frac{1}{3}(E_{b_2} + 2E_e)$. The values of Dq , Dq_{eff} , Ds , and Dt of the model calculation are indicated in Fig. 3.5a as a function of the equatorial bond ($d_x = d_y$). The following conclusions can be drawn: i) A negative Ds and Dt values are found for an elongated d_x related to the tensile-strained LaCoO_3 film on SrTiO_3 . ii) Comparing the values Dt and Ds , we find a Dt to Ds ratio ~ 0.15 for the Co ion. iii) $10Dq_{eff}$ is approximately constant (gray lines, Fig. 3.5a). In our simulation, we applied the optimized values of the Slater integrals and $10Dq$ for the unstrained LaCoO_3 crystal [103], using the fixed volume approach for the films. This method allows us to investigate the distortion effect systematically with only

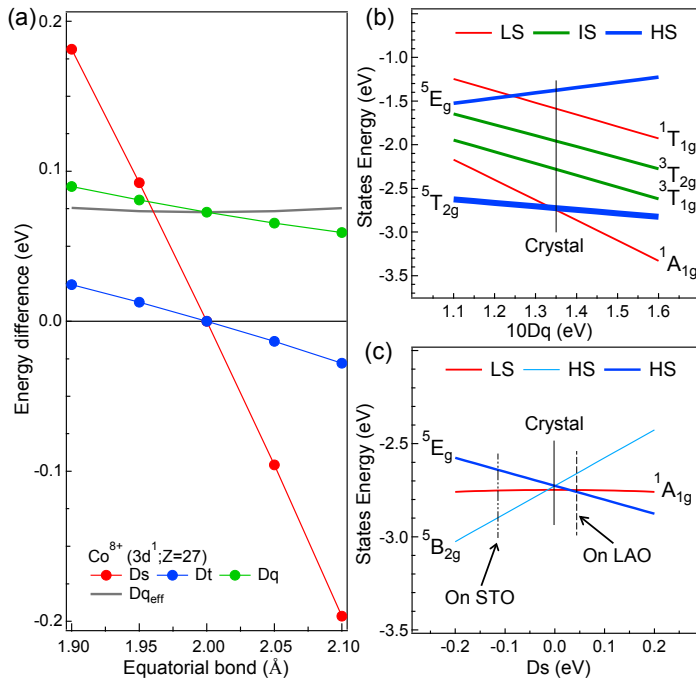


Figure 3.5: (a) The crystal field parameters of the tetragonal distorted Co^{8+} ion. The values were derived from a model calculation in a fixed volume cluster. (b)-(c) The energy diagram without spin-orbit coupling and charge transfer effect. (b) The energy diagram as a function of $10Dq$. (c) The energy diagram as a function of Ds value with a $10Dq=1.35$ eV.

the D_s parameter.

Applying the constraints to multiplet calculations without the charge transfer effect, Fig. 3.5b,c show the energy diagrams. The Slater integrals F_{dd}^2 and F_{dd}^4 were reduced to 50 % and 65 % from atomic values to simulated the screening effect of charge transfer, where $F_{dd}^2=5.065$ eV and $F_{dd}^4=4.117$ eV. The ground state of the relaxed LaCoO_3 is $^1A_{1g}$ state below 20K and its $10Dq$ is close to $10Dq_{cross}$. It gives an optimized $10Dq_{eff}$ at ~ 1.35 eV. Fig. 3.5c displays the energy diagrams in the constraint $\frac{D_t}{D_s} = 0.15$ as a function of D_s . A small distortion switches the ground state symmetry and implies the competition between the $^5B_{1g}(D_{h4})$, $^5E_g(D_{h4})$, and $^1A_{1g}(O_h)$ states. The charge transfer effect will be taken into account and discussed later.

3.4 Experiment Results and Discussions

3.4.1 Experimental Results

Figure 3.6a compares the fluorescence yield XAS spectra acquired from two orthogonal linear polarized incident beams. The linear vertical (V) and horizontal (H) polarized beams are defined by the electric field orientation as illustrated in Fig. 3.6b. During the measurements of the crystal and the films, the (001) and (010) orientations of the samples were placed in the scattering plane. The XAS results (Fig. 3.6a) show that the shoulder above the edge (at ~ 783.5 eV) is higher in the case of the LaCoO_3 single crystal, which can be attributed to the LS $^1A_{1g}(O_h)$ ground state^[97, 130]. The isotropic $^1A_{1g}(O_h)$ state also implies that there is no polarization dependence in the dipole transition, as confirmed by the overlap of the two polarization-dependent spectra. In addition, bulk sensitive fluorescence yield XAS spectra show no characteristic features of Co^{2+} ions^[7, 213], which implies that the presence of Co^{2+} ions can be neglected.

The maximum of the Co L_3 edge was selected for the RIXS measurements because (i) the RIXS intensity is maximal and (ii) the comparison with the calculations is best defined. Using an excitation energy a few eV before the maximum of the Co L_3 edge would yield reduced fluorescence, but we consider the two advantages to outweigh the drawbacks. The excitation energy is indicated as E_{in} in Fig. 3.6a. The experiments were aligned at a grazing incident geometry ($\theta \sim 10^\circ$) with the spectrometer at 90° . Two types of features are identified from the results (Fig. 3.6c): sharp excitonic peaks between 0 and 3 eV and the broad fluorescence feature. The excitations above 3 eV are combinations of charge transfer excitations and fluorescence emission, which were used for normalization. At 20 K, the

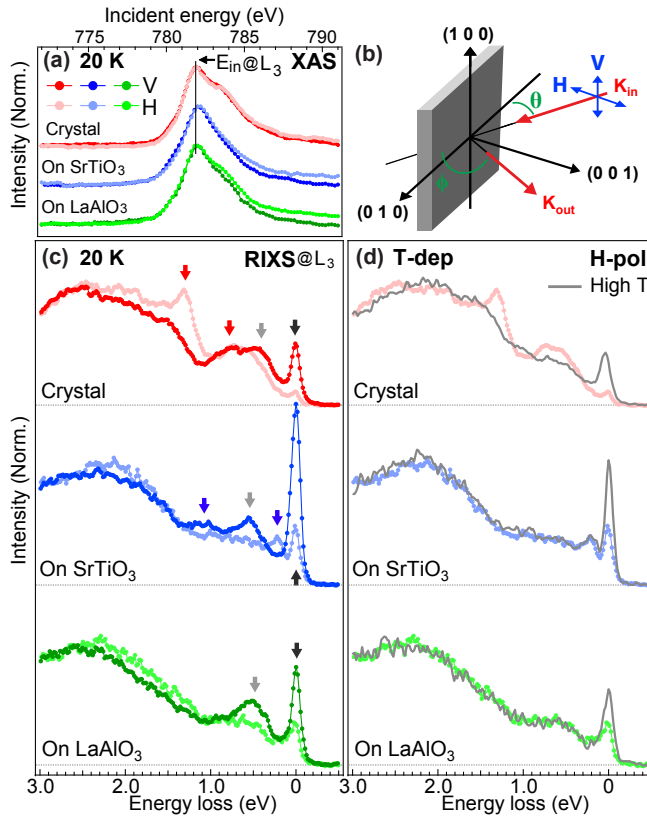


Figure 3.6: (a) The fluorescence yield XAS results. E_{in} indicates the selected incident energy for the RIXS measurement. (b) Illustration of the experimental geometry. (c) Polarised RIXS spectra at the L_3 edge for the LaCoO_3 crystal and the LaCoO_3 films. The dark and light color circles indicate the spectra of V- and H- polarization beams, respectively. The black, red and blue arrows refer to the elastic peak, the characteristic features of the LaCoO_3 single crystal and the characteristic features of the LaCoO_3 film on SrTiO_3 substrate, respectively. The gray arrows indicate the mixture of spin states. (d) The comparison of H-polarization spectra between low temperature (color) and high temperature (gray). The measurements are performed at a temperature 150 K for the films and 300 K for the single crystal.

excitations of the LaCoO_3 single crystal are located at about 0, 0.4, 0.8, and 1.3 eV (arrows in Fig. 3.6c). These features behave differently in the films. The 0.8 eV and 1.3 eV features (red arrows) become weaker or disappear in both films. In addition, the $\text{LaCoO}_3/\text{SrTiO}_3$ film (Fig. 3.6c) shows the appearance of new features at 0.2 eV and 1.1 eV (blue arrows). In particular, the 0.2 eV feature shows a strong

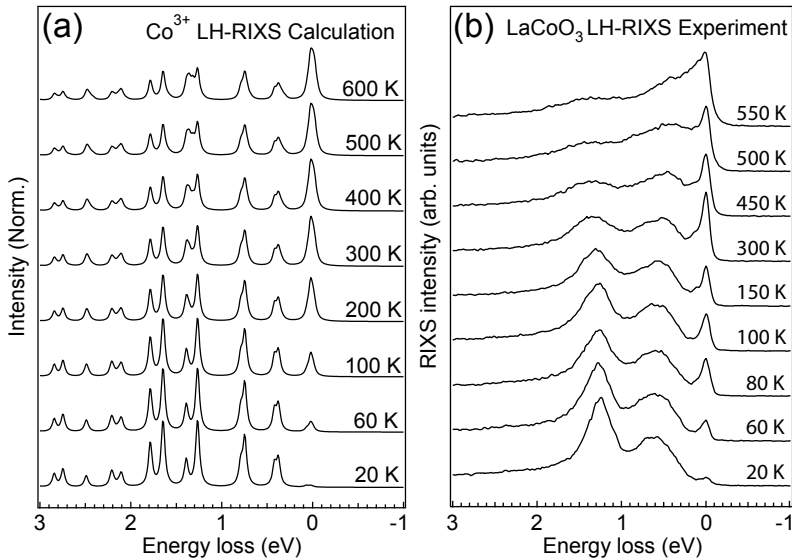


Figure 3.7: The temperature dependent $2p3d$ RIXS spectra. (a) Calculation results. (b) Experimental results. The experimental results are grabbed from the reference [103].

polarization dependence while the LaCoO_3 crystal and the $\text{LaCoO}_3/\text{LaAlO}_3$ film exhibit no feature around 0.2 eV. The gray arrows at ~ 0.4 eV in the Fig. 3.6c might be the contribution of spin state mixtures between HS and LS LaCoO_3 , which will be discussed later.

Figure 3.6d compares the measurements below and above the magnetic transition temperature (~ 70 K). The high temperature measurements were performed at 150 K for the films and at 300 K for the single crystal. The LaCoO_3 single crystal RIXS spectra changes with temperature due to the transition from a pure LS $^1A_{1g}(O_h)$ state to a mixture between the LS $^1A_{1g}(O_h)$ and HS $^5T_{2g}(O_h)$ states^[103]. In contrast, in the strained LaCoO_3 film, no spectral difference is visible except for the elastic peak, implying that the spin state does not change in this temperature region. The elastic peak is enhanced because of the thermal population of lattice vibration excitations (< 20 meV)^[91, 221] or the excitations from thermally excited states within the same $^5B_{2g}(D_{4h})/^5E_g(D_{4h})$ manifold (< 50 meV)^[103]. These quasi-elastic features can not be distinguished due to the resolution limit. We point out that the experimental temperature difference between the single crystal and the films will not influence the discussion, because the effect of spins state change on spectral features has already been observed at ~ 150 K in the single crystal^[103].

This temperature dependent $2p3d$ RIXS spectra of the LaCoO_3 crystal due to the spin state population change can also be simulated through the calculation (see Fig. 3.7). The calculation is described by the SIAM with the interacting parameters identical to those used in reference [103].

3.4.2 Distortion Dependent Calculations

Figure 3.8a presents the energy diagram as a function of the tetragonal distortion parameter D_s with a constant ratio 0.15 between D_t and D_s . The charge transfer parameters are implemented as follows: $U = 6.5$ eV, $Q = 7.5$ eV, $T_{12g} = 1.8$ eV, and $T_{eg} = 3.118$ eV^[103]. The intra-atomic Slater integrals of the $3d$ states were 92.5% from the atomic values ($F_{dd}^2 = 9.371$ eV and $F_{dd}^4 = 5.859$ eV) and the $3d$ spin-

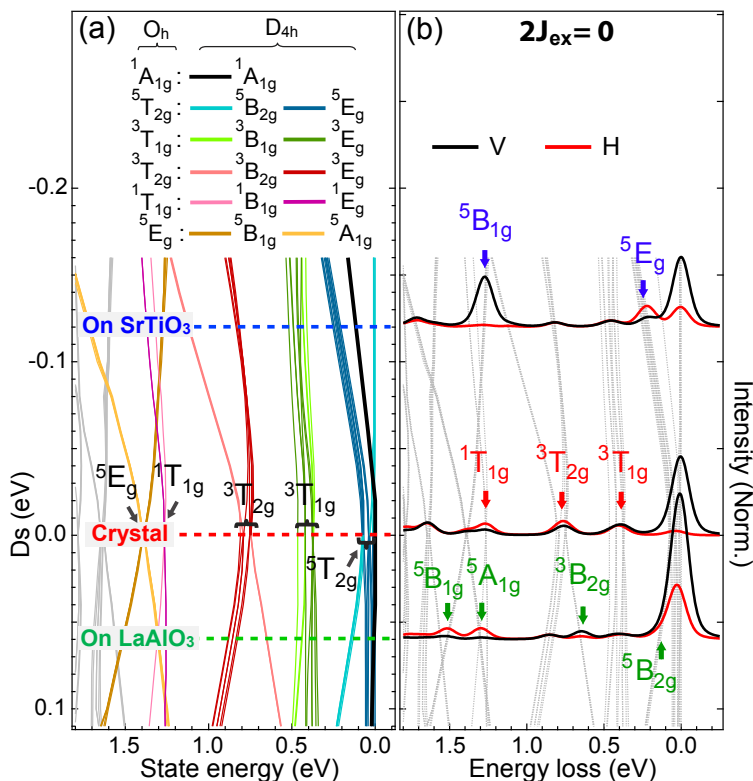


Figure 3.8: The calculation of (a) the energy diagram and (b) the RIXS spectra as a function of the distortion parameter D_s . The red, blue and green arrows refer to the characteristic features of the LS $1A_{1g}(O_h)$, HS $5B_{2g}(D_{4h})$ and HS $5E_g(D_{4h})$ ground states, respectively.

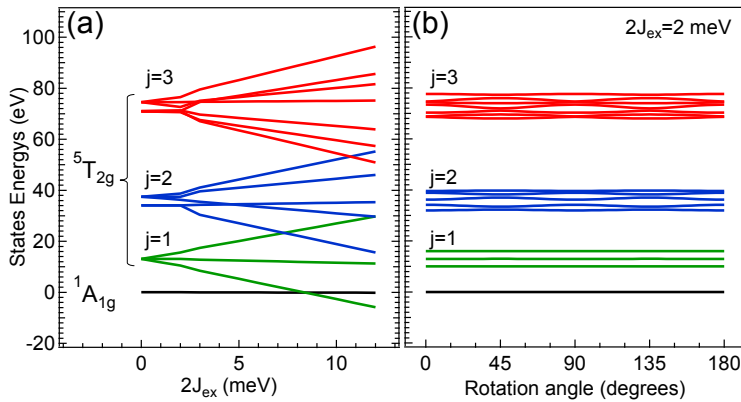


Figure 3.9: (a) The energy diagram of $^1A_{1g}(O_h)$ and $^5T_{2g}(O_h)$ states as a function of $2J_{ex}$ value. (b) The energy diagram of $^1A_{1g}(O_h)$ and $^5T_{2g}(O_h)$ states as a function of $2J_{ex}$ rotation angle along \mathbf{y} axis, where $|2J_{ex}|$ is fixed at 2 meV.

orbit coupling was 55 meV. The charge transfer effect decreases the ionic $10Dq$ value to 0.595 eV and provided an additional ligand $10Dq$ to a value $\sim 0.595/3$ eV. Figure 3.8a shows that the $^5B_{2g}(D_{4h})$ and $^5E_g(D_{4h})$ splittings of the $^5T_{2g}(O_h)$ excited state change to the ground state when the distortion is applied. The $^3T_{1g}(O_h)$ excited state splits into $^3E_g(D_{4h})$ and $^3B_{1g}(D_{4h})$ states. This $^3T_{1g}(O_h)$ excited state is located at about 0.4 eV and show no strong tetragonal distortion dependence. In contrast, the $^3T_{2g}(O_h)$ excited state is more sensitive to the distortion effect and splits into $^3E_g(D_{4h})$ and $^3B_{2g}(D_{4h})$ states. The rotation distortion has been neglected because it is beyond the ability of a cluster calculation, where we note that a change in the ground state symmetry requires a value of $|2J_{ex}|$ larger than 8 meV, as indicated in Fig. 3.9a. The magnetic exchange splittings are independent of the orientation of the $2J_{ex}$, see Fig. 3.9b. Note that if the rotation distortion can increase the exchange interaction, it means that other exchange mechanisms might be involved to enlarge the $|2J_{ex}|$ value.

The 0.2 eV feature in the $\text{LaCoO}_3/\text{SrTiO}_3$ film is determined by a D_s value of ~ -0.12 eV (blue dashed line). The D_s value for the $\text{LaCoO}_3/\text{LaAlO}_3$ film is estimated at ~ 0.06 eV (cf Table 3.1) using linear extrapolation. These values are slightly larger than the values estimated from our fixed volume approach ($D_s \sim 0.04$ eV for a 1% mismatch, cf Fig. 3.5c), which is partly caused by the symmetry breaking of the octahedral charge transfer. Breaking the symmetry of the charge transfer hopping will introduce an additional state splitting, which leads to larger D_s values. Figure 3.8b displays the calculation of the $2p3d$ RIXS spectra

with respect to different distortion values. We used 0.05 eV Lorentzian broadening convoluted with a 0.10 eV Gaussian broadening in fwhm. The broadening of the incident energy was simulated by a convoluted broadening of 0.3 eV Lorentzian broadening and 1.0 eV Gaussian broadening in fwhm to simulate the wide incident energy window of the AGM-AGS system. The calculations have been performed on the maximum of the L_3 resonant edge of V-polarization beam and all the intensities were normalized to the total intensity of charge transfer features. An important observation is that positive and negative Ds exhibit different polarization dependence of the excitons.

In Fig. 3.8b, the peak of zero energy loss indicates the transition back to the ground state. The features corresponding to the ${}^3T_{1g}(O_h)$, ${}^3T_{2g}(O_h)$ and ${}^1T_{1g}(O_h)$ excited states originating from an ${}^1A_{1g}(O_h)$ ground state can be observed (red arrows) with weak polarization dependence. For a ${}^5B_{2g}(D_{4h})$ ground state, the ${}^5E_g(D_{4h})$ excited state at ~ 0.2 eV is enhanced by H-polarized incident photon. Another noticeable feature is the ${}^5B_{1g}(D_{4h})$ excited state, which shows similar polarization selectivity as the ${}^5B_{2g}(D_{4h})$ ground state. In contrast, a ${}^5E_g(D_{4h})$ ground state shows a strong polarization dependence of the zero energy loss peak. Weak polarization dependence appears at ~ 1.3 and ~ 1.5 eV, related to the ${}^5A_{1g}(D_{4h})$ and ${}^5B_{1g}(D_{4h})$ excitations. The dichroic intensity of the ${}^3B_{1g}(D_{4h})/{}^3E_g(D_{4h})$ and ${}^3B_{2g}(D_{4h})/{}^3E_g(D_{4h})$ excitations are weak (Fig. 3.8b).

According to the XAS spectra, the composition of Co^{2+} is negligible because

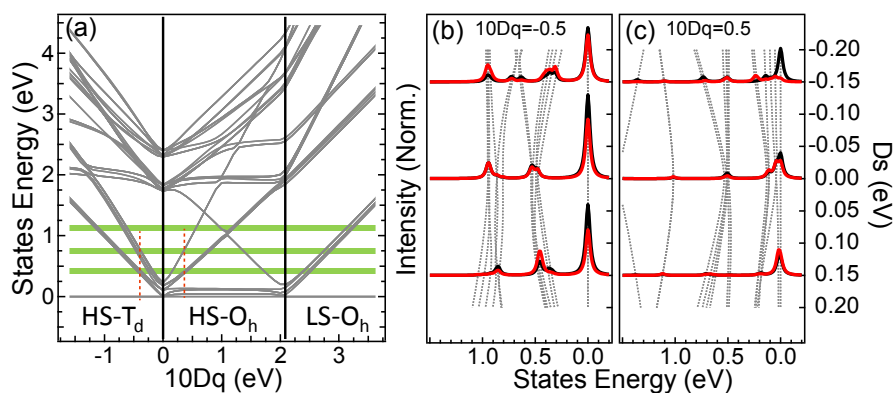


Figure 3.10: (a) The Co^{2+} energy diagram as a function of $10Dq$ with including two ligand hole configurations. Black vertical lines indicate the crossover point and the green horizontal lines indicate the energies at about 0.4, 0.8, and 1.3 eV. (b)-(c) The energy diagram and the spectra with respect to the Ds values when (b) $10Dq = -0.5$ eV and (c) 0.5 eV.

only a small amount (less than 1%) could be observed. Here, we examine the distortion effect on $2p3d$ RIXS spectra of the Co^{2+} ions. Figure 3.10a presents the non-distorted Co^{2+} calculations as a function of $10Dq$. The Slater integrals F_{dd}^2 and F_{dd}^4 were both reduced to 90 % from atomic values to simulated the small screening effect, where $F_{dd}^2=8.356$ eV and $F_{dd}^4=5.191$ eV. The ground state of the system switches from a HS ${}^4A_{1g}(T_d)$ state through a HS ${}^4T_{1g}(O_h)$ state to a LS ${}^2E_g(O_h)$ state. By comparing to the experimental results, two optimized cases could be taken into account: $10Dq \sim -0.5$ eV and 0.5 eV (red dash lines in Fig. 3.10a). For a HS ${}^4A_{1g}(T_d)$ state ($10Dq=-0.5$ eV), the orbital singlet ground state has no distortion dependence. In addition, the calculated RIXS features at about 0.4 and 0.8 eV did not show a consistent polarization dependence (Fig. 3.10b) to the experimental results (cf Fig. 3.6). Thus, the tetrahedral Co^{2+} has ruled out from the simulation. In contrast, figure 3.10c show that the distortion effect on the HS ${}^4T_{1g}(O_h)$ state has a good agreement to the experimental behavior, i.e., a negative Ds has stronger H-polarization signal on 0.2 eV feature. However, few lower states ~ 100 meV should be observed and also the higher energy excited states do not match the experimental result well.

3.4.3 Comparison of L_3 Edge Results

The simulation in Fig. 3.8b seems to overestimate the polarization dependence of the ${}^5B_{1g}(D_{4h})$ excitation of the ${}^5B_{2g}(D_{4h})$ ground state, which is likely related to a mixture of spin states. The spin state mixture has been observed in the tensile D_{2h} and D_{3d} distorted LaCoO_3 and explained as the LS-HS spin state ordering^[116, 117, 125]. Such frozen electron configuration provides long-range ferromagnetic order^[117, 222]. This is consistent with the TEM observation of a defect structure which suggests $\sim 40\%$ tetragonal distorted Co^{3+} ions on SrTiO_3 substrates^[127]. This defect structure generates an in-plane 3×1 supercell^[128]. For $\text{LaCoO}_3/\text{LaAlO}_3$ film, a similar defect structure has been observed by dark lines running parallel to the surface^[124, 127]. This indicates that the LS-HS spin state ratio is approximately 2 to 1 in both the tensile- and compressive-strained LaCoO_3 films.

Figure 3.11 compares experimental dichroism spectra with the simulations. The spectra of the LaCoO_3 single crystal at 20 K can be simulated well by a pure ${}^1A_{1g}(O_h)$ state^[97, 103, 125]. For the tensile-strained $\text{LaCoO}_3/\text{SrTiO}_3$ film, the simulated spectra are the summation of the LS ${}^1A_{1g}(O_h)$ state and the HS ${}^5B_{2g}(D_{4h})$ state with a composition ratio 2:1. The dichroism feature at ~ 0.2 eV is reproduced and the dichroism intensity of the ${}^5B_{1g}(D_{4h})$ is larger in calculations compared

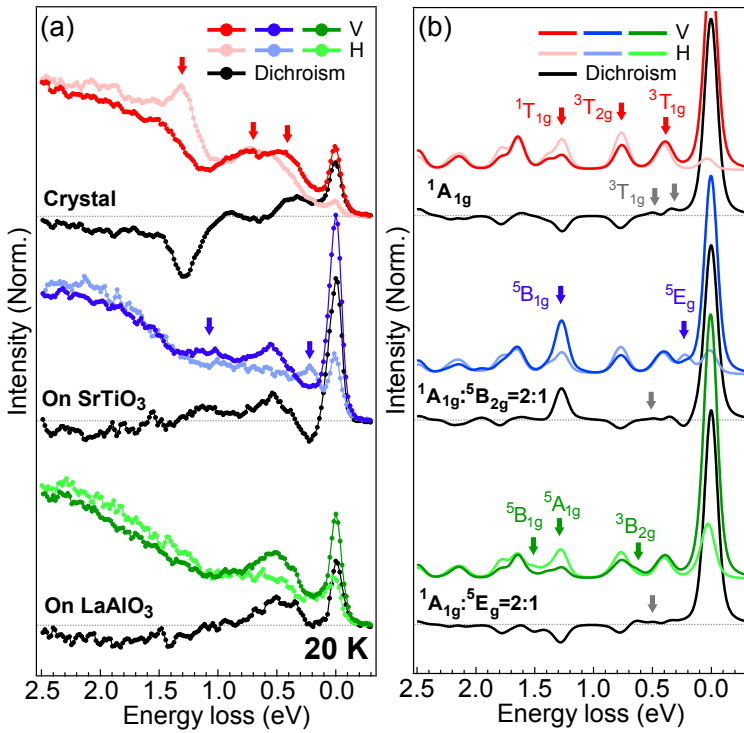


Figure 3.11: The comparison of dichroism spectra. (a) Experiment and (b) simulation. The red, blue and green arrows refer to the characteristic features LS ${}^1A_{1g}(O_h)$, HS ${}^5B_{2g}(D_{4h})$ and HS ${}^5E_g(D_{4h})$ ground states, respectively. The gray arrows indicate the possible of spin state mixture as discussed in the text.

with experiment. Comparing the RIXS dichroism spectra on $\text{LaCoO}_3/\text{LaAlO}_3$ film, there is no dichroism feature in the low energy region as compared to the $\text{LaCoO}_3/\text{SrTiO}_3$ sample, which is in agreement with the simulation. Increasing the LS state population, the dichroism intensity of the films in the energy region between 0.2 and 1.0 eV (gray arrows) can also be improved. The mixed spectrum shows better agreement which implies the existence of spin state mixtures and suggests that the HS Co^{3+} can be the trigger of long-range ferromagnetic order. Some discrepancies remain related to the fact that (i) $10D_{q_{eff}}$ was constrained to a constant in all the cases, while the position of high energy excitations are changed when different $10D_{q_{eff}}$ values are applied; (ii) In tetragonal symmetry the ${}^3T_{1g}(O_h)$ state splits into the ${}^3B_{1g}(D_{4h})$ and ${}^3E_g(D_{4h})$ states, which can yield different dichroism intensity with respect to the excitation in octahedral symmetry.

According to the simulated results, the effective magnetic moments $\mu_{eff} = 3.8$,

4.1, and 4.2 (μ_B/Co) are obtained at 150 K for the single crystal, the SrTiO₃ film and the LaAlO₃ film respectively. The effective magnetic moments μ_{eff} of the transition metal oxides are approximately equal to $g \times \sqrt{S_{\text{tot}}(S_{\text{tot}} + 1)}$, where $g \sim 2$ and the total spin moments S_{tot} were obtained by the state population at certain temperature. The μ_{eff} of the LaCoO₃/SrTiO₃ film shows a good agreement with the experimental value ~ 4.6 ^[115]. The μ_{eff} are respectively ~ 1.96 for the LaCoO₃ single crystal (~ 3.1 in another reference [66]) and 3.2 for the LaCoO₃/LaAlO₃ film, which are smaller than our values. The μ_{eff} value of the LaCoO₃/LaAlO₃ film is slightly larger because the $D_s \sim 0.06$ eV is closer to the LS-HS crossover (cf Fig. 3.8b). It implies that a small 10Dq fluctuation might flip the ground state from the HS ${}^5E_g(D_{4h})$ state to the LS ${}^1A_{1g}(D_{4h})$ state and decrease the average μ_{eff} . In addition, when the t_{2g} splitting is close to the $3d$ spin-orbit coupling, the possibility of unquenched orbital moments in Co³⁺ HS with D_{4h} symmetry competes with the exchange interaction in C_4 symmetry, which leads to an overestimation of the effective moment. Furthermore, the spin state distribution of bulk LaCoO₃ might be influenced by the collective behavior of IS excited state^[214], which will also reduce the theoretical μ_B value of bulk LaCoO₃.

3.4.4 Energy Dependent RIXS Spectra

Figure 3.12 shows the experimental and simulated spectra excited at L_3 edge and $L_3 \pm 2$ eV, using the same theoretical models. The fine structures are more pronounced at $L_3 - 2$ eV due the suppressed fluorescence features experimentally^[103], but the pre-edge RIXS spectrum is sensitive to the small resonant features which bias the adjustment of the energy in the simulation. Such difficulty can also be found in the high quality XAS results^[97]. These resonant features are hidden in the tail of the absorption maximum and modify the calculations. For better determination of the energies in order to discuss more precise simulation parameters, a fine step energy map is required. In the Fig. 3.12a, a feature at 0.2 eV appears which is always enhanced by the H-polarized incident photon. This observation agrees with the simulation results (Fig. 3.12c). In addition, when we excite at the absorption maximum (L_3 edge), the feature of the ${}^5B_{1g}(D_{4h})$ excited state is enhanced by V-polarized incident photon and pronounced at about 1.1 eV in experiment and 1.3 eV in simulation. The energy discrepancy could be compensated by manipulating the $10Dq_{\text{eff}}$, which is constrained to a constant in our model. Whereas, the LaCoO₃/LaAlO₃ film (Fig. 3.12b) shows similar RIXS dichroism intensity of 1.3 eV feature to the bulk sample but no new feature at low energy region. The presence of the 1.3 eV feature in the LaCoO₃/LaAlO₃ film

might be contributed by two sources of ${}^1A_{1g}(O_h)$ ground state as well as ${}^5E_g(D_{4h})$ ground state. It suggests a mixture of spin states as previously discussed, which matches the simulation (Fig. 3.12d).

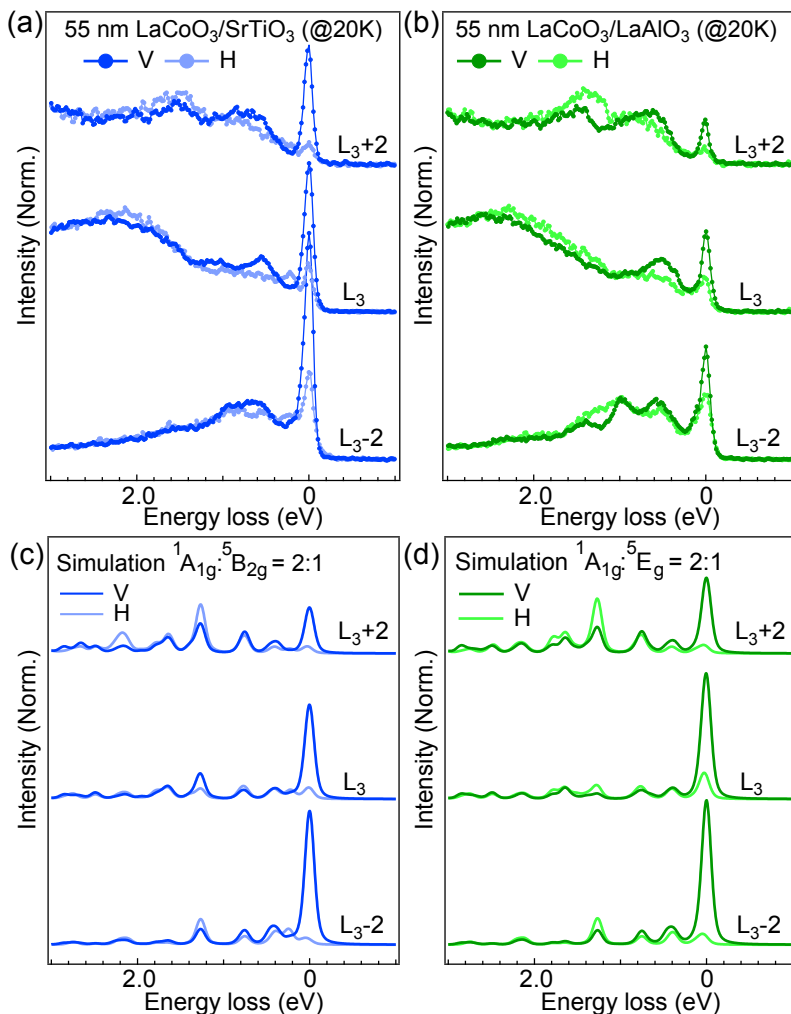


Figure 3.12: (a)-(b) The energy dependent RIXS spectra of the 55 nm LaCoO₃ films on the (a) SrTiO₃ substrate and (b) LaAlO₃ substrate. (c)-(d) The simulation for the mixture of (c) ${}^1A_{1g}(O_h)$ and ${}^5B_{2g}(D_{4h})$ states and (d) ${}^1A_{1g}(O_h)$ and ${}^5E_g(D_{4h})$ states.

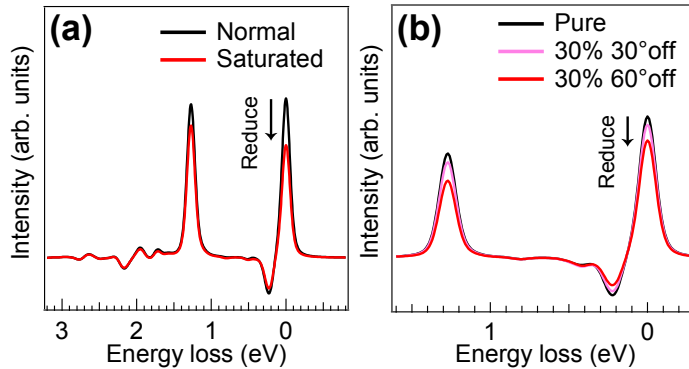


Figure 3.13: The comparison of the simulated dichroism spectra (a) with considering the saturation and self-absorption effect and (b) with considering the orientation off-aligned defects. The calculation is tested for the optimized case $D_s = -0.12\text{eV}$.

3.4.5 Saturation of the Elastic Peak

In Fig. 3.11, the RIXS intensity near the zero loss region is lower in the experiments than in the calculations. A possible reason for this discrepancy is the energy dependent self-absorption effect. The RIXS intensity is influenced by the absorption factor of the incident and the emitted photon. For a larger absorption factor, the spectra will be more saturated. Figure 3.13a shows the simulation of this state-dependent saturation effect. The zero energy line of the L_3 edge RIXS spectra has an emitted photon energy equal to the maximum of the L_3 edge, which shows the strongest intensity saturation due to self-absorption. In contrast, the high energy loss region features show less saturation effect, which also establishes that normalizing to the fluorescence feature is a valid approach.

Another reason for the discrepancy between the experimental data and the calculations can be that all the CoO_6 clusters are assumed to be well aligned to the pseudo-cubic orientation (002). The combination effect of octahedron rotation and octahedron deformation might reflect on the polarization dependence of spectra although the octahedron rotation does not change the ground state symmetry. Experimentally, not all the CoO_6 clusters will be aligned exactly to the pseudo-cubic orientation, for instance, the strain-induced rotational modifications observed by TEM. These rotational variations lead to the mixture of different polarization dependent effects, see Fig. 3.13b. By including the off-aligned tetragonal field, both the elastic and the ${}^5B_{1g}$ ($\sim 1.3\text{ eV}$) features decrease the intensity. It brings the simulated result of the $\text{LaCoO}_3/\text{SrTiO}_3$ film closer to the experiments.

On the other hand, in the case of the LaCoO₃/LaAlO₃ film, the (average) lattice constant appears to deviate slightly from the single crystal, which implies that the relaxed fraction might be larger and less sensitive to the rotation effect.

3.5 Conclusions

2p3d RIXS dichroism can be used to determine the nature of the ground state. Using linear dichroism analysis, we show that the Co³⁺ ions are dominated by the ¹A_{1g}(O_h) state in a LaCoO₃ single crystal. Whereas, the tensile- and compressive-strained LaCoO₃ films on SrTiO₃ and LaAlO₃ respectively, contain contributions from the ⁵B_{2g}(D_{4h}) and ⁵E_g(D_{4h}) states. A 0.2 eV excitation was observed in the tensile-strained LaCoO₃/SrTiO₃ film by *2p3d* RIXS, which is attributed to an orbital excitation from the ⁵B_{2g}(D_{4h}) to the ⁵E_g(D_{4h}) state. No feature appeared at this energy region in the compressive-strained LaCoO₃/LaAlO₃ film. The film spectra show no temperature dependence, implying that the spin state does not change above the transition temperature (~70K). Although some features were not simulated perfectly, the composition mixture effect fits the existing picture of strain-induced differences. Bulk sensitive fluorescence yield XAS shows no Co²⁺ features, therefore the data suggests that the HS Co³⁺ can be the trigger of long-range ferromagnetic order due to the possible existence of quantum-chemical mixed spin states.

Appendix: The RIXS simulations and slice selection

The energy map of the simulations are presented in Fig. 3.14). In order to compare this simulation to the experimental results, the energy slices of the maximum L_3 edge have been chosen as the excitation of the V-polarization beam (the green dashed lines in Fig. 3.14). All the intensities were normalized to the total intensity of the charge transfer features of these cutting slices.

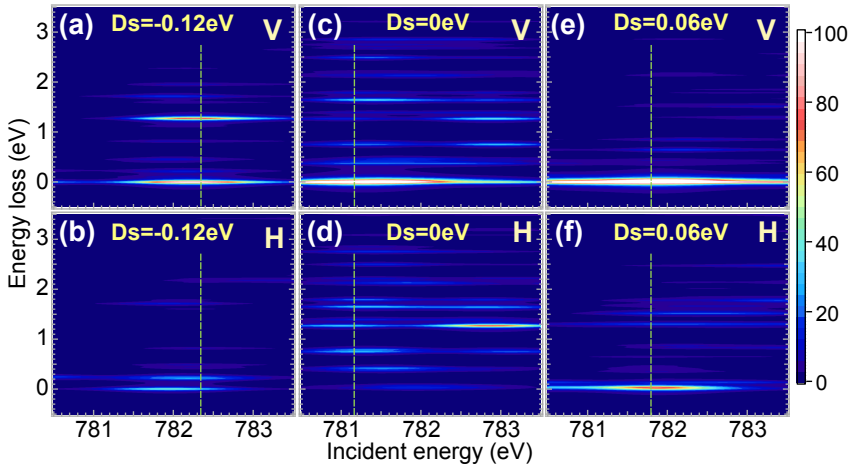


Figure 3.14: (a)-(b) The simulated RIXS energy contour for (a)-(b) $D_s = -0.12$ eV, (c)-(d) $D_s = 0.0$ eV, and (e)-(f) $D_s = 0.06$ eV. The top and bottom panels are the simulations corresponding to the V- and H-polarization incident beam, respectively.

Chapter 4

Angular Dependence and Self-absorption of $2p3d$ RIXS in LaCoO_3

In chapter 3 I have shown that the difference between two orthogonal linearly polarized incident beams provides more details about the ground state characteristics. In this chapter, I present the angular dependent analysis of $2p3d$ resonant inelastic X-ray scattering ($2p3d$ RIXS) of the LS- $^1A_{1g}(O_h)$ and HS- $^5B_{2g}(D_{4h})$ ground states. The polarization dependence is not only determined by the difference between two orthogonal linearly polarized incident beams but also influenced by the experimental geometry. Through the crystal field theory calculation including the ligand to metal charge transfer (LMCT) effect, I show theoretically that with the ~ 20 meV resolved Co $2p3d$ RIXS, the $3d$ spin-orbit splitting excitation states of $^1A_{1g}(O_h)$ ground states can be distinguished according to the geometry setting. In combination with the self-absorption correction, the angular dependence caused by the saturation effect can be simulated. Strong saturation distorts the spectra of the LaCoO_3 single crystal and limits the observation of small dependence of the spin-orbit splitting excitation states. In contrast, the RIXS on 55 nm LaCoO_3 shows less self-absorption effects and preserves the angular dependence of the excitation states.

4.1 Introduction

Resonant inelastic X-ray scattering (RIXS) is a developing technique to investigate the ground and excited states with its angular degree of freedom. Its scattering cross-section is based on the Kramers-Heisenberg formula^[19] which shows that RIXS is a technique sensitive to the experimental geometry involving the beam polarization as well as the material symmetry. The geometry sensitivity of the *L*- and *M*- edge RIXS has been examined by Michel van Veenendaal theoretically for the one hole or one electron case^[32]. Based on it, one is able to emphasise the particular transitions of *d*-states with their spin characteristics at a certain polarization or geometry setting for RIXS. Marco Moretti Sala *et al.* applied this property in the perovskite cuprates to determine the crystal field energy^[31]. By including the spin-orbit coupling, super-exchange field ($2J_{ex}$), or external magnetic field, the system symmetry is further reduced^[4]. This implies that RIXS can even have the fine structure selectivity of the spin-orbit coupling for multi-electron cases.

In this chapter, we discuss the angular dependent $2p3d$ RIXS. The target samples are the LaCoO_3 single crystal and the 55 nm LaCoO_3 film on the SrTiO_3 substrate ($\text{LaCoO}_3/\text{SrTiO}_3$ film). In an ionic limit, the angular dependent $2p3d$ RIXS can probe the excitations within the $3d^6$ manifold of a Co^{3+} ion with their charge, orbital, and spin characteristic. In addition, a model is proposed to describe the intensity correction for the saturation and self-absorption effects. RIXS can be explained from two processes: absorption (*photon-in*) and emission (*photon-out*). The absorption process excites the electrons to the higher energy levels and the emission process emits the photons when the electrons decay to the lower energy levels. Two effects are found here: (i) The probing depth is dependent on the XAS cross section (saturation) and (ii) the emitted photons are re-absorbed (self-absorption). Consequently, the emitting intensity might be distorted according to the photon energy and the system geometry. This saturation and self-absorption effect is a well-known behavior which introduces the energy and angular dependence in fluorescence yield X-ray absorption spectroscopy (XAS)^[223–229]. As such, it also distorts the RIXS spectra.

4.2 Theory

4.2.1 The Kramers-Heisenberg Equation

The energy and angular dependent RIXS cross-section is determined by the Kramers-Heisenberg equation which is written as^[19]:

$$F_{\text{RIXS}}(\omega_{\text{in}}, \omega_{\text{out}}) = r_e^2 \frac{\omega_{\text{out}}}{\omega_{\text{in}}} \sum_f |A_f(\omega_{\text{in}})|^2 \delta(\omega_{\text{in}} + E_g - \omega_{\text{out}} - E_f). \quad (4.1)$$

The scattering amplitude $A_f(\omega_{\text{in}})$ is given as:

$$A_f(\omega_{\text{in}}) = \sum_m \frac{\langle f|V_E|m\rangle \langle m|V_I|g\rangle}{\omega_{\text{in}} + E_g - E_m + i\Gamma} = \langle f|V_E G(\omega_{\text{in}}) V_I|g\rangle. \quad (4.2)$$

Here ω_{in} and ω_{out} are the energies of the incident and the emitted photons; E_g , E_f , and E_m are the eigenvalues of respectively the ground state $|g\rangle$, the final state $|f\rangle$, and the intermediate state $|m\rangle$; Γ gives the lifetime broadening of the intermediate state. The $V_I(V_E)$ is the transition operator induced by the electric-magneto field of the photon and can be expanded as $\epsilon_I \cdot \mathbf{P}_I e^{ik_I \cdot r_I} (\epsilon_E \cdot \mathbf{P}_E e^{ik_E \cdot r_E})$. For the $2p3d$ RIXS, the $2p3d(3d2p)$ transition operator are approximated as an electric dipole operator $\epsilon_I \cdot P_I (\epsilon_E \cdot P_E)$ for the absorbed (emitted) channel, i.e. $e^{ik_I \cdot r_I} (e^{ik_E \cdot r_E}) \sim 1$. Note that we can omit the scattering coefficient $r_e^2 \frac{\omega_{\text{out}}}{\omega_{\text{in}}}$ in the equation because $\frac{\omega_{\text{out}}}{\omega_{\text{in}}} \sim 1$ for $2p3d$ - $3d2p$ RIXS and the classical electron radius r_e is a constant.

For better understanding of the angular dependence, many authors have already reformulated the scattering amplitude using the spherical tensor expansion, where the cross-section formula of $2p3d$ RIXS is written as [32, 230, 231]:

$$A_f(\omega_{\text{in}}) = P_{dipole}^2 \sum_{Q=0}^2 \sum_{q=-Q}^Q G(\omega_{\text{in}}) T_{Qq}(\epsilon_E, \epsilon_I) \langle f|W_{Qq}|g\rangle. \quad (4.3)$$

Van Veenendaal pointed out that the cross-section now is described by the effective dd transition operators W_{Qq} from a $3d^n$ ground state to another $3d^n$ final state with a polarization weighting factor $T_{Qq}(\epsilon_E, \epsilon_I)$ [32]. The W_{Qq} is an one particle operator which is constructed by the orbital- and spin-dependent tensors. The system geometry (Fig. 4.1a) reflects on the polarization tensors $T_{Qq}(\epsilon_E, \epsilon_I)$. The P_{dipole} are the reduced matrix element between the $2p$ (core) and $3d$ (valence) levels.

In our simulation, all the vectors are described by the axes of the crystal field operator, which are the axes **a**, **b** and **c** as indicated in the figure. Because no polarization analyzer was used in the measurement, we considered isotropic emitted photons that were composed by the summation of two orthogonal linear polarized beams[231]. The possible final excited states $|f\rangle$ can be obtained from cluster calculation[20, 175]. For bulk LaCoO_3 , the Co^{3+} shows rather pure ${}^1A_{1g}(\text{O}_h)$ configuration at 20K. We assume that the Co^{3+} ion is surrounded in an O_h crystal field, where we employed the parameters from reference [103]. For

the LaCoO₃/SrTiO₃ film, we used the optimized parameters as given in chapter 3, which provided a ⁵B_{2g}(D_{4h}) ground state. Figure 4.1b shows the excited states with their term symbols of the ¹A_{1g}(O_h) and the ⁵B_{2g}(D_{4h}) configurations. Because the super-exchange field (2J_{ex}) is small in both cases, we ignored its contribution.

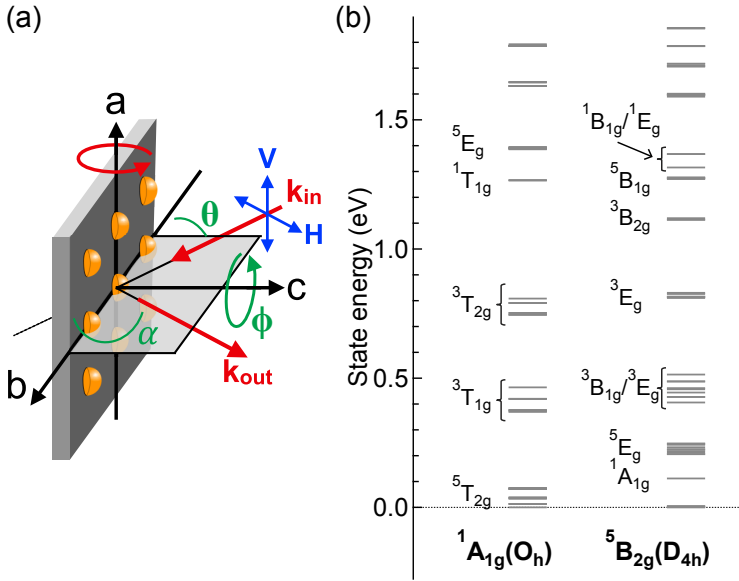


Figure 4.1: (a) The illustration for the geometry and the rotations. (b) The excited states with their term symbols of the LS-¹A_{1g}(O_h) and HS-⁵B_{2g}(D_{4h}) ground states.

4.2.2 Saturation and Self-absorption Effects

The energy and angular dependent RIXS intensity will be influenced by the saturation and self-absorption effects. Constant flux of incoming photons is assumed and denoted by I_0 . The flux of the transmitted beam after a distance l in the sample is denoted by $I_T(l)$, where the boundary condition is $I_T(0) = I_0$. In the absorption process, the absorbed photons (I_{abs}) within a small distance Δl at the position l can be described as a multiplication of absorption factor ($\mu(\omega_{in})$), which is written as:

$$I_{abs} = \mu(\omega_{in})I_T(l)\Delta l. \quad (4.4)$$

On the other hand, we also can describe such absorption process by making the difference between the photon flux after and before the beam pass through the same

small distance Δl . So I_{abs} is also written as:

$$I_{abs} = I_T(l) - I_T(l + \delta l). \quad (4.5)$$

Combining the Eq. 4.4 and 4.5, we get:

$$I_T(l + \delta l) - I_T(l) = \Delta I_T(l) = -I_{abs} = -\mu(\omega_{in})I_0\Delta l. \quad (4.6)$$

When the Δl is approaching to an extreme small value, i.e. $\Delta l \rightarrow dl$ and $\delta I_T(l) \rightarrow dI_T(l)$, then the Beer-Lambert law is obtained by integrating the equation:

$$I_T(l) = I_T(0)e^{-\mu(\omega_{in})\cdot l} = I_0e^{-\mu(\omega_{in})\cdot l}. \quad (4.7)$$

If there is an angle between the incident photon and the sample surface, indicated by θ in Fig. 4.2a, the path l is replaced by the absorbed depth d ($l = \frac{d}{\sin\theta}$) and Eq. 4.7 is rewritten into:

$$I_T(d) = I_0e^{-\mu(\omega_{in})\cdot \frac{d}{\sin\theta}}. \quad (4.8)$$

For the emission process, the total emitted flux from the sample surface to the penetration length l' can be described as following function:

$$I_{ems}(d) = \int_{z=0}^{z=d} dI_S(z) \cdot e^{-\mu(\omega_{out})\cdot l'}. \quad (4.9)$$

The term $dI_S(z)$ stands for the scattering possibility per absorbed photon in a finite distance dz at the a certain depth z . We can expand $dI_S(z)$ into the Eq. 4.4 with a scattering possibility (emission cross-section) $S(\omega_{in}, \omega_{out})$ as:

$$dI_S(z) = S(\omega_{in}, \omega_{out}) \times I_{abs} = S(\omega_{in}, \omega_{out}) \times \mu(\omega_{in})I_T(z) \frac{dz}{\sin\theta}. \quad (4.10)$$

The scattering factor $S(\omega_{in}, \omega_{out})$ describes the scattering possibility for a particular emitted photon energy, which is determined by the state transition possibility. The multiplication $S(\omega_{in}, \omega_{out}) \times \mu(\omega_{in})$ can represent the scattering intensity of RIXS without taking the photon interference into account. We note that the Auger decays or other non-fluorescence channels are also state dependent. They will induce additional scaling factors on the emission intensity. In current case (L edge), those scaling factors are approximated constant. Here, we consider a scattering geometry with an angle offset ($\alpha - \theta$) between scattered beam and sample surface, see Fig. 4.2a. It leads to an angular relation that $l' = \frac{z}{\sin(\alpha - \theta)}$. Equation 4.9 becomes:

$$I_{ems}(d) = \int_{z=0}^{z=d} dI_S(z) \cdot e^{-\mu(\omega_{out})\cdot \frac{z}{\sin(\alpha - \theta)}}. \quad (4.11)$$

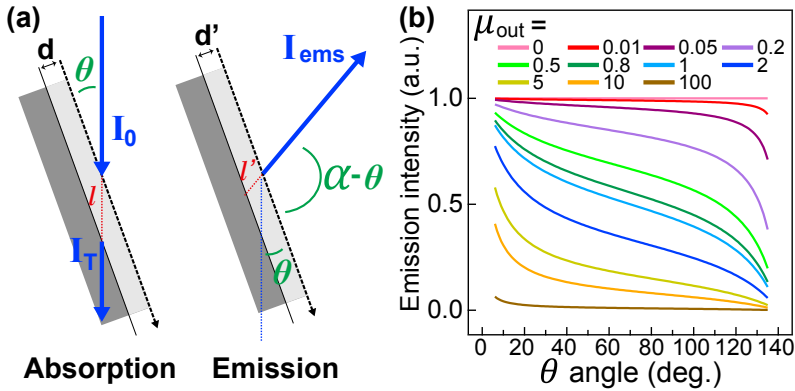


Figure 4.2: (a) The illustration of the geometry for the absorption and emission process. (b) The emission intensity as a function of sample rotation angle θ . The $\mu(\omega_{in})$ here is fixed as one and the $\mu(\omega_{out})$ is scaled from zero to infinity to simulated the trends.

Then the general equation of the emission intensity including the self-absorption effect is derived:

$$\begin{aligned}
 I_{ems}(d) &= \int_{z=0}^{z=d} S(\omega_{in}, \omega_{out}) I_0 \mu(\omega_{in}) e^{-\mu(\omega_{in}) \cdot \frac{z}{\sin\theta}} \frac{dz}{\sin\theta} \cdot e^{-\mu(\omega_{out}) \cdot \frac{z}{\sin(\alpha-\theta)}}. \\
 &= I_0 \frac{S(\omega_{in}, \omega_{out}) \mu(\omega_{in})}{\sin\theta} \int_{z=0}^{z=d} e^{-z \left(\frac{\mu(\omega_{in})}{\sin\theta} + \frac{\mu(\omega_{out})}{\sin(\alpha-\theta)} \right)} dz \\
 &= I_0 \frac{S(\omega_{in}, \omega_{out}) \mu(\omega_{in})}{\sin\theta} \frac{1}{\frac{\mu(\omega_{in})}{\sin\theta} + \frac{\mu(\omega_{out})}{\sin(\alpha-\theta)}} \times \left(1 - e^{-d \left(\frac{\mu(\omega_{in})}{\sin\theta} + \frac{\mu(\omega_{out})}{\sin(\alpha-\theta)} \right)} \right).
 \end{aligned} \tag{4.12}$$

This equation has been discussed and applied on XAS spectra in several articles [223–229]. Most of those cases has been summed over the emitted photon energy, which implies that the absorption factor $\mu(\omega_{out})$ is approximately constant. However, it is not constant in RIXS because the emitted photon energy is analyzed.

Self-absorbed free. If the sample thickness is much smaller than the attenuation length, i.e. $d \rightarrow 0$, we can approximate the exponential function $e^{-x} \sim 1 - x$. Then we obtain:

$$\begin{aligned}
 I_{ems}(d \rightarrow 0) &\simeq I_0 \frac{S(\omega_{in}, \omega_{out}) \mu(\omega_{in})}{\sin\theta \times \left(\frac{\mu(\omega_{in})}{\sin\theta} + \frac{\mu(\omega_{out})}{\sin(\alpha-\theta)} \right)} \times \left(1 - \left(1 - d \left(\frac{\mu(\omega_{in})}{\sin\theta} + \frac{\mu(\omega_{out})}{\sin(\alpha-\theta)} \right) \right) \right) \\
 &= I_0 \mu(\omega_{in}) S(\omega_{in}, \omega_{out}) \frac{d}{\sin\theta}.
 \end{aligned} \tag{4.13}$$

Equation 4.13 shows that the emission intensity is proportional to the incoming photon flux I_0 , the absorption factor of incident beam $\mu(\omega_{in})$, the scattering factor $S(\omega_{in}, \omega_{out})$, the sample thickness d , and the angle θ . Note that the $\mu(\omega_{in})$ and $\mu(\omega_{out})$ are the total absorption factors at the certain energy ω_{in} and ω_{out} , which are the summation factors over all element “X”, i.e. $\mu(\omega) = \sum_X \mu_X(\omega)$ and $S(\omega_{in}, \omega_{out}) = \sum_X S_X(\omega_{in}, \omega_{out})$. Here X can be cobalt, oxygen or the other element. In a good approximation, the RIXS intensity is proportional to the multiplication of absorption and emission cross-sections, which are the factors $\mu(\omega_{in})$ and the $S(\omega_{in}, \omega_{out})$, respectively. Thus the total intensity of RIXS shows no self-absorption and only depends on d and θ for the self-absorbed free case. This approximation is also applied to ultra-thin films or dilute specimens to claim no saturation effect for the fluorescence yield X-ray absorption spectrum. The multiplication will become $\mu(\omega)S(\omega_{in}, \omega_{out}) = \sum_X \mu_X(\omega)S_X(\omega_{in}, \omega_{out})$ if the interference is ignored. Then the Eq. 4.13 is expressed as:

$$I_{ems}(d \rightarrow 0) = I_0 \sum_X \mu_X(\omega_{in}) S_X(\omega_{in}, \omega_{out}) \frac{d}{\sin\theta}. \quad (4.14)$$

For the Co L_3 edge, the spectrum is proportional to the multiplication of the $\mu_{Co}(\omega_{in})$ and the $S_{Co}(\omega_{in}, \omega_{out})$. The state dependent scattering possibility implies that the partial fluorescence yield X-ray absorption is not identical to the normal absorption spectrum. Liu *et al.* show good agreement of such state dependent behavior between the experimental and calculated results in dilute specimens^[232]. If the $S_{Co}(\omega_{in}, \omega_{out})$ is approximated constant, the scattered spectrum is equivalent to the absorption spectrum $\mu_{Co}(\omega_{in})$.

Fully absorbed. If d becomes infinity, the incident photons are fully absorbed. Thus the exponential term in the Eq. 4.12 becomes zero. Then we obtain the scattering intensity as a function of the photon energy and the sample geometry:

$$\begin{aligned} I_{ems}(d \rightarrow \infty) &= I_0 \sum_X \frac{S_X(\omega_{in}, \omega_{out}) \mu_X(\omega_{in})}{\sin\theta} \frac{1}{\frac{\mu(\omega_{in})}{\sin\theta} + \frac{\mu(\omega_{out})}{\sin(\alpha-\theta)}} \\ &= I_0 \sum_X S_X(\omega_{in}, \omega_{out}) \mu_X(\omega_{in}) \frac{1}{\mu(\omega_{in}) + \mu(\omega_{out}) \frac{\sin\theta}{\sin(\alpha-\theta)}}. \end{aligned} \quad (4.15)$$

This relation is identical with the published equations related to inverse partial fluorescence yield to obtain an bulk sensitive absorption spectra^[229]. The key aspect of inverse partial fluorescence yield is that one applies the partial fluorescence yield away from the target edges, the multiplication of $\mu_X(\omega_{in})$ and $S_X(\omega_{in}, \omega_{out})$

is a constant. For example, in a two element case, where cobalt and oxygen are considered. The emission intensity becomes:

$$I_{ems} = I_0 \frac{S_{Co}(\omega_{in}, \omega_{out})\mu_{Co}(\omega_{in}) + S_O(\omega_{in}, \omega_{out})\mu_O(\omega_{in})}{\mu_{Co}(\omega_{in}) + \mu_O(\omega_{in}) + (\mu_{Co}(\omega_{out}) + \mu_O(\omega_{out})) \frac{\sin\theta}{\sin(\alpha-\theta)}} \quad (4.16)$$

When accumulating the emitted photons at the oxygen K edge, the emission intensity of cobalt is negligible ($\mu_{Co}(\omega_{in})S_{Co}(\omega_{in}, \omega_{out}) \sim 0$). The emission spectrum becomes the summation of the emitted photon energy (ω_{out}) in the oxygen K edge, which leads $\mu_O(\omega_{in})S_O(\omega_{in}, \omega_{out})$ to be approximated constant with respect to the incident energy of the cobalt L edge. It also implies that the absorption factors of the emission photon ($\mu_{Co}(\omega_{out})$ and $\mu_O(\omega_{out})$) are approximately constant. Then the emission intensity at a fixed geometry can be simplified as:

$$I_{ems} = I_0 \frac{Constant}{\mu_{Co}(\omega_{in}) + \mu_O(\omega_{in}) + Constant} \quad (4.17)$$

The inverse intensity becomes that $I_{ems}^{-1} \propto \mu_{Co}(\omega_{in}) + \mu_O(\omega_{in}) + C$, where C and $\mu_O(\omega_{in})$ are constant with respect to the incident energy of the cobalt L edge. Thus the emission intensity is mainly dominated by the absorption factor $\mu_{Co}(\omega_{in})$ which provides a bulk sensitive absorption spectra.

For RIXS, equation 4.15 shows that the scattering intensity of RIXS should be corrected by the coefficient $\frac{1}{\mu(\omega_{in}) + \mu(\omega_{out}) \frac{\sin\theta}{\sin(\alpha-\theta)}}$ when the saturation effect is included. Figure 4.2b plots this saturation relation as the function of θ . The $\mu(\omega_{in})$ here is fixed at one and the $\mu(\omega_{out})$ is scaled from zero to infinity to simulate the trends. The scattering angle α is 140° . Note that no background contribution is considered in Fig. 4.2b. Depending on the competition between $\mu(\omega_{in})$ and $\mu(\omega_{out})$, three cases can be noticed:

i) $\mu(\omega_{out}) \gg \mu(\omega_{in})$ ($I_{ems} \simeq 0$). In this condition, the absorption factor of the emission beam is much bigger than incident beam absorption. The scattered photons can easier be reabsorbed in the emission process. It implies that the emission intensity tends to zero, see the lines of $\mu(\omega_{out}) \sim 100$.

ii) $\mu(\omega_{out}) \ll \mu(\omega_{in})$ ($I_{ems} \sim I_0 \frac{S_X(\omega_{in}, \omega_{out})\mu_X(\omega_{in})}{\mu(\omega_{in})}$). When the absorption factor of the emission beam is much smaller than the incident beam, the angular dependent term is negligible together with the small $\mu(\omega_{out})$ value. In other words, the spectrum saturation is angular independent, see the lines of $\mu(\omega_{out}) \sim 0$.

iii) $\mu(\omega_{out}) \simeq \mu(\omega_{in})$. In this case no factor can be omitted, see the lines of $\mu(\omega_{out}) \sim 1$. The self-absorption effect is dependant on the geometry and the photon energy of both incident and emitted beams. From the equation, we can specify

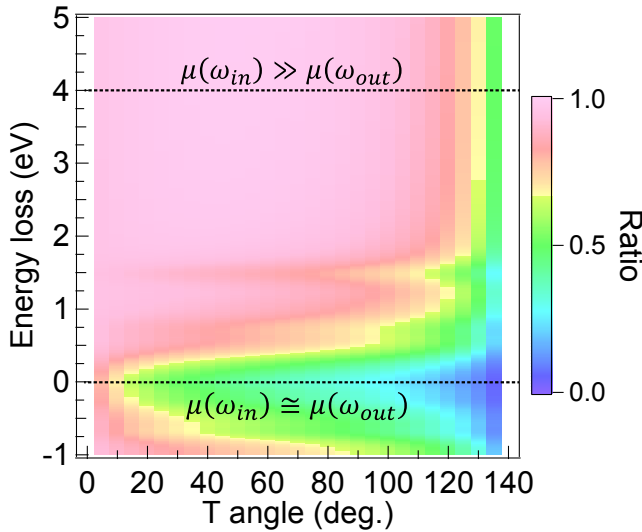


Figure 4.3: The correction coefficients ($\frac{1}{\mu(\omega_{in}) + \mu(\omega_{out})} \frac{\sin\theta}{\sin(\alpha - \theta)}$) as a function of rotation angle and emitted photon energy for the case of the LS $\text{Co}^{3+} {}^1\text{A}_{1g}(\text{O}_h)$ ground state. The incident energy is selected at maximum of L_3 edge.

the following two extreme conditions: The first case is that the incident beam is propagating along in the sample surface plane, where $\theta \sim 0$. Here, the emission intensity $I_{ems} \sim I_0 \frac{S_X(\omega_{in}, \omega_{out}) \mu_X(\omega_{in})}{\mu(\omega_{in})}$ provides a maximum value. But the absorption cross-section is saturated due to the competition between the absorption factor on certain element $\mu_X(\omega_{in})$ and the total absorption factor $\mu(\omega_{in})$. Another case describes that the propagation of the emitted beam is along in the sample surface plane. It implies that the scattered photons are totally reabsorbed and no scattering intensity should be expected ($I_{ems} \sim 0$).

In the case of the LS $\text{Co}^{3+} {}^1\text{A}_{1g}(\text{O}_h)$ ground state we obtain the $\mu(\omega_{out})$ and $\mu(\omega_{in})$ by calculating the XAS spectra. Because linear polarized beam is used, the value of $\mu(\omega_{in})$ is about half of the maximum of the total $\mu(\omega)$. Fixed incident photon energy implies that the incident absorption factor $\mu(\omega_{in})$ is always the same. In contrast, the $\mu(\omega_{out})$ is approximately equal to the total $\mu(\omega)$. Note that the total $\mu(\omega)$ includes not only the contribution of the target element and but also the contributions from other elements. We assume the other absorption channels give a background μ_B about 5% of total $\mu(\omega)$. Figure 4.3 shows the correction coefficients ($\frac{1}{\mu(\omega_{in}) + \mu(\omega_{out})} \frac{\sin\theta}{\sin(\alpha - \theta)}$) as a function of rotation angle and emitted photon energy. The emitted signal can be classified into two parts: the dd

excitations and the fluorescence. The emitted photons' energies of dd excitations are close to the L_3 edge absorption, which implies that $\mu(\omega_{out}^{dd}) \sim \mu(\omega_{in})$, so the case (iii) is applied. In contrast, the fluorescence feature is ~ 4 eV higher than elastic peak in L_3 RIXS, i.e., the emitted photons' energies ω_{out}^F is 4 eV smaller than the main line of L_3 edge. According to the calculation, the absorption factor 4 eV before the edge is considerable smaller. We can assume that $\mu(\omega_{out}^F) \ll \mu(\omega_{in})$ which leads to the case (ii) and shows no angular dependence. It also show that normalizing the spectra to the fluorescence feature is a safe way to reduce the experimental fluctuation in the current case.

4.3 Method

The Co $2p3d$ RIXS measurements were performed at the beamline 05A in Taiwan Light Source (TLS)^[24]. The scattering angle α was set at 140° for the LaCoO_3 single crystal and at 90° for the $\text{LaCoO}_3/\text{SrTiO}_3$ film. During the measurements of the crystal and the films, the (001) and (010) orientations of the samples were placed in the scattering plane. The sample details see the appendix and also the chapter 3. Both samples were measured at 20 K and at the Co L_3 edge ($\sim 780\text{eV}$). The experimental resolution of RIXS was calibrated as ~ 90 meV and the recorded incident energy broadening was about 1 eV fwhm. The calculations of the electronic structures and of $2p3d$ RIXS spectra were performed by the program Quanta in a tetragonal crystal field including the LMCT effect^[175, 202]. The intrinsic life time broadening of incident and emitted energies were considered by the widths 300 meV and 20 meV in fwhm, respectively. In addition to the intrinsic life time broadening, we applied 1000 meV and 60 meV Gaussian broadening to simulate the experiment incident energy window and the energy loss resolution.

4.4 Results and Discussion

Figure 4.4a shows the angular dependent RIXS of the LaCoO_3 single crystal at the maximum of Co L_3 edge. The experimental results were normalized and subtracted to the fluorescence feature, see appendix for a treatment example. The elastic peak shows a maximum intensity at the specular point ($\theta = \frac{\alpha}{2}$) due to strong reflection. In contrast, the intensity of the dd excitations decreases when the θ increases. Figure 4.4b shows the θ dependent calculation result of the $^1A_{1g}(O_h)$ ground state, where the angular dependence can be observed. Comparing the spectra of $\theta = 25^\circ$ and 70° , the excitation intensity of the $^3T_{1g}(O_h)$ feature slightly increase and the feature shifts due to the intensity competition of four

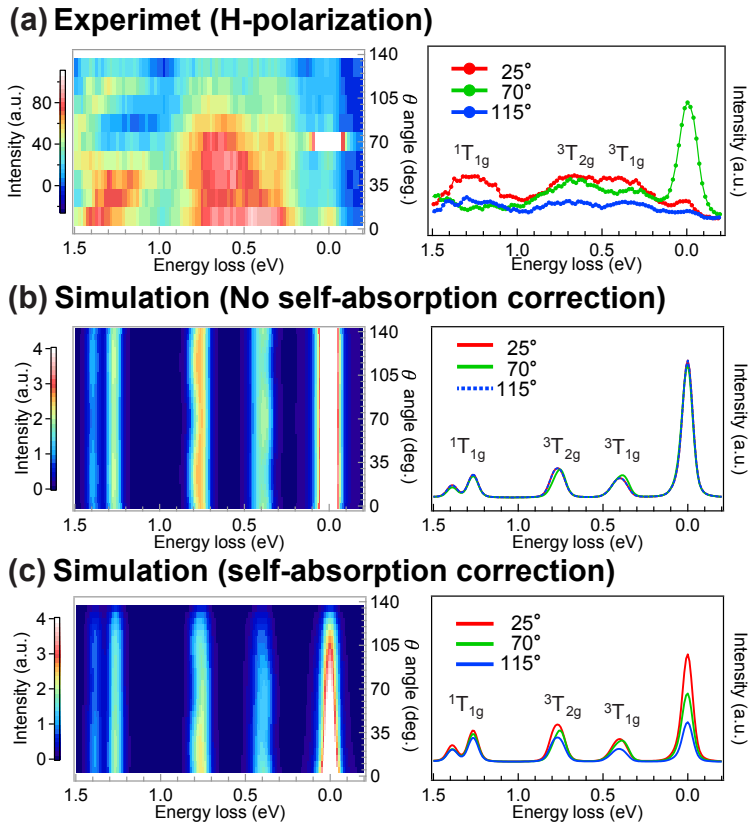


Figure 4.4: The $2p3d$ RIXS results as a function of rotation angle θ (left panels) and slice cuts (right panels). (a) The experimental results of LaCoO_3 . (b)-(c) The simulated spectra of ${}^1A_{1g}(O_h)$ ground state (b) without and (c) with including the saturation and self-absorption effect. The scattering geometry of calculation is identical to the angle used in the experiment on the LaCoO_3 single crystal ($\alpha = 140^\circ$; H-polarized incident photon).

spin-orbit fine structures, which will be discussed in next paragraph. However, the total trend is not in agreement with the experimental results because the saturation and self-absorption effects should be applied in a condensed sample. Figure 4.4c shows the simulations by multiplying the correcting ratios in Fig. 4.3 to the calculated result (Fig. 4.4b). This corrected results show good agreement in the trend except for the elastic peak. The intensity of the elastic peak is overestimated in the calculation. We conclude that, although the spectra were distorted, it still preserves the angular dependence of the fine structures. This angular dependence

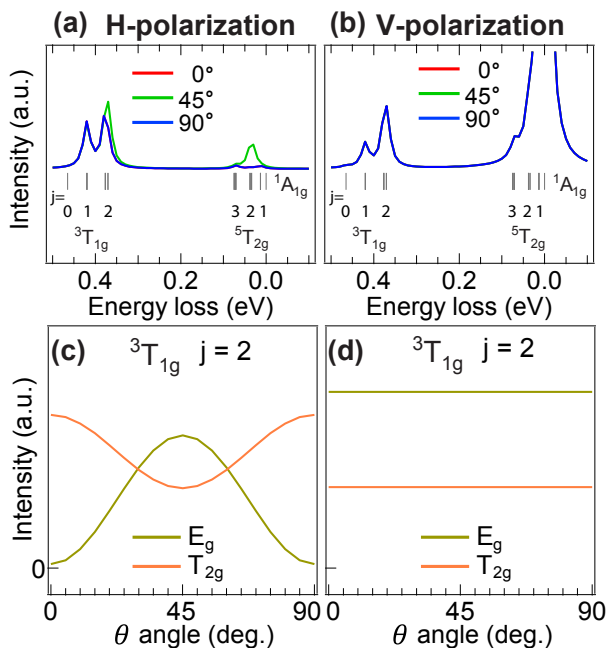


Figure 4.5: (a)-(b) The simulated $2p3d$ RIXS spectra of $^1A_{1g}(O_h)$ ground state as a function of sample rotation θ with small life time broadening. (c)-(d) The $2p3d$ RIXS transition cross-section of the $^3T_{1g}$ excitation state as function of rotation angle θ . Presenting here only the states with a total moment is equal to two ($j=2$). The scattering angle α is now replaced by 90° .

reflects the small energy shift of the $^3T_{1g}$ excitation state in both the experimental and the simulated results.

Generally, an isotropic symmetry (e.g. $^1A_{1g}$) shows no angular dependence in a dipole $2p3d$ transition. However, $2p3d$ RIXS has two dipole transitions (rank 1 transition), which implies that the final effective transition can have quadruple-like behavior (rank 2 transition), where the intermediate state of RIXS plays an important role to determine the cross-section^[32, 233]. The intermediate state is the maximum of the L_3 edge which is a mixture of different symmetries. On the other hand, due to the spin-orbit coupling, the final excited state splits into different branches with a small energy difference. In combination with the polarization tensor, the effective transition gives the angular dependence determined by the spin and orbit characteristics of the states for the case of $^1A_{1g}$ ground state. For example, figure 4.5a,b show three $2p3d$ RIXS spectra in different geometries. The scattering angle α is now replaced by 90° . The $^3T_{1g}$ state splits into four

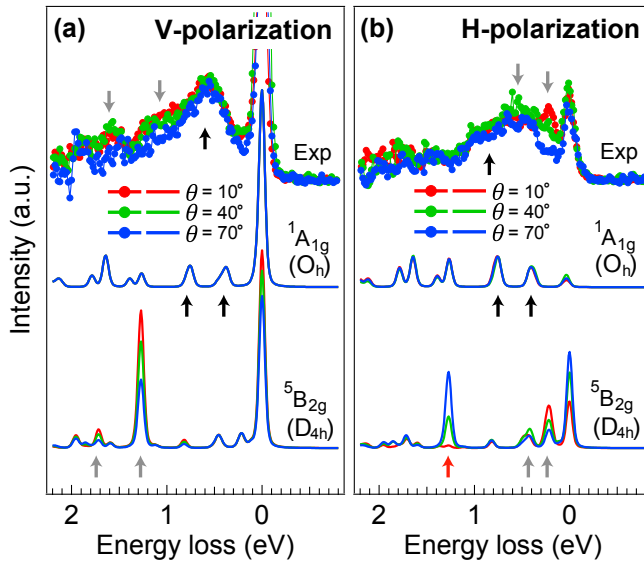


Figure 4.6: The $2p3d$ RIXS results of the 55nm $\text{LaCoO}_3/\text{SrTiO}_3$ film in comparing with the calculation of ${}^1A_{1g}(\text{O}_h)$ and ${}^5B_{2g}(\text{D}_{4h})$ ground states. Both the (a) V- and (b) H- polarized are calculated and measured at a geometry that scattering angle α is 90° .

states with E_g , T_{2g} , T_{1g} , and A_{1g} symmetry. For the V-polarization case, the elements in the polarization tensor are equally contributed in all geometries. Thus, no angular dependence is expected. In contrast, the H-polarized incident beam can have the non-homogeneous element in the polarization tensor as a function of system geometry. Thus, the angular dependence is pronounced and depending on the spin and orbit characteristics of the initial and the final state. Figure 4.5c,d present only the angular dependent RIXS cross-section of the E_g and T_{2g} group of the ${}^3T_{1g}$ state, which are probed at the maximum of L_3 edge. In Fig. 4.4, the broadening is increased due to the limiting experimental resolution. Hence the angular dependence reflects on the intensity competition and the energy shift.

One way to avoid the self-absorption effect is reducing the sample thickness. Then the saturation effect is only considered as a function of rotation angle (cf. Eq. 4.13). Once we normalize the spectra to the fluorescence features, the intensity of the dd excitations can be corrected properly. We examine this via the angular dependent $2p3d$ RIXS of the 55 nm $\text{LaCoO}_3/\text{SrTiO}_3$ film. Indeed, the dd excitations are now less influenced by the self-absorption effect and are mainly determined by the polarization selectivity, see Fig. 4.6. Most of the angular de-

pendent features agree with the calculation of the ${}^5B_{2g}(D_{4h})$ state (gray arrows). As discussed in chapter 3, the ground state of Co^{3+} ions in the $LaCoO_3/SrTiO_3$ film shows a mixture of LS ${}^1A_{1g}(O_h)$ state and HS ${}^5B_{2g}(D_{4h})$ state. Comparing to the ${}^5B_{2g}(D_{4h})$ state, the angular dependence of RIXS is negligible for the ${}^1A_{1g}(O_h)$ state (Fig. 4.6). It provides the angular independent features with respect to ${}^5B_{2g}(D_{4h})$ ground state as indicated in black arrows which are almost invisible. Some discrepancies are remained, for example, the 1.3 eV feature as indicated with the red arrow. It could be due to that we assumed that the CoO_6 clusters are well aligned to the pseudo-cubic orientation (002). Experimentally, not all the CoO_6 clusters should be aligned exactly along the pseudo-cubic orientation. Another possibility could be that the trigonal symmetry reduction was not taken into account. The angular dependent spectra are even more sensitive to distinguish the symmetry type than only using the polarization difference.

4.5 Conclusions

We have shown that the angular dependence of $2p3d$ RIXS analyzed with the scattering cross-section and the saturation/self-absorption effect. The ground state symmetry provides different orbital characteristics of the $2p3d$ RIXS transition and implies the different angular dependence on RIXS spectra. A remarkable consequence is that the isotropic LS ${}^1A_{1g}(O_h)$ ground state shows angular dependent $2p3d$ RIXS spectra, in contrast to the absence of angular dependence in the $2p$ XAS spectra. Unfortunately, the high Co concentration in the $LaCoO_3$ single crystal distorts the RIXS spectra due to the saturation effect which limits the distinguishability. By applying a self-absorption model, both the energy and angular trends of the saturation effect is well explained. In contrast, for the $LaCoO_3/SrTiO_3$ film, the self-absorption effect is small. Thus the $LaCoO_3/SrTiO_3$ film shows good agreement with the angular trend although some features are not reproduced well. The possible reason of this mismatch could be a mixture of ground states, non-perfect empirical parameters and/or reduced symmetry. Our results show that the angular dependent $2p3d$ RIXS can provide deeper understanding on the fundamental properties of strongly correlated oxide materials.

Appendix:Lattice information of single crystal

Figure 4.7a is an optical image showing the orientation of the LaCoO_3 single crystal. The unit vectors \vec{a} , \vec{b} , and \vec{c} correspond to the axes along the (100), (010), and (001) directions, respectively. The characterization of the crystal was carried out using an in-house X-ray 4-circle diffractometer, which scans the crystal along any crystallographic axes. The normal direction of the sample (cleavage plane) corresponds to the (012) direction in the $R\bar{3}C$ space group. To simplify the description, we use a pseudo-cubic lattice notation, e.g., the surface normal (012) is replaced by (001). Figure 4.7b-d show the diffraction patterns obtained by the Cu $K_{\alpha 1,2}$ emission. A θ - 2θ scan along the surface normal (001) shows the

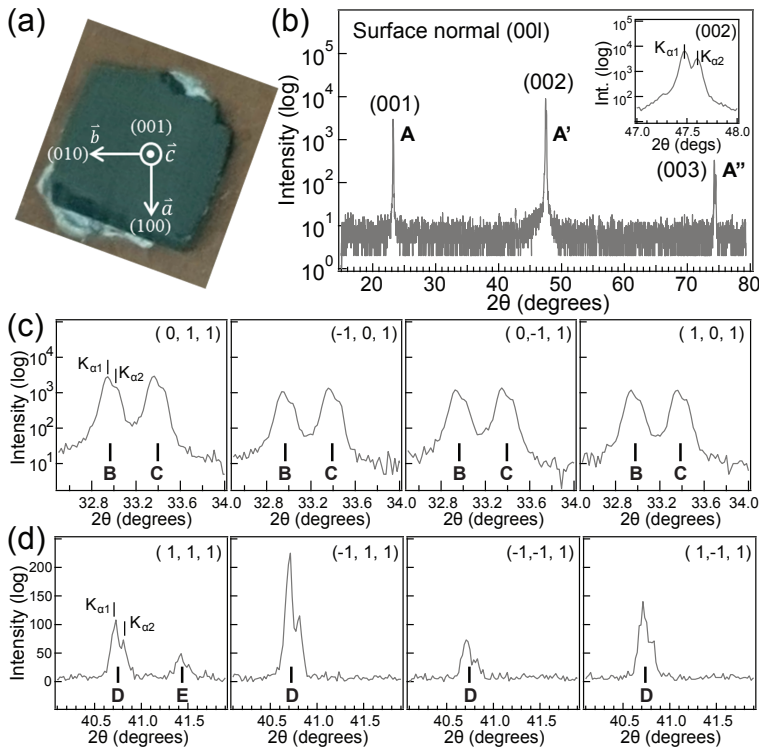


Figure 4.7: (a) The orientation of the LaCoO_3 sample. (b)-(d) The θ - 2θ diffractions along (b) surface normal (001), (c) off-normal (011), and (d) off-normal (111) direction. The inset of (b) shows the intensities with the scattering angle from 47° to 48° , in which a small multiplet splitting between Cu $K_{\alpha 1}$ and $K_{\alpha 2}$ is observed. The splittings are also found in the panels (c) and (d).

first to third harmonics of the reflection, as indicated by labels A, A', and A'' in Fig. 4.7b. We note that no “twins feature” was observed along the surface normal. The diffraction of the (011) direction is composed of the (110) and (104) features (B and C in Fig. 4.7c, respectively) in the notation of the $R\bar{3}C$ space group. Similarly, the diffraction of the (111) direction is composed of the (202) and (006) features (D and E in Fig. 4.7d, respectively) in the $R\bar{3}C$ notation. The (single) peak E confirms a single-domain crystal. The RIXS experiments were performed in the (010)-(001) scattering plane (Fig. 4.7a).

Appendix:Treatments on RIXS spectra

The spectral treatments were mentioned also in chapter 3. The RIXS spectra were measured for a fixed incident photon energy at the peak of the Co L_3 edge, see the inset of Fig. 4.8a. The experiential RIXS spectra are usually contaminated by fluorescence features, to which, e.g., the ion concentration, exposure area of the sample, and the probing path contribute in a complex way. One could assume, however, that the fluorescence feature has no intrinsic angular dependence and the self-absorption is homogeneous for the isotropic $^1A_{1g}(O_h)$ ground state. Thus, to extract excitations of the system in a safe way, the spectra with different q values are normalized to their fluorescence feature and then it is subtracted by a fitting procedure.

Figures 4.8a,b represent our data treatment of the RIXS spectrum. We select the spectrum which was measured at $q = (0.52\pi, 0.52\pi, 0.52\pi)$ with the H-polarization ($\alpha = 140^\circ, \theta \sim 15^\circ$). The gray area in Fig. 4.8a indicates the profile of the fluorescence feature, which is simulated by five Gaussian functions. We note that, actually, the normalization area of fluorescence affect the total intensity a bit. Furthermore, the fluorescence profile is not exactly identical from one to another due to the incident energy fluctuation. Then the fluorescence profile is subtracted from the experimental data, leading to a blue curve in Fig. 4.8a, where the dd excitations are clearly visible, see also Fig. 4.8b. These dd excitations (with energies below 2.0 eV) can be fitted by Gaussian functions with 250 meV (fwhm), simulating the instrumental resolution ($\Delta E = 90$ meV), the spin-orbit coupling effect (~ 50 meV), and possible vibrational effect^[234]. Five distinguishable dd excitations were selected and they correspond to the $^1A_{1g}$, $^3T_{1g}$, $^3T_{2g}$, $^1T_{1g}$, and 5E_g states in an octahedral symmetry, indicated in Fig. 4.8b. The HS $^5T_{2g}(O_h)$ state was omitted in the fitting procedure because of its negligible intensity in the L -edge RIXS spectra. The elastic peak is fitted by a Gaussian (90 meV) and a pseudo-Voigt function (~ 200 meV) that simulates an additional tail due to an

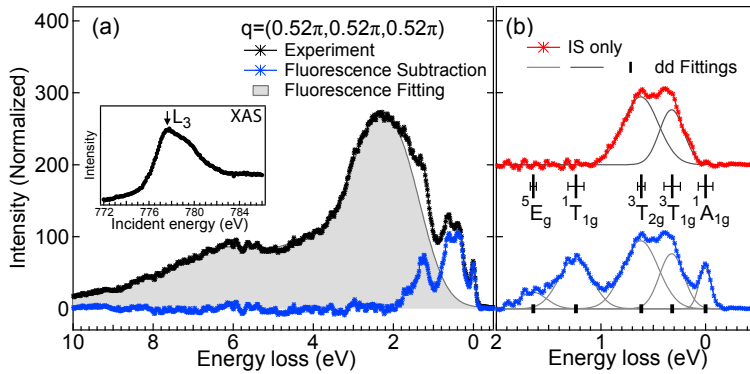


Figure 4.8: (a) Fluorescence profile and fluorescence-subtracted data for the RIXS spectrum at $\mathbf{q} = (0.52\pi, 0.52\pi, 0.52\pi)$ with the H-polarization. The inset shows the L_3 -edge absorption spectra, in which the arrow indicates the resonance energy used in the RIXS measurement. (b) The Gaussian fitting of the dd excitations (below 2.0 eV). The black bars mark the peak position of the Gaussian functions (gray curves). The red curve shows the contributions of the IS excitations.

aberration of the gratings. We note that the weight of the pseudo-Voigt function is less than 5% of that of the Gaussian, see Fig. 4.8c. The 90 meV broadening of elastic peak is consistent with the experimental resolution because there is no spin-orbit splitting.

Chapter 5

Excitonic Dispersion of the Intermediate-Spin State in LaCoO_3

Traditionally, the spin-state crossover of LaCoO_3 has been described as a thermal population of excited atomic multiplets. Despite its long history, the opinion on the nature of the first excited Co^{3+} multiplet remains split between the high-spin (HS, $S = 2$, $t_{2g}^4 e_g^2$) and intermediate-spin (IS, $S = 1$, $t_{2g}^5 e_g^1$) states^[80]. A co-existence of Co ions in the excited (IS or HS) and ground (LS) states in a lattice is expected to cause a sizable disproportionation of Co-O bond lengths. However, this has never been observed despite the effort to do so. Here, I report Co L_3 -edge resonant inelastic X-ray scattering on LaCoO_3 at 20 K and observe excitations with sizable dispersion that I identify as intermediate-spin (IS) states of ${}^3T_{1g}$ symmetry. The present result shows that mobility substantially reduces the energy of IS excitations in part of the Brillouin zone, which makes them important players in the low-energy physics of LaCoO_3 together with immobile high-spin (HS) excitations.

This chapter is based on the publication:

R.-P. Wang, A. Hariki, A. Sotnikov, *et al.*, “Excitonic dispersion of the intermediate spin state in LaCoO_3 revealed by resonant inelastic x-ray scattering”, **Phys. Rev. B** **98**, 035149 (2018)

5.1 Introduction

More than 50 years ago the electron-hole attraction was proposed to drive narrow gap semiconductors or semimetals to a new phase, the excitonic insulator. The experimental proof of its existence in bulk materials remains elusive. In strongly correlated insulators, the proximity of the excitonic insulator phase is reflected by the presence of dispersive electron-hole excitations with a small gap above a singlet ground state^[235]. Recently, such an excitation spectrum was proposed to be realized in perovskite oxide LaCoO_3 ^[113].

At low temperature LaCoO_3 is a non-magnetic insulator with Co ions in the low-spin (LS, $S = 0$, $t_{2g}^6 e_g^0$) ground state. Upon heating it undergoes a crossover to a paramagnetic Curie-Weiss insulator ($T \sim 100$ K) and, eventually, a Curie-Weiss metal ($T \sim 500$ K)^[64–66, 68, 79, 82, 97]. Traditionally, the spin-state crossover has been described as a thermal population of excited atomic multiplets. Despite its long history, the opinion on the nature of the first excited Co^{3+} multiplet remains split between the high-spin (HS, $S = 2$, $t_{2g}^4 e_g^2$)^[30, 74, 97] and intermediate-spin (IS, $S = 1$, $t_{2g}^5 e_g^1$)^[80] states. Both scenarios are allegedly supported by experiments, see, e.g., Refs. [87, 96, 97] and [84, 86, 88–90] for the former and latter one, respectively. A coexistence of Co ions in the excited (IS or HS) and ground (LS) states in a lattice is expected to cause a sizable disproportionation of Co-O bond lengths. However, this has never been observed despite the effort to do so.

The excitonic scenario is based on the observation that not only the spin but also the multiplet flavors (LS, IS, and HS) undergo nearest-neighbor (nn) exchange via the superexchange mechanism. Inter-atomic exchange processes such as $|\text{LS}, \text{IS}\rangle \leftrightarrow |\text{IS}, \text{LS}\rangle$, see Fig. 5.1a, $|\text{LS}, \text{HS}\rangle \leftrightarrow |\text{IS}, \text{IS}\rangle$, or $|\text{IS}, \text{HS}\rangle \leftrightarrow |\text{HS}, \text{IS}\rangle$ turn out to have sizable amplitudes on nn bonds. At low temperatures, where the state of the system is dominated by atomic LS states, only the first process is relevant. It gives rise to propagation of IS excitations (excitons) on the LS background. As usual in periodic systems, the elementary IS excitations have the plane-wave form with the energy dependent on the quasi-momentum \mathbf{q} , see Fig. 5.1b.

The IS excitons come in two orbital symmetries (irreducible representations): ${}^3T_{1g}$ ($d_{xy} \otimes d_{x^2-y^2}$, $d_{zx} \otimes d_{z^2-x^2}$, and $d_{yz} \otimes d_{y^2-z^2}$) and ${}^3T_{2g}$ ($d_{xy} \otimes d_{z^2}$, $d_{zx} \otimes d_{y^2}$, and $d_{yz} \otimes d_{x^2}$). Due to their geometry, the ${}^3T_{1g}$ excitons have lower on-site energies (stronger bonding) and larger mobility, concentrated to their respective planes. The HS excitations behave differently. The nn HS-LS exchange is a fourth-order process in hopping and thus has a substantially smaller amplitude than the second-order IS-LS exchange. The HS excitation can be approximately treated as an

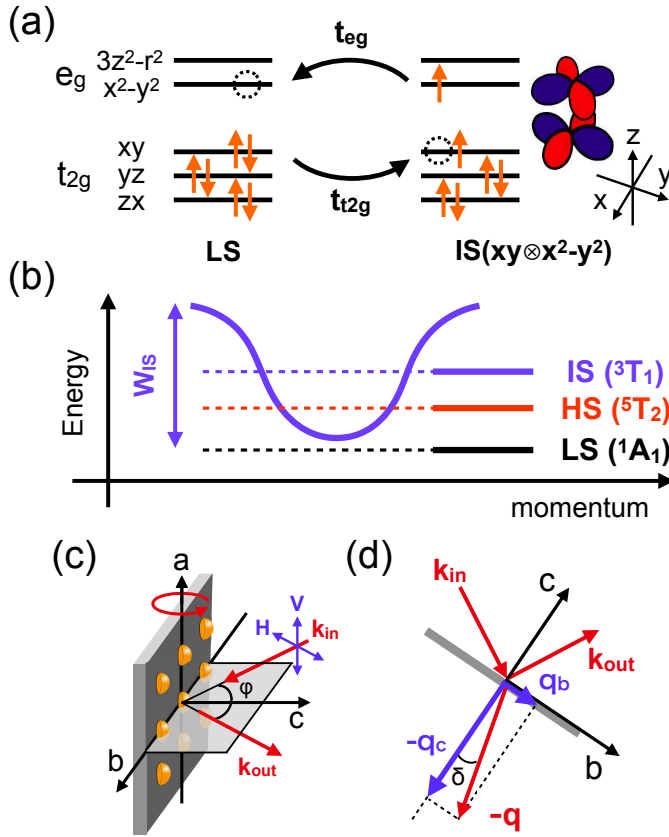


Figure 5.1: (a) A cartoon view of the nn hopping process with the dominant contribution to the IS propagation, and the orbital structure of the $^3T_{1g}$ excitation. (b) Sketch of the atomic-level energies together with the dispersion of the IS ($^3T_{1g}$) state on the LS background in the lattice. (c) The experimental geometry and the definition of the scattering angle φ , where $\varphi = 180^\circ - \alpha$. α has been defined in section 1.1.2. The sample can be rotated around the a axis. The half-spheres represent Co atoms. (d) Determination of the momentum transfer $\mathbf{q} = \mathbf{k}_{out} - \mathbf{k}_{in}$. The component q_b due to the offset δ is negligibly small ($|q_b| < 0.03\pi$).

immobile bound pair (bi-exciton) of two IS excitons with different orbital flavors.

The existence of dispersive low-energy excitations has profound consequences. Their thermal population does not lead to a static distribution of excited atomic states and thus does not induce lattice distortions. When the excitation gap is closed, e.g., by application of strong magnetic field^[112], the excitations with \mathbf{q} -vector of the band minimum form a condensate. Recent LDA+ U calculations^[236]

find LaCoO_3 to be close to the condensation instability. The metamagnetic transition observed in high fields^[112] has the temperature dependence consistent with exciton condensation, but not with HS-LS spin-state order^[113]. The properties of the low-temperature phase of related $(\text{Pr}_{1-y}\text{R}_y)_x\text{Ca}_{1-x}\text{CoO}_3$ have been consistently explained by exciton condensation^[237, 238]. Despite this indirect evidence an unambiguous proof of the excitonic physics in LaCoO_3 has been missing. Ultimately, this can be provided by direct observation of the IS dispersion.

5.2 Method

5.2.1 Experiment

RIXS has become a powerful tool to study low-energy excitations in transition metal oxides in the last decade^[11]. The Co L_3 -edge RIXS ($2p_{3/2} \rightarrow 3d \rightarrow 2p_{3/2}$) provides sufficient energy resolution to distinguish different spin states^[103]. The RIXS amplitude for the IS excitations is sufficient to enable observation of their dispersion, although the X-ray wave-length at the Co L_3 edge in LaCoO_3 ($\approx 15.9 \text{ \AA}$) restricts the accessible momentum transfer.

The LaCoO_3 single crystal was grown by the floating zone method^[103] and more sample details can be found in past two chapters. The RIXS measurements were performed at the BL05A in Taiwan Light Source (TLS), with linearly polarized X-rays, either vertical (V) or horizontal (H) to the scattering plane. The overall energy resolution at the Co L_3 edge ($\sim 780 \text{ eV}$) was 90 meV ^[24]. The experimental setup is illustrated in Figs. 5.1c and 5.1d. The sample normal was aligned to the \mathbf{c} axis in the (pseudo) cubic axis with a lattice constant $a_{\text{cub}} \approx 3.83 \text{ \AA}$. The measurements were carried out in the bc scattering plane by rotating the sample along the \mathbf{a} axis. We define the momentum transfer $\mathbf{q} = (0, q_b, q_c)/a_{\text{cub}}$ as the projection of the transferred momentum \mathbf{q} onto the \mathbf{b} and \mathbf{c} axes, and a_{cub} is omitted from now on, for simplicity. The scattering angles φ of 148° , 120° , 90° , and 40° correspond to $\mathbf{q} = (0, q_b, 0.26\pi)$, $(0, q_b, 0.48\pi)$, $(0, q_b, 0.68\pi)$ and $(0, q_b, 0.90\pi)$, respectively. We set a small offset δ to avoid a strong signal due to reflection, see Fig. 5.1(d). It implies a small q_b projection value ($|q_b| < 0.03\pi$), that is negligible with the present energy resolution. The sample temperature was 20 K , i.e., well below the spin-crossover temperature.

5.2.2 RIXS Calculation

The theoretical RIXS cross-section can be reformulated as^[20]:

$$\frac{\delta^2 \sigma}{\delta \Omega \delta \omega} \propto \text{Im} \sum_{\gamma, \gamma'} R_{\gamma'}^\dagger(\mathbf{q}, \omega_{\text{in}}) G_{\gamma', \gamma}(\mathbf{q}, \omega_{\text{loss}}) R_{\gamma}(\mathbf{q}, \omega_{\text{in}}). \quad (5.1)$$

$R_\gamma(\mathbf{q}, \omega_{\text{in}})$ is the X-ray absorption/emission amplitude and $G_{\gamma,\gamma}(\mathbf{q}, \omega_{\text{loss}})$ stands for the electron-hole propagator. While the former determines the intensity (visibility) of different multiplet excitations γ in the RIXS spectra, it is solely the latter one that determines their dispersions. Here ω_{in} is the incident photon energy and ω_{loss} is the energy transfer.

$R_\gamma(\mathbf{q}, \omega_{\text{in}})$ is given by $\langle d_\gamma(r_j) | V_E(\omega_{\text{in}} + E_{\text{LS}} - H + i\Gamma)^{-1} V_I | GS \rangle$. A sufficiently accurate estimation of this amplitudes is provided by the atomic-model calculation for Co^{3+} , which includes the experimental geometry encoded in the $V_I(V_E)$ operator of the incident (emitted) photon, full-multiplet form of $3d$ - $3d$ and $2p$ - $3d$ Coulomb interaction, the $3d$ crystal field and the spin-orbit coupling in the Co $3d$ shell and the $2p$ shell. The nature ground state $|GS\rangle$ of LaCoO_3 can be replaced by the LS state vacuum $|LS\rangle$ and the $|d_\gamma(r_j)\rangle$ describes the excited state of $2p^6 3d^n$ configuration. The spin-orbit coupling within the $2p$ shell ζ_p and the Slater integrals for the $2p$ - $3d$ interaction F^k, G^k are calculated within an atomic Hartree-Fock code. Then the F^k and G^k values for the $2p$ - $3d$ interaction are scaled down by the empirical factor 75% to simulate the effect of intra-atomic configuration interaction from higher basis configurations neglected in the atomic calculation. We note that the amplitude $R_\gamma(\mathbf{q}, \omega_{\text{in}})$ for the LS ground state is rather insensitive to the choice of the empirical factor.

The matrix element of the particle-hole propagator $G_{\gamma,\gamma}(\mathbf{q}, \omega_{\text{loss}})$ ($= \langle d_\gamma(\mathbf{q}) | (\omega_{\text{loss}} + E_{\text{LS}} - H + i\delta)^{-1} | d_\gamma(\mathbf{q}) \rangle$), which determines the dispersion of the excitations, is the key theoretical quantity studied in this work. Its evaluation is, in general, a difficult task that requires approximations. The insulating ground state of LaCoO_3 ^[239–241], which can be viewed as a collection of LS atoms allows us to eliminate the local charge fluctuations and to use a low-energy effective model where only a few atomic multiplets and their nearest-neighbor interactions are retained. The description is further simplified at the low-temperatures ($T \lesssim 20$ K) where thermal excitations can be neglected and generalized spin-wave theory can be used^[242], which describes the excitations as non-interacting bosons propagating on the lattice.

5.2.3 The Effective Bosonic Model in Co^{3+}

Construction of the model starts with the density-functional calculation for the idealized cubic perovskite structure ($a=3.8498$ Å) using Wien2k^[243]. Then, an effective Hubbard model spanning the Co $3d$ -like band is obtained with the wien2wannier^[244] and wannier90^[245] software. The starting point of our strong-coupling analysis is the Hubbard Hamiltonian for the d -shells of Co:

$$H = \sum_i H_{\text{at}}^{(i)} + \sum_{\mathbf{r}} H_t^{(\mathbf{r})}, \quad (5.2)$$

where

$$H_{\text{at}}^{(i)} = \sum_{\alpha\beta} t_{\alpha\beta}^{ii} c_{i\alpha}^\dagger c_{i\beta} + \sum_{\alpha\beta\gamma\delta} U_{\alpha\beta\gamma\delta} c_{i\alpha}^\dagger c_{i\beta}^\dagger c_{i\gamma} c_{i\delta}, \quad (5.3)$$

$$H_t^{(\mathbf{r})} \equiv H_t^{(ij)} = \sum_{\alpha\beta} t_{\alpha\beta}^{ij} c_{i\alpha}^\dagger c_{j\beta}, \quad i \neq j, \quad (5.4)$$

i and j are the lattice-site indices (we account for local, $i = j$, and nn contributions only) that correspond to a particular bond index \mathbf{r} for $i \neq j$, and $\alpha, \beta, \gamma, \delta$ are the internal state (orbital and spin) indices. The local and nn hopping matrices $t_{\alpha\beta}^{ij}$ are provided by projection of the band structure (obtained in the framework of the *ab initio* density-functional approach^[243] for the idealized cubic perovskite structure) to Wannier orbitals. In the absence of spin-orbit coupling, this approach yields the local matrix $t_{\alpha\beta}^{ii}$ with diagonal entries ($\alpha = \beta$) only, which are degenerate with respect to the t_{2g} or e_g orbital character.

In our optimized result, the cubic crystal field splitting (between the t_{2g} and e_g states) is $10Dq=1.666$ eV. The spin-orbit coupling has the amplitude $\zeta_d = 56$ meV and adds corresponding off-diagonal elements to the local matrix $t_{\alpha\beta}^{ii}$. The nn hopping matrices are equal for the spin-up and spin-down sectors (z is the spin quantization axis), which have almost diagonal structure in the orbital space (the order $z^2, x^2 - y^2, xy, yz, zx$ is used below),

$$t^{(\hat{x})} = \begin{pmatrix} -0.147 & 0.269 & & & \\ & 0.269 & -0.458 & & \\ & & & -0.159 & \\ & & & & -0.071 \\ & & & & & -0.159 \end{pmatrix},$$

$$t^{(\hat{y})} = \begin{pmatrix} -0.147 & -0.269 & & & \\ -0.269 & -0.458 & & & \\ & & & -0.159 & \\ & & & & -0.159 \\ & & & & & -0.071 \end{pmatrix},$$

and $t^{(\hat{z})} = \text{diag}(-0.614, -0.008, -0.071, -0.159, -0.159)$ with the values given in units of eV. For the interaction term, we use the Slater parametrization of the intra-atomic electron-electron interaction $U_{\alpha\beta\gamma\delta}$ with two tunable parameters, average interaction U and Hund's coupling J , while fixing the ratio of Slater integrals

$F_{\text{dd}}^4/F_{\text{dd}}^2 = 0.625$. These two interaction parameters U and J are adjusted to yield the proper position of the many-body states in accordance with recent experimental observations. This results, in particular, in the choice of $U = F_{\text{dd}}^0 = 2.1$ eV and $J = 0.66$ eV that yields $F_{\text{dd}}^2 = 5.686$ eV.

We diagonalize the local Hamiltonian $H_{\text{at}}^{(i)}$ to obtain atomic eigenenergies $E_{\gamma}^{(q)}$ and eigenstates $|\Psi_{\gamma}^{(q)}\rangle$, where q is the number of electrons in the d -shell ($q = 6$ for Co^{3+} ions in LaCoO_3) and γ is the state index. Next, we use the set of the lowest 34 states of the d^6 configuration containing LS, HS, IS (T_{1g} and T_{2g}) as an active space and treat the non-local terms $H_t^{(r)}$ as a perturbation. Performing the Schrieffer–Wolff transformation^[246] to the second order, we arrive at the following bosonic Hamiltonian:

$$H_{\text{eff}} = H_0 + H_{\text{int}}, \quad H_0 = \sum_{ij, \gamma\gamma'} (h_{\gamma\gamma'}^{ij} d_{i\gamma}^{\dagger} d_{j\gamma'} s_i s_j^{\dagger} + \Delta_{\gamma\gamma'}^{ij} d_{i\gamma}^{\dagger} d_{j\gamma'}^{\dagger} s_i s_j + \text{H.c.}). \quad (5.5)$$

State	E_{at}	$a_{\gamma\gamma}^{(\hat{x})}$	$a_{\gamma\gamma}^{(\hat{y})}$	$a_{\gamma\gamma}^{(\hat{z})}$
LS	0.000	-0.003	-0.003	-0.003
HS($xy \otimes yz$)	0.879	-0.148	-0.137	-0.148
IS (T_{1g}, xy)	0.879	-0.136	-0.136	-0.006
IS (T_{2g}, xy)	1.324	-0.078	-0.078	-0.210
State	$h_{\gamma\gamma}^{ii}$	$h_{\gamma\gamma}^{ij(\hat{x})}$	$h_{\gamma\gamma}^{ij(\hat{y})}$	$h_{\gamma\gamma}^{ij(\hat{z})}$
LS	0.000	—	—	—
HS($xy \otimes yz$)	0.034	0.000	0.000	0.000
IS (T_{1g}, xy)	0.344	0.062	0.062	0.001
IS (T_{2g}, xy)	0.613	0.024	0.024	0.044
State	$\Delta_{\gamma\gamma}^{ij(\hat{x})}$	$\Delta_{\gamma\gamma}^{ij(\hat{y})}$	$\Delta_{\gamma\gamma}^{ij(\hat{z})}$	
LS	—	—	—	
HS($xy \otimes yz$)	0.000	0.000	0.000	
IS (T_{1g}, xy)	0.003	0.003	0.000	
IS (T_{2g}, xy)	0.001	0.001	0.003	

Table 5.1: Characteristic bosonic amplitudes (in units of eV) of the effective model at $U = 2.1$ eV, $J = 0.66$ eV, and $\zeta_d = 0$. The amplitudes for pair creation/annihilation processes are not general and shown for $S_z = 0$ states only, due to their dependence on the spin projection (the process obeys its conservation rule, i.e., only IS pairs with opposite m_s contribute).

Here, we consider the LS state (more precisely, it is not “pure” LS because of local spin-orbit coupling contributions from other states) as the bosonic vacuum that $|\emptyset\rangle_i = s_i^\dagger |0\rangle$, and other states from the low-energy manifold of the d^6 configuration as different bosonic flavors γ characterized by the corresponding creation (annihilation) operators $d_{i\gamma}^\dagger$ ($d_{i\gamma}$) on the lattice site i . The term with the amplitude h in Eq. 5.5 corresponds to the *renormalized* on-site energies of bosons (for $i = j$), and their hopping amplitudes on the LS background (for $i \neq j$). The term with the amplitude Δ describes the non-local pair-creation/annihilation processes. The interaction term H_{int} in Eq. 5.5 contains third and fourth order terms in d (d^\dagger). The explicit expressions for the effective bosonic amplitudes h and Δ in terms of original fermionic parameters can be found in Ref. [247].

In Table 5.1, for sake of visibility, we provide only few characteristic values for the amplitudes and both atomic E_{at} and renormalized $h_{\gamma\gamma}^{ii}$ energies, $h_{\gamma\gamma}^{ii} = E_{\text{at},\gamma} + \sum_{\mathbf{r}} [a_{\gamma\gamma}^{(\mathbf{r})} - a_{\emptyset\emptyset}^{(\mathbf{r})}]$, in the absence of spin-orbit coupling. Note that values for states with other orbital characters can be obtained by corresponding permutations of basis vectors. Due to its non-negligible amplitude of spin-orbit coupling (we estimate it as $\zeta_d = 56$ meV), it affects the listed values of physical quantities of interest and thus the dispersive features. Its presence is accounted for in the numerical procedure (resulting in the dispersions shown in the main part of the manuscript), but makes the matrices h and Δ dense hindering a simple summary of characteristic values similar to those that are shown in Table 5.1. Restricting ourselves to the zero density of d -excitations (i.e., neglecting the boson-boson interaction term H_{int}), we proceed with the linearized spin-wave approach^[242]. This provides access not only to momentum dependencies of bosonic (IS and HS) excitations in the lattice, but also allows us to analyze theoretically all the relevant RIXS intensities in LaCoO_3 , as discussed above.

5.3 Results and Discussion

Figure 5.2 shows experimental RIXS spectra along the path in reciprocal space from $\Gamma(0, 0, 0)$ to $X(0, 0, \pi)$ recorded at 20 K, well below the spin-crossover temperature. The spectra were normalized to the fluorescence that was subsequently subtracted as it has been done in past chapters. The inset shows the spectrum at $q=(0, 0, 0.90\pi)$ in a wide energy window. It can be decomposed into five Gaussian contributions with the full width at half maximum (fwhm) of 250 meV, accounting for the instrumental resolution ($\Delta E = 90$ meV), the spin-orbit splitting of the multiplets, and possible vibrational effect^[234]. The four peaks at around 0.4, 0.7, 1.2, and 1.6 eV, are attributed to the excitations from LS ($^1A_{1g}$) ground state to IS

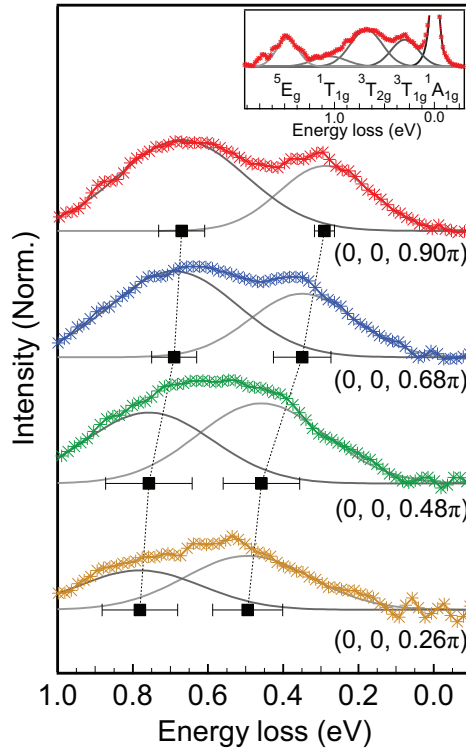


Figure 5.2: Experimental spectra for different momentum transfers $(0, 0, q_c)$. The elastic peak is subtracted and each spectrum is fitted by two Gaussian functions with 250 meV of fwhm, with centers indicated by squares with the error bar. The inset shows the spectrum at $\mathbf{q}=(0,0,0.90\pi)$ in a wide energy range together with the term symbols (see discussion in text).

$({}^3T_{1g})$, IS (${}^3T_{2g}$), LS (${}^1T_{1g}$), and HS (5E_g) states, respectively^[103]. We point out that the lowest HS (${}^5T_{2g}$) state, located below 100 meV^[97], has a negligible RIXS intensity in the LS ground state^[103, 248] and thus is not visible at low temperature. The IS ${}^3T_{1g}$ peak exhibits a clear \mathbf{q} -dependent shift from 490 to 290 meV in the interval from $\mathbf{q}=(0,0,0.26\pi)$ to $(0,0,0.90\pi)$. The \mathbf{q} -dependence of the IS ${}^3T_{2g}$ peak at around 0.7 eV is much less pronounced.

Figure 5.3 shows the theoretically calculated spectra of particle-hole excitations ρ_{ph} in LaCoO₃ for different U (row) and J (column) values, together with the present RIXS experimental data. For the parameters in the upper-right triangle (gray background) or at smaller U and J values, the LS state is not a stable ground state, contradicting the experimental observations at $T \lesssim 20$ K^[68, 82, 97]. The excitation energy of the lowest high-spin state (~ 10 – 20 meV) is in agree-

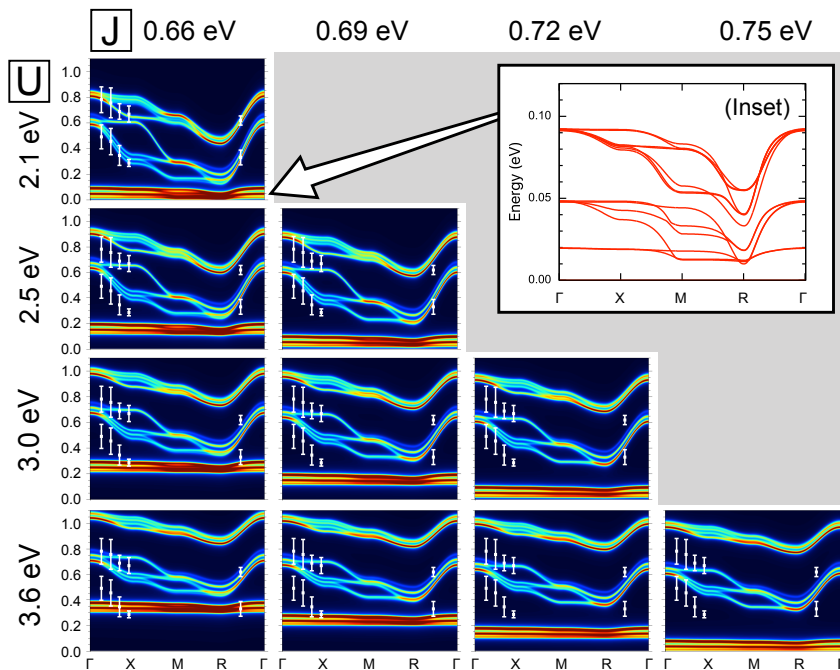


Figure 5.3: The calculated total densities of particle-hole excitations ρ_{ph} for different U (row) and J (column) values, together with the RIXS experimental data (white points with error bars) from Fig 2. The additional point $\mathbf{q}=(0.52\pi, 0.52\pi, 0.52\pi)$ was measured with H polarization. The inset shows the low-energy region for $(U, J) = (2.1 \text{ eV}, 0.66 \text{ eV})$.

ment with other studies^[87, 96, 103] only along the diagonal panels in Fig. 5.3. For $(U, J)=(2.1 \text{ eV}, 0.66 \text{ eV})$, the best agreement with the RIXS experimental data is found. The inset shows the low-energy region for the chosen regime. Note here that the calculated spectra are quite sensitive to the variation of U and J , which has a complex effect of changing simultaneously the positions of band centers and bandwidths of all excitations. Therefore the existence of parameters matching all experimental constraints is more than trivial fitting. When comparing with interaction parameters used in other studies one has to keep in mind that U and J are strongly basis dependent. Therefore the present values can be compared to studies based on $3d$ -only models^[249], but not to the values used in LDA+ U or models including the O $2p$ states explicitly. The optimized U and J values yield $F_{\text{dd}}^2 = 5.686 \text{ eV}$ in such $3d$ -only model, which rough agrees with the screened Slater integral value in the $3d$ -only cluster model ($F_{\text{dd}}^2 = 5.065 \text{ eV}$, see chapter 3).

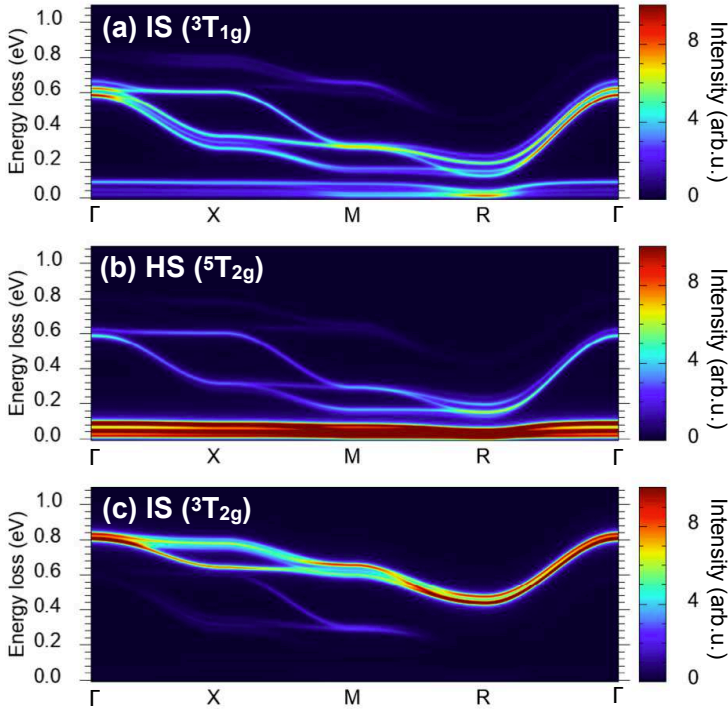


Figure 5.4: The calculated densities of particle-hole excitations resolved into contributions of different atomic multiplets: (a) IS (${}^3T_{1g}$), (b) HS (${}^5T_{2g}$) and (c) IS (${}^3T_{2g}$). The spectra were artificially broadened with a Lorentzian of 10 meV width. The interaction parameters $U=2.1$ eV and $J = 0.66$ eV, and the spin-orbit coupling amplitude $\zeta_d = 56$ meV were used in the effective Hubbard 'Co d -only' model.

Fig. 5.4 shows the contributions of different atomic multiplets to the calculated dispersion of elementary excitations. The sizable dispersion of the IS ${}^3T_{1g}$ branch, describing a propagation of a single IS ${}^3T_{1g}$ state on the LS background, originates from processes such as the one depicted in Fig. 5.1(a). The band minimum at the R point is a simple consequence of the electron nn hopping amplitudes t_{e_g} and $t_{t_{2g}}$ [see Fig. 5.1(a)] having the same sign ^[236], a general feature of the perovskite structure. The enhanced low-energy IS ${}^3T_{1g}$ intensity around the R point is partly due to weak nn pair creation/annihilation processes $|\text{LS}, \text{LS}\rangle \leftrightarrow |\text{IS}, \text{IS}\rangle$ ^[247]. The spin-orbit coupling induces a splitting in the IS ${}^3T_{1g}$ states, which is clearly seen along the R - Γ direction, see Fig. 5.4a and Fig. 5.5c.

The HS excitations, within the present approximation, have no hopping on the LS background. As a result, they form almost flat bands with the centers at

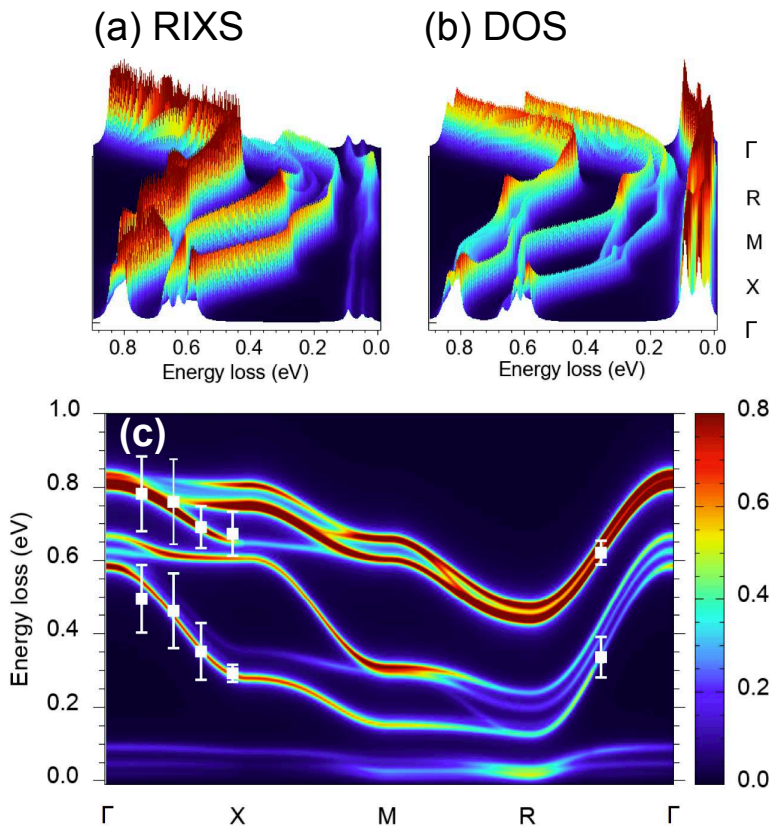


Figure 5.5: The calculated RIXS intensities (a,c) along the high-symmetry directions in the pseudo-cubic BZ compared with experimental data from Fig. 5.2. The IS (${}^3T_{1g}$) excitations show the dispersion feature from 10 to 600 meV. The ${}^3T_{2g}$ IS excitations are located at higher energies. The flat bands located below 100 meV correspond to the spin-orbit split HS multiplet. (b) 3D plot showing the calculated total density of the particle-hole excitations ρ_{ph} . Comparison to the RIXS spectra reveals the suppression of the HS intensity by the transition matrix elements.

approximately 20, 45 and 90 meV, split and partially mixed with IS by the spin-orbit coupling. These energies are consistent with other studies^[87, 96, 103].

Inclusion of the transition amplitudes $R_\gamma(\mathbf{q}, \omega_{in})$ strongly suppresses the contribution of the HS (${}^5T_{2g}$) states to the RIXS spectra, see Fig. 5.5(a) and 5.5(b). The calculated RIXS intensities along high-symmetry lines in the cubic Brillouin zone (BZ) together with the experimental ${}^3T_{1g}$ and ${}^3T_{2g}$ peak positions are shown in Fig. 5.5(c). We find a very good match in the experimentally accessible part of

BZ along the Γ - X and Γ - R directions. The most interesting region around R point is out of the experimental reach at Co L_3 -edge. Due to the dominant nn character of the exciton hopping, the shape of the dispersion is largely determined by the lattice structure. Knowing the dispersion over a substantial part of the bandwidth thus puts the extrapolation on a solid ground.

Without experimental data about the detailed excitation spectrum around the R point we can speculate about two possible scenarios: (i) the lowest excitation is dominantly IS, implying that exciton condensation would be possible upon closing of the excitation gap, e.g., by a magnetic field as discussed^[113] in some interval of small IS concentrations; (ii) the lowest excitation is dominantly HS, but the existence of mobile IS excitations prevents a formation of the spin-state (HS-LS) order due to $|\text{HS, LS}\rangle \leftrightarrow |\text{IS, IS}\rangle$ fluctuations.

5.4 Conclusions and Outlook

Using Co L_3 -edge RIXS in LaCoO₃ at 20 K we have observed dispersion of the IS (${}^3T_{1g}$) excitations with a sizable bandwidth. The experimental data match well the theoretical calculations in the experimentally accessible part of the Brillouin zone and their extrapolation points to an important role of IS excitations for the low-energy physics of the material. Dispersion dominated by the nearest-neighbor processes allows for reliable extrapolation. Improved energy resolution and polarization analysis would reduce reliance on theoretical model and is therefore highly desirable.

The present results show that the question, whether the first atomic excited state is HS or IS, is not correctly posed. While there is little doubt that the lowest atomic excitation is HS, the propensity of IS states to move on the LS lattice changes the game in the extended system. LaCoO₃, therefore, should not be viewed as a static collection of ions in particular atomic states, but rather as a gas of mobile bosonic excitons (IS) above (LS) vacuum. The HS states play the role of strongly bound and essentially immobile bi-excitons. This picture provides a natural explanation why the spin-state order accompanied by Co-O bond-length disproportionation is not observed in LaCoO₃ despite the low-energy of HS excitations. It further suggests LaCoO₃ and its analogs as potential materials for realization of excitonic magnetism^[250].

Chapter 6

Mixed-valence Cobalt Compounds

In this chapter, I discuss the preliminary Co $2p3d$ RIXS results of two mixed-valence cobalt compounds: Co_3O_4 and $(\text{Pr}_{0.925}\text{Y}_{0.075})_{0.7}\text{Ca}_{0.3}\text{CoO}_3$. For the mixed-valence compounds, the site occupancy is determined by factors such as crystal field energy, bond length, charge occupancy, electron hopping, and configuration interaction. These quantities reflect on the electronic structure which is deeply linked to intrinsic properties such as the magnetism or conductivity. With a proper selected incident energy for Co $2p3d$ RIXS, the chemical sites can be probed independently in the mixed-valence compounds.

6.1 Site Selective Electronic Structure of the Co^{2+} and Co^{3+} in Co_3O_4

Co_3O_4 is widely used in applications of magneto-optical information storage [43, 44], photocatalysis [46–51], batteries [45], or as a visible light emitting material [52]. Co_3O_4 has a normal spinel structure (AB_2O_4) below 850 K [38, 39], where the A site ions are composed by the divalent metal ions (Co^{2+}) in a tetrahedral crystal field and the B site ions are formed by the trivalent metal ions (Co^{3+}) in an octahedral crystal field. The site occupancy is determined by factors such as crystal field energy, bond length, charge occupancy, as well as electron hopping and configuration interaction. These quantities influence the electronic structure which is deeply linked to intrinsic material property [39].

The electronic structure was characterized by the method of optical absorption [53–57] or infrared [58, 59]. The optical absorption presented few excitation features which were located at 0.82, 0.93, 1.64, and 2.81 eV [54]. Various interpretations on the electronic structure have been proposed to assign the spectra [53, 55–57, 59]. Recently, Hibberd *et. al.* performed the Co $L_{2,3}$ -edge ($2p$) X-ray absorption spectroscopy (XAS) as a more sensitive technique to probe the metal valence state, crystal field strength, and coordination geometry [62]. They shown that the electronic structure of Co_3O_4 seems can be simulated well by the reference spectra of well-characterized Co-based polyoxometalates (POMs). But $2p$ XAS is limited by its lifetime broadening of 200 meV and it does not measure the electron transitions within the $3d$ shell (dd excitations), which implies that it is not sensitive enough to detect small distortions on the local environment of the Co ions. The limits lead to the interpretation discrepancy which suggests that other chemical site sensitive technique is required for examining the electronic structure of cobalt oxides [62, 63].

In this section, we investigate the mixed-valence Co ions in the Co_3O_4 through Co $2p3d$ resonant inelastic X-ray scattering (RIXS). The $2p3d$ RIXS exhibits chemical site selective and intense dd excitations in compare with the NIR and UV/Vis, which allows a better determination of the ligand field [63]. From an accurate analysis of high resolution Co $2p3d$ edge RIXS spectra, the energy fine structure can be revealed including the small distortions [6, 7, 63] and the $3d$ spin-orbit coupling [4]. The hybridization of the ions and the ligands can also reflect on the $2p3d$ RIXS spectra [5, 213, 251]. In combination with the theoretical models (e.g. crystal field theory or charge transfer calculations), Co $2p3d$ RIXS can provide additional details about the electronic structures of both the ground state and excited states with the chemical site selectivity in Co_3O_4 .

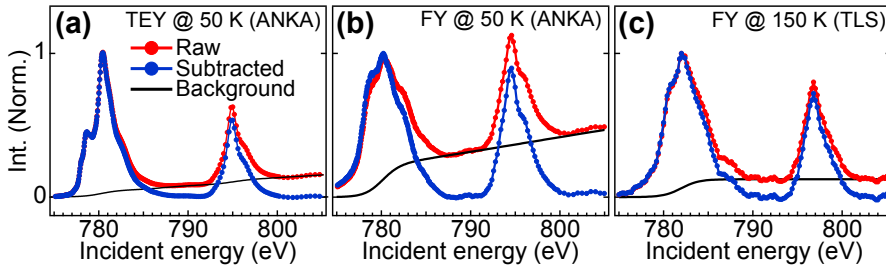


Figure 6.1: The data treatment of XAS spectra. (a) The TEY-XAS and (b) the FY-XAS spectra measured at WERA beamline in ANKA. (c) The FY-XAS spectra measured at soft X-ray RIXS beamline in TLS.

The experiments were performed on the 99.9985% pure Co_3O_4 powder produced by Alfa Aesar. A cylindrical pellet Co_3O_4 with the 10 mm in diameter 0.5 mm in height was prepared for the measurements. Cobalt $2p$ XAS spectra were acquired at the soft X-ray WERA beamline, ANKA synchrotron, Germany. The instrumental resolution was calibrated to be ~ 280 meV full width at half-maximum (fwhm) at $2p3d$ transition edge of Co (~ 780 eV). Both the total electron yield (TEY) method and the fluorescence yield (FY) methods were applied at 50 K. The Co $2p3d$ RIXS measurements were carried out at the BL05A in Taiwan Light Source^[24] with both linearly vertical (V) and horizontal (H) polarized incident X-rays. The experiments were aligned at a grazing incident geometry ($\sim 10^\circ$) with the spectrometer at 90° . The experimental energy resolution of incident photon was ~ 700 meV and the combination resolution of RIXS was ~ 90 meV. The FY-XAS spectrum was also acquired with an incident energy resolution ~ 700 meV at RIXS beamline. The measurements were carried out at 150 K in RIXS beamline. In order to compare the XAS spectra from different beamline and approaches, the background signal introduced by edge jump and particle scattering were subtracted from the spectra as shown in Fig. 6.1. The subtracted spectra were normalized to the strongest peaks at Co L_3 -edge. The photon energy in RIXS beamline were calibrated to the spectra acquired in WERA beamline. For the RIXS spectra, all the spectra of H-polarized incident beam were normalized to the exposure time. Then the V-polarization spectra were normalized to H-polarization spectra according to the energy loss profile above 2.5 eV.

Figure 6.2 shows the XAS and RIXS results. The TEY spectrum shows clearly a sharp feature at about 780 eV and few satellites before the main peaks. They might corresponds to the characteristic features of the $\text{Co}^{3+} {}^1A_{1g}(\text{O}_h)$ and the $\text{Co}^{2+} {}^4A_2(\text{T}_d)$ ground states^[62], respectively. The FY absorption spectra are

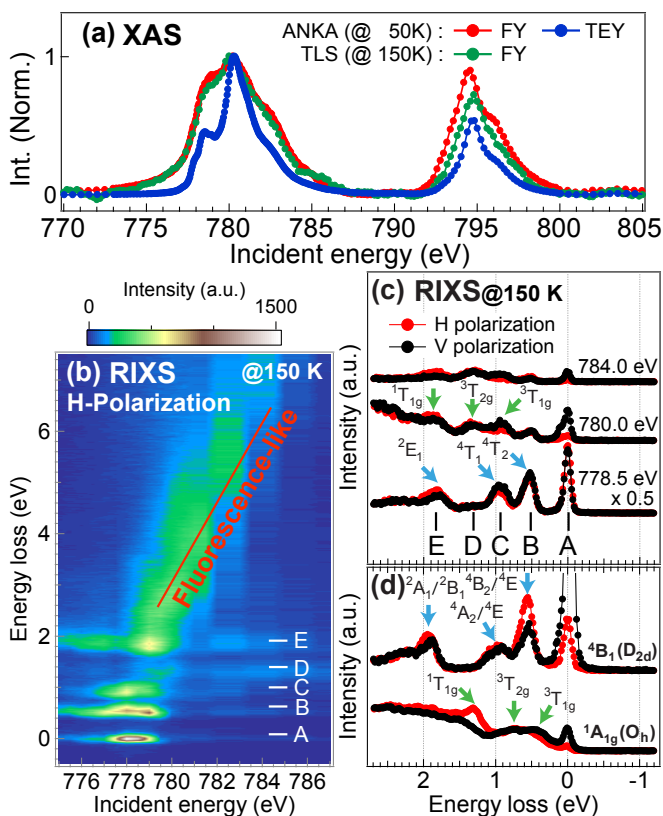


Figure 6.2: The Co $2p$ XAS and $2p3d$ RIXS experimental results of Co_3O_4 . (a) The XAS spectra. (b) The H-polarized RIXS map. (b) The comparison of H- and V- polarized RIXS spectra. (d) The reference RIXS spectra at the maximum of resonant edge for the LS $^1A_{1g}(O_h)$ and the HS $^4B_{1g}(D_{2h})$ ground states, which were obtained by the measurements on the LaCoO_3 crystal at 20 K and $\text{K}_5\text{H}[\text{CoW}_{12}\text{O}_{40}] \cdot x\text{H}_2\text{O}$ at 300 K, respectively.

strongly distorted due to that for the high condense Co_3O_4 sample exhibits strong saturation and self-absorption effects. This effect saturates the most intense features and effectively increases the low-intensity features. Excitons can be observed in the RIXS results and they have been indicated with capital letters from A to E (Fig. 6.2b). Their excitation energies are 0, 0.5, 0.9, 1.2, and 1.9 eV, respectively. A fluorescence-like signal can be observed and its excitation energy increases with increasing incident photon energy as indicated. The excited states A-C are resonant at 778 eV incident photon energy and the excited state D is resonant at ~ 780 eV. The excited state E is resonant at an energy ~ 779 eV.

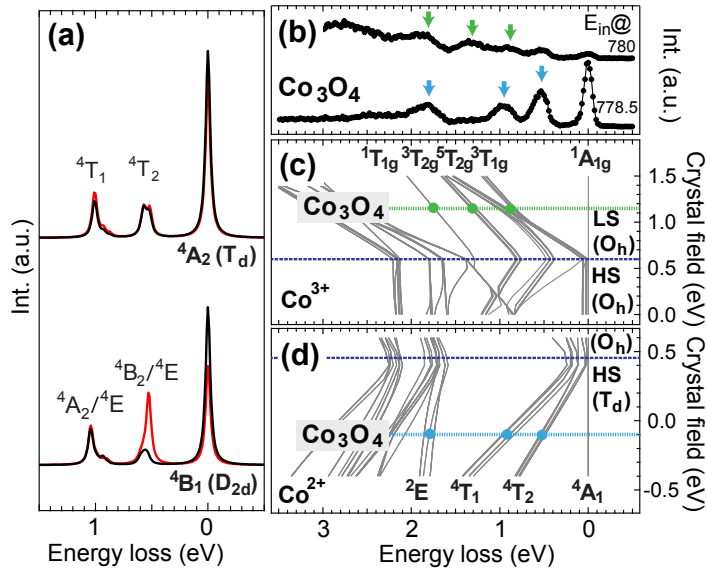


Figure 6.3: (a) Polarization dependence of distorted and non-distorted tetrahedral Co^{2+} . The calculation was carried out by applying the parameters has been used in reference [7], where charge transfer interaction was not included. (b) The selected $2p3d$ RIXS spectra of Co_3O_4 . (c)-(d) The energy diagrams of the Co^{3+} ion (c) and the Co^{2+} ion (d) as a function of crystal field energy including the charge transfer interaction.

To gain more insight into the excited states characteristic, figure 6.2c shows the spectra which were measured by two linear orthogonal polarized incident beams. The feature at ~ 0.9 eV is enhanced by the V-polarized incident photon but the feature at ~ 1.9 eV has opposite behaviour. This polarization dependence is similar to the ${}^3T_{1g}(O_h)$ and ${}^1T_{1g}(O_h)$ excited states of the LaCoO_3 crystal at 20 K (see Fig. 6.2d), where the Co^{3+} ions have the LS ${}^1A_{1g}(O_h)$ ground state configuration. However, in the LaCoO_3 crystal, both the states are located at the lower energy than what we observe in Co_3O_4 , see Fig. 6.2d. The feature at about 0.5 eV can be identified as the 4T_2 excitation feature of tetrahedral Co^{2+} [59]. We compared it to a reference spectra of the distorted tetrahedral Co^{2+} in the $\text{K}_5\text{H}[\text{CoW}_{12}\text{O}_{40}] \cdot x\text{H}_2\text{O}$ [7], where the ground state of the Co^{2+} ions shows the HS ${}^4B_1(D_{2d})$ configuration. Due to the distortion, the ${}^4T_2(O_h)$ state splits into ${}^4B_2(D_{2d})$ and ${}^4E(D_{2d})$ states. It gives rise to the strong polarization dependence on the feature at about 0.5 eV, see Fig. 6.2d and 6.3a. However, no dichroism intensity at ~ 0.5 eV is observed in Co_3O_4 . It shows that the distortion of the

Table 6.1: The Slater Integral, crystal field energy, spin-orbit coupling energies, charge transfer energy, hopping energy, U_{dd} and U_{pd} used in the Simulation (in eV). The i and m stand for the configurations of initial ground state and intermediate state, respectively.

	F_{dd}^2	F_{dd}^4	F_{pd}^2	G_{pd}^1	G_{pd}^3	ζ_p	ζ_d
Co_i^{2+}	9.284	5.767	-	-	-	-	0.066
Co_m^{2+}	9.917	6.166	5.808	4.318	2.455	9.748	0.066
Co_i^{3+}	9.371	5.859	-	-	-	-	0.055
Co_m^{3+}	9.932	6.212	5.925	4.463	2.540	9.747	0.055
	10Dq	10Dq _{eff}	Δ	V_{eg}	V_{t2g}	U_{dd}	U_{pd}
Co_i^{2+}	-0.1	~ -0.55	4.5	1.0	2.0	4.5	-
Co_m^{2+}	-0.018	~ -0.47	4.5	1.0	2.0	4.5	6.0
Co_i^{3+}	1.15	~ 2.10	1.5	3.12	1.8	6.5	-
Co_m^{3+}	0.84	~ 1.79	1.5	3.12	1.8	6.5	7.5

tetrahedral Co^{2+} site in Co_3O_4 is neglectable, which agrees with the calculation (Fig. 6.3a). Thus we labelled the configuration of non-distorted tetrahedral Co^{2+} by HS ${}^4A_1(T_d)$.

Accordingly, we can simulate the characteristic features in comparison with the energy diagram (Fig. 6.2b-d). The features at about 0.9, 1.3, and 1.9 eV were recognized as the contributions of Co^{3+} (green arrows in Fig. 6.3b), which can be simulated by an optimized crystal field energy (10Dq) ~ 1.15 eV from energy diagram (Fig. 6.3c). The ligand to metal charge transfer provides an additional contribution to the 10Dq, which implies an effective crystal field energy (10Dq_{eff}) of ~ 2.1 eV. This implies that the LS ${}^1A_{1g}(O_h)$ ground state configuration of the Co^{3+} ion in the Co_3O_4 is further away from the spin state crossover than in the $LaCoO_3$ crystal. It suggests that the ground state of Co^{3+} in Co_3O_4 always carries the LS characteristic. The distortion on the Co^{3+} site is omitted because of it only induces minor effects on the polarization dependence for the ${}^1A_{1g}$ ground state. For the Co^{2+} ions, we also obtained an optimized 10Dq at ~ -0.1 eV (see Fig. 6.3d). It implies a 10Dq_{eff} value is ~ -0.55 eV associated with the hybridized contribution, where the negative sign of 10Dq_{eff} indicates an energy inversion due to the T_d symmetry. The excitations at 0.5, 0.9, 1.9 eV in the 6.3b agree with the feature in Co_3O_4 . All the optimized parameters are presented in Table 6.1. We note that because of the contraction of the $3d$ wave function induced by the core hole^[201], we applied the 10Dq_{eff} value of the intermediate state is

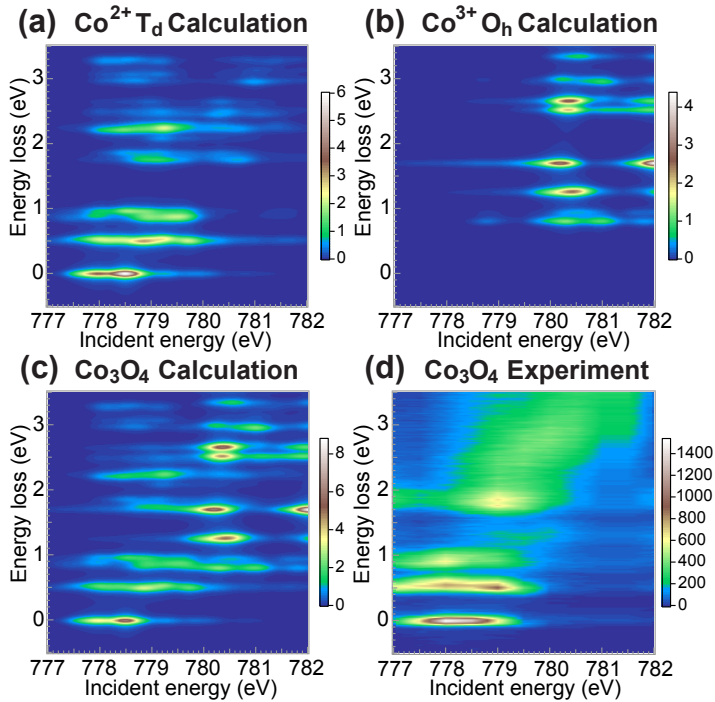


Figure 6.4: The $2p3d$ RIXS (a)-(c) simulated results and (d) experimental result. (a) and (b) present the calculation intensity per cobalt ion for the HS $\text{Co}^{2+} \ ^4\text{A}_{1g}$ (T_d) and the LS $\text{Co}^{3+} \ ^1\text{A}_{1g}$ (O_h) ground states, respectively. (c) The summations of two Co^{3+} at O_h site and one Co^{2+} at T_d site. (e) Experimental result.

reduced by 15% in comparison with the ground state.

The simulated intensity of RIXS are given in Fig. 6.4a and 6.4b for the HS $\text{Co}^{2+} \ ^4\text{A}_1(T_d)$ and the LS $\text{Co}^{3+} \ ^1\text{A}_{1g}(O_h)$ ground states. It has been discussed above that the former configuration exhibits the characteristic features at about 0.5, 0.9, 2 eV and the later on has characteristic features at about 0.9, 1.3, 1.8 eV, which were identified as the 4T_2 , 4T_1 , and 2E excited states and $^3T_{1g}$, $^3T_{2g}$, and $^1T_{1g}$ excited states, respectively. The intensity of zero energy loss is mainly caused by the HS $\text{Co}^{2+} \ ^4\text{A}_1(T_d)$ ground state. Because the LS $\text{Co}^{3+} \ ^1\text{A}_{1g}$ state is strongly suppressed when it is probed by H-polarized photon at the scattering angle about 90° . Figure 6.4c shows the sum of two components by the ratio of 1:2 for the Co^{2+} and Co^{3+} , according to the ratio of stoichiometric values (1:2). For the $2p$ XAS spectra, a ratio of 3:8 is applied for the normalized (to total area) Co^{2+} and Co^{3+} spectra, according to the ratio of stoichiometric values (1:2) and

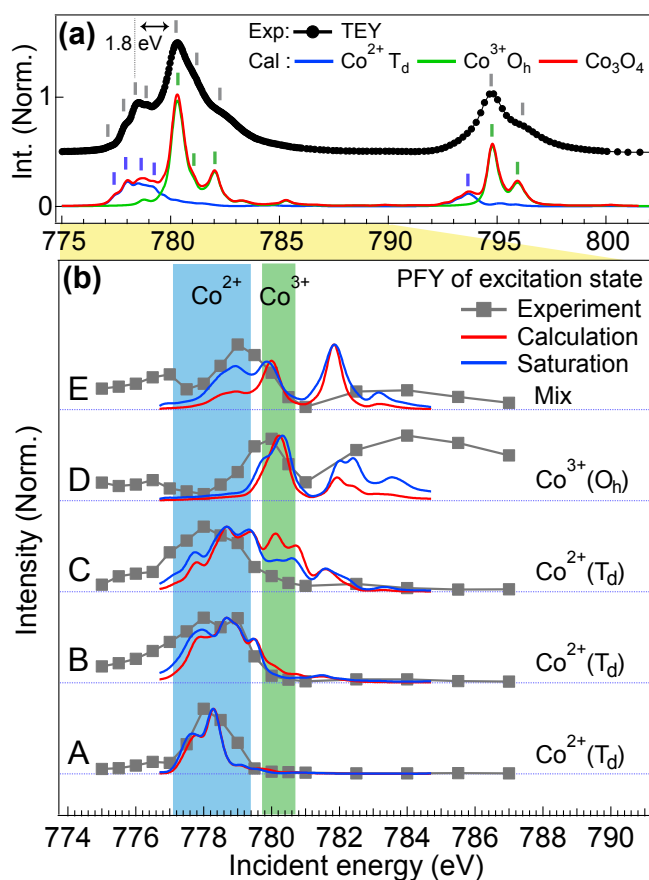


Figure 6.5: The comparison of XAS spectra. (a) TEY spectra. (b) PFY spectra of the excitation A-E.

the ratio of number of holes (3:4). The incident energy shift was adjusted to 1.8 eV between two sites as shown in Fig. 6.5a. The simulation shows general agreements on the excitation energy and resonant behavior with the experimental result (Fig. 6.4d).

By comparing the simulated and experimental TEY and PFY absorption spectra (Fig. 6.5), we show the chemical site selectivity. The PFY absorption spectra were obtained by the fitting intensity of the excitation features A-E experimentally and summation in a energy window with respect to the excitation features A-E theoretically from Fig. 6.4d and 6.4c, respectively. In the TEY results (Fig. 6.5a), the characteristic XAS features of Co^{2+} (blue bars) and Co^{3+} (blue bars) are well

simulated to the experimental features (gray bars), which is in agreement with the literature^[62]. Figure 6.5b presents the PFY absorption spectra in the energy region of L₃ edge. It shows that the excitation A-B are mainly contributed by the Co²⁺ site and the excitation D is almost solo contributed by the Co³⁺ site. The features C and E show mixture of two site in calculation but it the intensity of Co²⁺ is more pronounced. However, a systematic discrepancy is observed that the intensity at about 780 eV were always overestimated in the calculation. This discrepancy could be the consequence of saturation and self-absorption effect, which has already shown that the FY absorption spectra in Fig. 6.2a.

If the incident photons are fully absorbed by the sample, the correction formula of saturation and self-absorption effect can be described as^[229]:

$$I_{ems} = I_0 \frac{S_X(\omega_{in}, \omega_{out})\mu_X(\omega_{in})}{\mu(\omega_{in}) + \mu(\omega_{out}) \frac{\sin\theta}{\sin(\alpha-\theta)}}, \quad (6.1)$$

where the X , α , and θ stand for the emission edge of element X , the scattering angle, and the sample rotation angle, respectively. In currently work, we have measured the Co L₃ edge with an experimental geometry $\alpha = 90^\circ$ and $\theta = 20^\circ$. The $\mu(\omega_{in})$ and $\mu(\omega_{out})$ are the absorption factor of absorption and emission channel in RIXS. The combination of the emission $S_X(\omega_{in}, \omega_{out})$ and absorption $\mu_X(\omega_{in})$ terms give the RIXS intensity. In the correction, we assumed a background absorption factor is about 10% form the maximum of Co L₃ edge. The equation implies that the spectra are saturated more strongly with a larger absorption factor. Thus, after the saturation and self-absorption corrections, the features located at about 780 eV of PFY spectra are suppressed. It leads to that the PFY spectra intensity of excitation C is shifted to lower energy and the PFY spectra intensity at about 782 eV of excitation D is enhanced, which shows better agreement with the experimental results, see Fig. 6.5b.

Through the analysis above, the features at 0.5 eV and 1.3 eV can be clearly identified as the characteristic features of the ⁴T_{2g} excited state on the tetragonal Co²⁺ site and ³T_{1g} excited state on the octahedral Co³⁺ site. It confirms that the Co₃O₄ is mainly composed by the tetragonal Co²⁺ and octahedral Co³⁺, which is an ideal normal spinel structure. Due to the limited discriminative power of optical techniques, to the best of our knowledge, the ⁴A₂ to ⁴T₂ excitation was only reported by Mironova *et al.* through infrared more than two decades ago^[59].

One remark is that the broadening were considered as the same of the both sites in the simulation, which match the features of Co²⁺ site well. However, the broadening seems smaller than the experimental result on the Co³⁺ site. This

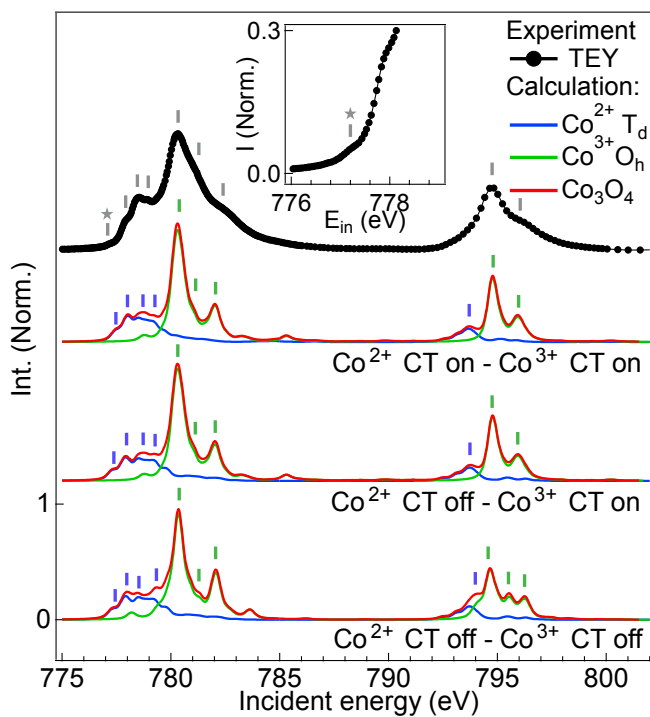


Figure 6.6: The comparison of XAS spectra with and without including the charge transfer (CT) effect.

could be due to the hybridization strains are different in each sites. With a stronger hybridization strain, the spectra become more delocalized and implies larger life time broadening. Thus, the broadening on Co^{3+} site is expected to be larger. Figure 6.6 demonstrates the simulation of XAS spectra including and excluding the ligand to metal charge transfer hybridization. Without considering the charge transfer hybridization on both Co^{2+} and Co^{3+} sites, the XAS spectra shows poor agreement with the experimental result. If we apply the charge transfer hybridization on Co^{3+} site, the agreement has improved, which implies that the Co^{3+} is much more sensitive to the hybridization effect which might enlarge the broadening. Furthermore, it has been suggested in the literature that both the Co^{2+} and Co^{3+} sites are hybridized strongly to the ligands^[252]. By including the hybridization effect on both the Co^{2+} and Co^{3+} sites, the simulation result shows best agreement. It implies that the ground state configuration is mixture of the $3d$ orbit and ligand hole (L). The weight of configurations up to two ligand holes are listed in Tale. 6.2.

Table 6.2: The weight of configurations and orbital covalency in ground state (unit in %). The number of ligand holes is considered up to two.

	$ 3d^n\rangle$	$ 3d^n\underline{L}^1\rangle$	$ 3d^n\underline{L}^2\rangle$	e_g covalency	t_{2g} covalency
$\text{Co}^{2+}(3d^7)$	79	20	1	80	100
$\text{Co}^{3+}(3d^6)$	40	50	10	100	50

We can estimate the orbital covalency of Co^{2+} and Co^{3+} sites by following relation ^[213]:

$$\text{Covalency}(\gamma) = 100\% - \mathcal{N} \frac{P_\gamma}{P_{sum}}, \quad (6.2)$$

where γ stands for the state corresponding to the e_g or t_{2g} orbitals. The coefficient \mathcal{N} is a renormalization factor of the number of holes in the orbit γ out of number of holes in $3d^n$ configuration. For example, in the case of HS $\text{Co}^{2+}(\text{T}_d)$, there are three holes in the t_{2g} orbit out of three holes in $3d^7$ configuration. Hence the renormalization factor is equal to one ($\frac{\text{number of holes in } 3d^n}{\text{number of holes in } t_{2g}} = 1$). In contrast, the renormalization factor for the e_{2g} orbit is meaningless because it is fully occupied (no hole exist). The P_γ is the percentage for the configuration which accepts the electrons transfer from ligand to the orbital γ . Note here that we only consider one electron transfer in the covalency estimation. P_{sum} is the percentages summation of all possible configurations involved in the hybridization, which is equal to one in current cases. Thus the orbital covalency of t_{2g} orbital on the Co^{2+} site and e_g orbital on Co^{3+} site are given as $\sim 70\%$ and $\sim 40\%$, respectively. It implies again that the hybridization effect on Co^{3+} site is larger than on Co^{2+} site and agrees with the literature^[252].

In addition, we compare the optimized parameters to the values extracted from a first principle density function theory calculation. The calculation was performed in the local density approximation, which was projected in Wannier orbitals^[243, 244]. By expanding the Wannier orbitals in the atomic orbitals, the effective correlations can be obtained. We found that the crystal field energy on the O_h Co^{3+} is ~ 0.7 eV with a small trigonal distortion $D_\sigma = 0.05$ eV. In currently result, the distortion effect cannot be observed. The hopping intensities $V_{a_{1g}}$, $V_{e_g, \pi}$ and $V_{e_g, \sigma}$ are respectively ~ 1.6 eV, ~ 1.46 eV and ~ 0.8 eV. This implies the average value to simulate the ideal O_h symmetry with the hopping intensity $V_{t_{2g}} \sim 1.74$ eV and $V_{e_g} \sim 3.03$ eV, which are similar as the values used ($V_{t_{2g}} \sim 1.8$ eV; $V_{e_g} \sim 3.12$ eV). The theoretical crystal field energy for the O_h Co^{3+} (~ 0.7 eV) is much smaller that what we obtained from simulations (~ 1.15 eV). The theoretical value might underestimated the intra-atom electron-electron interaction in

a d -shell only model, which will might effective increase the crystal field energy. Moreover, the strong hybridization on the Co^{3+} site implies that the O_h site ion becomes more d^7 like rather than d^6 . The complex mixture attributes the bias in the theoretical estimation. For the T_d Co^{2+} site, the theoretical parameters are -0.1 eV for crystal field energy and $1.29(1.82)$ eV for the hopping intensities $V_{e_g}(V_{t_{2g}})$. The values on the T_d Co^{2+} are comparable to the values applied for the simulation ($10Dq = -0.1$ eV; $V_{e_g} \sim 1$ eV; $V_{t_{2g}} \sim 2$ eV).

In summary, we present the Co $2p$ XAS and $2p3d$ RIXS experimental results in comparison with the cluster model simulation. By selecting the characteristic features of each configuration, the PFY spectra has the ability to differentiate the chemical sites. The 4A_1 to 4T_2 excitation of tetrahedral Co^{2+} site at 0.5 eV is clear observed beyond the discriminative power of traditional optical absorptions. In contrast, the ${}^1A_{1g}$ to ${}^1T_{1g}$ excitation of octahedral Co^{3+} site at 1.3 eV can be identified. Through the analysis, the ground state electronic structure of the Co^{2+} ions and Co^{3+} ions are once confirmed as HS ${}^4A_{1g}(T_d)$ and LS ${}^1A_{1g}(O_h)$ states. The spectra also suggests that both of the Co^{2+} and Co^{3+} sites are hybridized strongly to the ligands.

6.2 The Spin State Transition of the Co^{3+} Site in $(\text{Pr}_{0.925}\text{Y}_{0.075})_{0.7}\text{Ca}_{0.3}\text{CoO}_3$

Cobalt perovskites are rich in their spin and orbital degrees of freedom, yielding many attractive magnetic and transport properties. For example, bulk LaCoO_3 exhibits a magnetic transition from a diamagnetic phase to a paramagnetic phase at ~ 100 K and an insulator-metal transition at ~ 500 K^[67–71, 71, 72], where spin-state changes were also suggested in both cases^[69, 73]. With a substitution of other rare-earth ions, both the magnetic and the transport properties can be manipulated^[69, 92]. Replacing La ions with Eu ions can gradually shift the insulator-metal transition to a higher temperature^[69]. The insulator-metal transition can be explained by a three step model which describes the transitions starting from a low-spin (LS) ground state through a low-spin/high-spin (LS/HS) mixture phase at the middle temperature region then end up at a metallic intermediate-spin (IS) phase^[106, 132].

A similar magnetic transition associated with the insulator-metal transition has also been observed in $(\text{Pr}_{1-y}\text{R}_y)_{1-x}\text{Ca}_x\text{CoO}_3$ ($\text{R}=\text{Nd, Sm, Eu, Gd, Tb, Y}$)^[136, 138]. In case of $(\text{Pr}_{0.925}\text{R}_{0.075})_{0.7}\text{Ca}_{0.3}\text{CoO}_3$ ($x=0.3, y=0.075$), a clear transition has been shown at ~ 64 K on all the properties like conductivity, magnetic susceptibility, and heat capacity. This insulator-metal transition can also be driven by an external high magnetic field^[253, 254]. Generally, it was accepted that the electronic configuration of the Co^{3+} ions in such compounds exhibits a LS characteristic at low temperature and switches to a IS or a HS characteristic similar to the case of LaCoO_3 ^[255–258]. The transition is not only associated with the spin state change but also with a significant charge transfer between $\text{Pr}^{3+}/\text{Pr}^{4+}$ and $\text{Co}^{4+}/\text{Co}^{3+}$ sites^[138, 253, 259, 260].

In this section, we examine the spin-state characteristic of Co^{3+} ions in the sample $(\text{Pr}_{0.925}\text{Y}_{0.075})_{0.7}\text{Ca}_{0.3}\text{CoO}_3$ using $2p3d$ resonant inelastic X-ray scattering (RIXS). The RIXS measurement is sensitive to the ground and the excited states including their charge, spin, and orbital flavors^[1]. In particular, it has been shown that the quasi-degenerate Co $3d$ atomic multiplets can be distinguished successfully through the $2p3d$ RIXS on the cobalt perovskite^[103, 125]. Thanks to the orbital and chemical site selectivity, we can pinpoint a particular covalency of the specimen. Furthermore, in the excitonic condensation picture, nonzero spin-triplet excitonic condensation order parameter suggests a gap open in the one-particle spectra below the transition temperature^[237]. Such spin-triplet was indicated as the dispersive IS exciton in the undoped LaCoO_3 ^[113] and has been observed by $2p3d$ RIXS^[214]. In other words, $2p3d$ RIXS is a unique tool to reveal the complex competition between the local and collective electrons in the

cobaltites.

The Co $2p3d$ RIXS measurements were performed at the BL05A in Taiwan Light Source (TLS)^[24]. Both the linearly vertical (V) and horizontal (H) polarized incident X-rays were applied. The experimental energy resolution of the incident beam was ~ 700 meV and the combined resolution of RIXS was ~ 90 meV. The experiments were performed with a grazing incident geometry ($\theta \sim 10^\circ$) with the spectrometer at 90° . The fluorescence yield X-ray absorption spectra (FY-XAS) were also acquired with an incident energy resolution ~ 700 meV. Our polycrystalline sample was fabricated by a solid-state reaction and the synthesis details have been described by Hejtmaek et al.^[138]. The sample particles were spread on carbon tape attached to an oxygen free copper holder.

In order to distinguish the chemical site of the cobalt, we performed both the FY-XAS and RIXS measurements at 20 K (Fig. 6.7a). From the FY-XAS spectra, we observe one clear asymmetry feature at the Co L_3 edge. No clear shoulder above the edge is observed as found in the LS Co^{3+} ^[79, 97, 258], which implies that the contribution of the LS Co^{3+} state is small. The absence of multiplet features in the FY-XAS spectra prevents the determination of further significant information.

The selected incident energies for RIXS were illustrated as the blue bars in the figure. Note that the incident energies were not calibrated to a reference, so we indicated the energies relative to the main peak of Co L_3 edge in this work. The energy dependent RIXS spectra were measured by both V- and H- polarized incident photons, see Fig. 6.7b. We compared the results to a polarization dependent LS-like Co^{3+} RIXS spectra of the LaCoO_3 crystal at 20 K (bottom panel) and found that the polarization dependent RIXS signal (arrows in Fig. 6.7) before the main Co L_3 (~ 780 eV) of the $(\text{Pr}_{0.925}\text{Y}_{0.075})_{0.7}\text{Ca}_{0.3}\text{CoO}_3$ resembles the LS-like Co^{3+} RIXS spectra. Generally, the excitation energy increases with the increase in covalency. The spectra above the edge indicates a mixture of Co^{3+} and Co^{4+} . This implies that there is a smaller polarization dependence above the L_3 edge, see Fig. 6.7. No octahedral- Co^{2+} -like features^[4, 213] or tetrahedral- Co^{2+} -like features^[7] were observed, which implies that the RIXS spectra before the main Co L_3 (~ 780 eV) edge of the sample are mainly probing the Co^{3+} ions.

The incident energy at L_3-3 eV was selected for the temperature dependent measurement to focus on the Co^{3+} ion site in $(\text{Pr}_{0.925}\text{Y}_{0.075})_{0.7}\text{Ca}_{0.3}\text{CoO}_3$. In addition, this excitation energy avoids the fluorescence signal^[103, 125]. The temperatures were adjusted at 20 K and 120 K which are well below and above the insulator-metal transition temperature of (~ 64 K). FY-XAS spectra were also performed by V-polarized incident X-rays. A noticeable difference between the low and high temperature results is the intensity enhancement at about 778 eV,

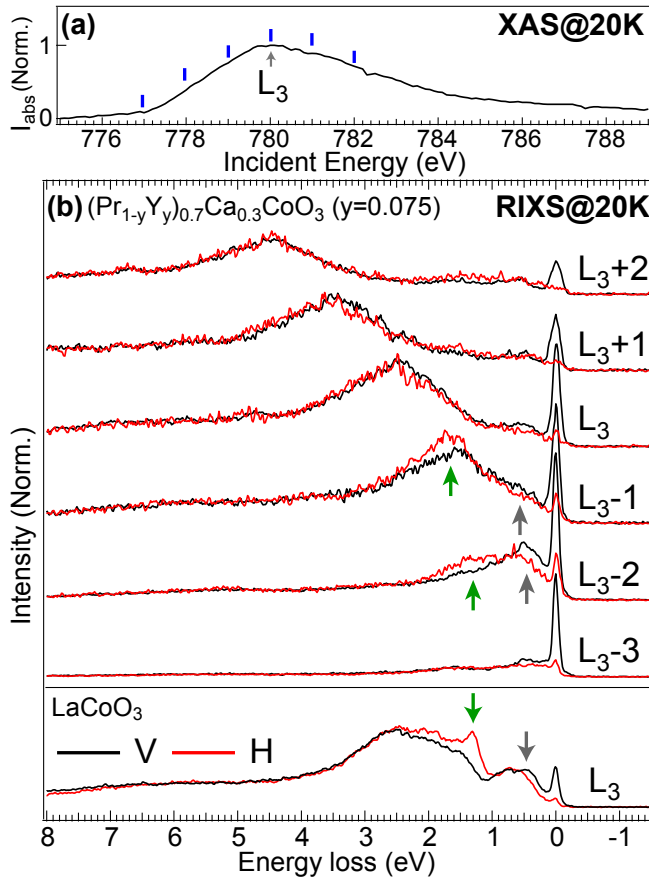


Figure 6.7: The energy dependent RIXS spectra at 20 K on the polycrystalline $(\text{Pr}_{0.925}\text{Y}_{0.075})_{0.7}\text{Ca}_{0.3}\text{CoO}_3$ sample. The figure in the bottom panel shows polarization dependent RIXS on a LaCoO_3 crystal in a similar experimental geometry. Note here that the V-polarized spectra were normalized to the exposure time and the H-polarized spectra were normalized to the intensity above 4 eV of V-polarized spectra.

see Fig. 6.8a. With an increasing of the temperature, the thermal excited states provide a possibility to be probed in the $2p3d$ transition signal on the XAS spectra. It has been reported that the increase of the pre-edge feature indicates the LS to HS transition^[79, 97, 258]. However, Abbate *et al.* indicated that the transition corresponds to the high temperature spin state transition which suggests a mixed spin state^[79, 103]. Thus, according to the XAS spectra, both the metallic IS and HS Co^{3+} multiplets could be the potential thermal excited configurations. Figure 6.8b

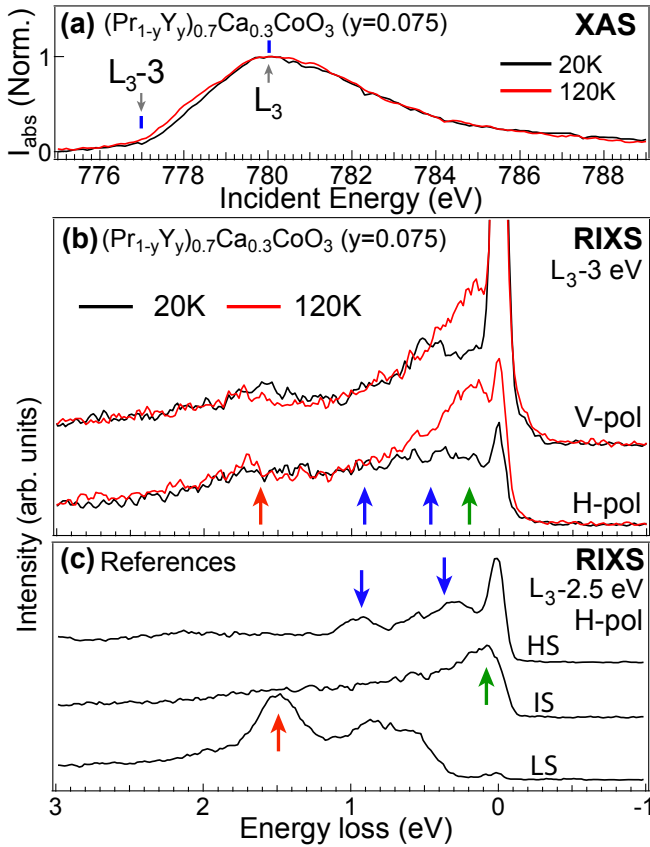


Figure 6.8: The temperature dependent measurements at 20 K and 120 K. (a) The XAS spectra and (b) the RIXS spectra of the polycrystalline $(\text{Pr}_{0.925}\text{Y}_{0.075})_{0.7}\text{Ca}_{0.3}\text{CoO}_3$ sample. (c) The reference RIXS spectra of the compounds $\text{Sr}_2\text{CoO}_3\text{Cl}$, $\text{La}_2\text{Co}_{0.5}\text{Ni}_{0.5}\text{O}_3$, and EuCoO_3 which are stand for the HS, IS, and LS ground states, respectively. The spectra were grabbed from the reference [103].

shows the results including both the V- and the H- polarized incident photons. To extract the signal contributed from the different spin states, we adopted the experimental reference obtained from literature^[103], see Fig. 6.8c. The spectra of the compounds $\text{Sr}_2\text{CoO}_3\text{Cl}$, $\text{La}_2\text{Co}_{0.5}\text{Ni}_{0.5}\text{O}_3$, and EuCoO_3 respectively represent the HS, IS, and LS ground states of Co^{3+} ions^[103, 261, 262]. In Co^{3+} $2p3d$ RIXS, they provide the characteristic excitation features at 0.4 and 0.8 eV for a HS ground state (blue arrows), at 0.2 eV for a IS ground state (green arrow), and 1.5 eV at a LS ground state (red arrow). Comparing the reference spectra to the temperature

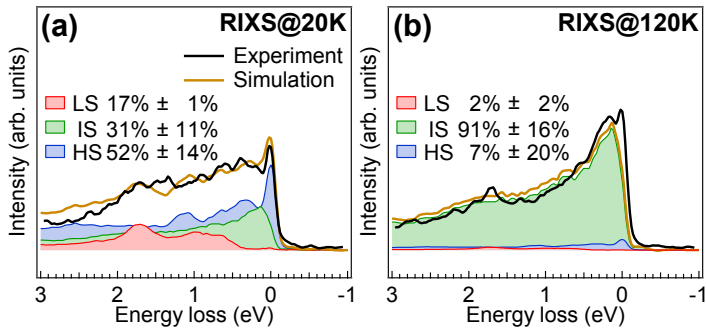


Figure 6.9: The comparisons between the experimental results and the simulated spectra with a spin-state ratio as indicated for the results (a) at 20 K and (b) at 120 K.

dependent results on the $(\text{Pr}_{0.925}\text{Y}_{0.075})_{0.7}\text{Ca}_{0.3}\text{CoO}_3$ sample, we observed that all the LS, IS, and HS states contributed to the RIXS signal at 20 K (see Fig. 6.8b). In contrast, the RIXS spectra at 120 K shows that the signal from the IS state is much enhanced (green arrow in Fig. 6.8b). We remark that the measurement did not reproduce well on the powder sample aged for a year in a vacuum environment. We concluded that the Co^{4+} ions are not stable in vacuum and the (surface of the) sample is reduced to Co_3O_4 .

To indicate the contributions of the three different spin states, we fitted the spectra by a linear combination of the three reference spectra. We note that the spectra of references were not considered at the same incident energy as our experiments and the spectra are normalized to the summation area from -1 eV to 3 eV. Although they might affect the precision of quantification, the dominating spin state configuration still can be identified. On the other hand, the crystal field potential and the intra electron-electron interaction might not be the same in different compound. Therefore, the excitation energies of the characteristic features might be changed by applying a different crystal field energy (10Dq) or electron-electron interaction energy (Slater Integral). Figure 6.9 shows the rough quantified results, where the energy scale of the spectra has been rescaled by the factor 1.1, 1.3 and 1.3 respectively for the LS, IS, and HS spectra in order to match the characteristic feature and simulate the interaction difference. In Fig. 6.9a, we found that the HS state dominates the ground state and provides more intensity on the spectra at 20 K. Furthermore, both of the LS and IS states seems also to coexist together with the HS state. In contrast, at the 120 K (Fig. 6.9b), the signal from IS state dominated the spectra. It suggests that the insulator-metal transition seems

to be accompanied with the transition from a LS/IS/HS mixture state to a nearly pure IS state.

This observation disagrees with few of the existing explanations^[255–258], where it is assumed that the low temperature phase exhibits a LS state on the Co^{3+} site. Theoretical analyses show the coexistence of a LS/HS or LS/IS mixed phase should have an ordering structure in cobaltites^[106, 107]. To explain this, a plausible picture is the spin-state fluctuation between the LS/HS phase and IS/IS phase^[106]. In this spin-state fluctuation scenario, below the transition, the long-range order of mixed LS/HS phase might be prevented by the increased of entropy. It implies that the mixed LS/HS phase tend to short range order arrangement. It also provides a bias to the discrimination of the spin state characteristic in the low temperature phase. Increasing the population of IS clusters has tendency to change the LS/HS phase into a uniform IS phase. On the other hand, the excitonic condensation scenario will be another plausible explanation^[237, 263]. At the low temperature, the nature of the ground state is a mixture state of the LS, IS, and HS states. The coexist of the LS and HS are tend to from a antiparallel spin orientated order but the mobile IS state tend to suppress the order^[214]. As the temperature increase, the excitonic gap disappears in part of the momentum transfer q . When we average the energy over all the q values, the center-of-mass of the IS exciton energy will come close to zero, which agrees to the experimental results. In addition, the disappearing excitonic gap also suggests that the formation of a quasidegenerate state including also high IS state population. This leads to the RIXS spectra become more IS-state-like.

In conclusion, we show the temperature dependence Co $2p3d$ RIXS experimental results on the $(\text{Pr}_{0.925}\text{Y}_{0.075})_{0.7}\text{Ca}_{0.3}\text{CoO}_3$ compound. Below the transition temperature, a mixed state of LS, IS, and HS states is presented. Particularly the contribution from the LS state is much less that the general agreements. As the temperature increase, more IS state are found. It indicates the insulator-metal transition of the $(\text{Pr}_{0.925}\text{Y}_{0.075})_{0.7}\text{Ca}_{0.3}\text{CoO}_3$ sample strong correlates with a spin-state transition characterized as the LS/HS-IS/IS transition.

Summary and Outlook

This thesis is focused on the study of cobalt-containing materials, and in particular of cobalt oxides, with resonant inelastic x-ray scattering (RIXS). I have studied different aspects of the electronic and magnetic structure of cobalt oxides, including charge transfer and hybridization effects, the nature of the competing spin states, the support-induced strain effect in thin oxide films, exciton dispersion and mixed valence phenomena. These effects have been studied with Co $2p3d$ RIXS measurements that are applied to binary cobalt oxides, cobalt perovskites, cobalt halides and cobalt sulfides. In order to interpret the high resolution $2p3d$ RIXS data I have used a number of theoretical methods based on charge transfer multiplet models.

In chapter 2, I discussed the ligand-metal hybridization as well as the electron transport properties of cobalt sulfides and halides. $2p3d$ RIXS spectra can provide accurate values of the charge transfer energy Δ and the crystal field parameter $10Dq$, where the crystal field parameter is split into ionic and charge transfer contributions. In order to compare the experiments with the simulation results from the cluster calculations, proper constraints are required to reduce the number of parameters. I have shown that the additional crystal field energy caused by the charge transfer effect is approximate linear to Δ . In addition, the L_2 -edge RIXS spectra are analyzed with respect to the integrated intensity ratio between resonant ($2p_{1/2}3d$) and non-resonant ($2p_{3/2}3d$) X-ray emissions, which are ~ 0.55 , ~ 1.06 , ~ 1.22 , and ~ 1.71 for CoF_2 , CoCl_2 , CoBr_2 , and CoS , respectively. These numbers show that the Coster-Kronig channel is stronger in CoS and I concluded that the ratio between resonant and non-resonant decay is a potential tool to probe the effects of electron delocalization.

Chapter 3 presents the polarization dependent $2p3d$ RIXS spectra of strained and unstrained LaCoO_3 . By studying the polarization dependence of spectra, the charge, spin, and orbital characteristic of the states can be clarified due to the symmetry selectivity of polarized photons. I compared the experimental results with the simulation in a fixed volume approach. This fixed volume model is pro-

posed to limit the degree of freedom on empirical parameters, which preserves the symmetry characteristic and provides a systematic discussion. Guided by the polarized incident photon analysis, I learned that the Co^{3+} ions are dominated by the $^1A_{1g}(\text{O}_h)$ state in LaCoO_3 single crystal. In addition to the $^1A_{1g}(\text{O}_h)$ state, $^5B_{2g}(\text{D}_{4h})$ and $^5E_g(\text{D}_{4h})$ states contribute partially to the ground state in the tensile- and compressive-strained LaCoO_3 films on SrTiO_3 and LaAlO_3 , respectively. It shows that the $2p3d$ RIXS are able to distinguish the state mixture through the polarization dependent behaviors of ground state and excited state. The agreement between simulations and experiments suggests that the high-spin Co^{3+} can be the trigger of long-range ferromagnetic order due to the possible existence of quantum-chemical mixed spin states.

Moreover, I demonstrated the angular dependent analysis of the $2p3d$ RIXS of the low-spin $^1A_{1g}(\text{O}_h)$ and high-spin $^5B_{2g}(\text{D}_{4h})$ ground states in chapter 4. The polarization dependence is not only determined by the difference between two orthogonal linearly polarized incident beams but also influenced by the experimental geometry. A remarkable consequence is that the isotropic low-spin $^1A_{1g}(\text{O}_h)$ ground state shows angular dependent $2p3d$ RIXS spectra, in contrast to the absence of angular dependence in the $2p$ XAS spectra. In addition, a model is proposed to describe the intensity correction for the saturation and self-absorption effects. The energy and angular dependences are well explained by including such saturation effect. It also show that high energy loss features are influenced less by the saturation effect, which indicates that normalizing to the fluorescence feature could be a good approach to discuss the intensity competition. Although some discrepancies remain in the final simulations, the results show that the angular dependent $2p3d$ RIXS can provide deeper understanding on the fundamental properties of strongly correlated oxide materials.

The experimental geometry provides not only symmetry selectivity but also momentum selectivity. In chapter 5, I have studied the momentum dependent $2p3d$ RIXS of LaCoO_3 at 20K. Sizable dispersions of the intermediate-spin excited state ($^3T_{1g}$) were observed. The experimental data match well with the theoretical interpretation in the experimentally accessible part of the Brillouin zone and their extrapolation points to an important role of intermediate-spin excitations for the low-energy physics of the material. The results show that LaCoO_3 should not be viewed as a static collection of ions in particular atomic states, but rather as a gas of mobile bosonic excitons (intermediate-spin excitations) above vacuum (low-spin ground state). The high-spin states play the role of strongly bound and essentially immobile biexcitons. This picture provides a natural explanation why the spin-state order accompanied by Co-O bond-length disproportionation is not

observed in LaCoO_3 despite the low-energy of high-spin excitations.

In the chapter 6, I investigated the $2p3d$ RIXS spectra of the mixed-valence oxides Co_3O_4 and $(\text{Pr}_{0.925}\text{Y}_{0.075})_{0.7}\text{Ca}_{0.3}\text{CoO}_3$. The chemical site selectivity of $2p3d$ RIXS provides the ability to emphase the different covalent ions in the mixed-valence materials. For Co_3O_4 , a 4A_1 to 4T_2 excitation of the tetrahedral Co^{2+} site at 0.5 eV is clearly observed beyond the discriminative power of traditional optical absorptions. Guided by the cluster calculations, the ground state electronic structure of the Co^{2+} ions and Co^{3+} ions are once confirmed as high-spin ${}^4A_1(T_d)$ and low-spin ${}^1A_{1g}(O_h)$ states in the Co_3O_4 . The spectra also suggest that both of the Co^{2+} and Co^{3+} sites are hybridized strongly to the ligands. By selecting the characteristic features of each configuration, the partial fluorescence yield absorption spectra give the ability to differentiate the chemical sites. For the $(\text{Pr}_{0.925}\text{Y}_{0.075})_{0.7}\text{Ca}_{0.3}\text{CoO}_3$, I presented the temperature dependent Co $2p3d$ RIXS results on the polycrystalline sample. Below the transition temperature, a mixed state of low-spin, intermediate-spin, and high-spin states is presented. Particularly the contribution from the low-spin state is much less the general agreements. As the temperature increases, a higher intermediate-spin state contribution is found. It indicates the insulator-metal transition of the $(\text{Pr}_{0.925}\text{Y}_{0.075})_{0.7}\text{Ca}_{0.3}\text{CoO}_3$ sample strong correlates with a spin-state transition characterized as the low-spin/high-spin to intermediate-spin/intermediate-spin transition.

From all different $2p3d$ RIXS measurements, I have shown that $2p3d$ RIXS can reveal the electronic structure as well as the complex interactions. $2p3d$ RIXS measurements can also probe the hybridization an-isotropy and the bonding type [11, 251]. It is able to discuss the competition between the metal-to-metal (MM) and metal-to-ligand (ML) charge transfer including their magnetic properties of advance materials. These charge transfer and spin interactions play an important role in multilayered thin films, for example, the exchange bias in $\text{LaNiO}_3/\text{LaMnO}_3$ superlattices [264] or charge transfer in the isopolar $\text{LaTiO}_3/\text{LaFeO}_3$ interface [265]. In addition, the $2p3d$ RIXS might be able to probe the paramagnons of hematite ($\alpha\text{-Fe}_2\text{O}_3$). The high-energy terms (intra-atomic interactions and octahedral crystal field) determine the 6A_1 high-spin ground state. This ground state is potentially affected by $3d$ spin-orbit coupling, symmetry distortions and inter-atomic exchange interactions. The 6A_1 ground state however cannot be affected by the first two interactions, making it solely dependent on the inter-atomic exchange yielding magnon excitations. This situation is similar to the $3d^8$ ground state in NiO [2, 248]. The magnon excitations can couple to vibrations, making the q-dependent study of $2p3d$ RIXS in high-spin iron(III) systems sensitive to the dis-

persion of phonon-magnon excitations.

The power of RIXS has caught much attention and the experimental resolution is much improved from ~ 500 meV to ~ 20 meV with high brightness^[25, 266–268]. More efficient instruments with good resolution offer great potential to look into the low energy phonon excitations, spin-orbital coupling, spin flip excitations and orbital excitations, which can reveal the competition induced by charge, spin, and orbital interactions in advanced strongly correlated materials. Besides that, many new measurements are widely available in the future, e.g. mono-layer specimen measurements^[269], emitted beam polarization analysis^[269], three dimensional dispersion^[270], chemical interactions^[271, 272] and ultra-fast time resolved experiments^[273–275]. Through different experimental approaches, RIXS can look deeper into the time and spatial dependence of interactions. In order to interpret the new findings, many simulating approaches are also proposed to bridge the gap between the cluster multiplet calculation and the single electron excitation *ab initio* calculations^[202, 251, 276–279]. Guided by the theoretical predictions and simulations, more exciting issues of transition metal oxides can be resolved using RIXS.

Nederlandse Samenvatting

Dit proefschrift richt zich op de studie van kobalthoudende verbindingen en in het bijzonder van kobaltoxiden, met resonante inelastische röntgenverstrooiing (in het Engels Resonant Inelastic X-ray Scattering, RIXS). Ik heb verschillende aspecten van de elektronische en magnetische structuur van kobaltoxiden bestudeerd, inclusief ladingsoverdracht- en hybridisatie-effecten, de aard van de concurrerende spintoestanden, het substraatgeïnduceerde spanningseffect in dunne oxidefilms, excitondispersie en verschijnselen omtrent gemengde valentie. Deze effecten zijn bestudeerd met Co $2p3d$ RIXS-metingen die worden toegepast op binnaire kobaltoxiden, kobaltperovskieten, kobalthalogeniden en kobaltsulfiden. Om de hoge resolutie $2p3d$ RIXS-gegevens te interpreteren, heb ik een aantal theoretische methoden gebruikt die gebaseerd zijn op kristalveldmultipletmodellen met ladingsoverdracht.

In hoofdstuk 2 besprak ik de ligand-metaalhybridisatie en de elektrontransporteigenschappen van kobaltsulfiden en -halogeniden. $2p3d$ RIXS-spectra kunnen nauwkeurige waarden geven van de ladingsoverdrachtsenergie Δ en de kristalveldparameter $10Dq$, waarbij de kristalveldparameter wordt gesplitst in ionische bijdragen en ladingsoverdrachtbijdragen. Om de experimenten te vergelijken met de simulatieresultaten van de clusterberekeningen, zijn er beperkingen nodig om het aantal parameters te verminderen. Ik heb aangetoond dat de extra kristalveldenergie die wordt veroorzaakt door het ladingsoverdrachtseffect bij benadering lineair is met Δ . Daarnaast worden de L_2 -edge RIXS-spectra geanalyseerd met betrekking tot de geïntegreerde intensiteitsverhouding tussen resonante ($2p_{1/2}3d$) en niet-resonante ($2p_{3/2}3d$) röntgenemissies. De verhoudingen zijn respectievelijk ~ 0.55 , ~ 1.06 , ~ 1.22 en ~ 1.71 voor CoF_2 , CoCl_2 , CoBr_2 en CoS . Deze getallen laten zien dat het Coster-Kronig-kanaal sterker is in CoS en ik concludeerde dat de verhouding tussen resonant en niet-resonant verval een potentieel hulpmiddel is om de effecten van elektronlocalisatie te meten.

Hoofdstuk 3 presenteert de polarisatie-afhankelijke $2p3d$ RIXS-spectra van gespannen en ongespannen LaCoO_3 . Door de polarisatieafhankelijkheid van spec-

tra te bestuderen, kunnen de ladings-, spin- en orbitaalkenmerken van de toestanden worden gevonden. Ik vergeleek de experimentele resultaten met de simulatie in een benadering met een vast volume. Dit model wordt voorgesteld om het aantal empirische vrijheidsgraden te beperken, waardoor de symmetrie-eigenschap behouden blijft en een systematische discussie kan plaatsvinden. Op basis van de gepolariseerde analyse van inkomende röntgenfotonen, leerde ik dat de Co^{3+} ionen worden gedomineerd door de $^1A_{1g}(O_h)$ toestand in LaCoO_3 éénkristal. Daarnaast dragen $^5B_{2g}(D_{4h})$ en $^5E_g(D_{4h})$ toestanden bij aan de grondtoestand in de films met trek- en drukspanningen van LaCoO_3 op respectievelijk SrTiO_3 en LaAlO_3 . Hieruit blijkt dat $2p3d$ RIXS in staat is om het toestandsmengsel te onderscheiden door het polarisatie-afhankelijke gedrag van grondtoestand en aangeslagen toestand. De overeenkomst tussen simulaties en experimenten suggereert dat de Co^{3+} hoge-spin toestand de trigger kan zijn van ferromagnetische orde op lange afstand vanwege het mogelijke bestaan van quantum-chemische gemengde spintoestanden.

Bovendien demonstreerde ik in hoofdstuk 4 de hoekafhankelijke analyse van de $2p3d$ RIXS van de lage-spin $^1A_{1g}(O_h)$ en hoge-spin $^5B_{2g}(D_{4h})$ grondtoestanden. De polarisatieafhankelijkheid wordt niet alleen bepaald door het verschil tussen twee orthogonale lineair gepolariseerde invallende bundels maar ook beïnvloed door de experimentele geometrie. Een opmerkelijke consequentie is dat de isotrope lage-spin $^1A_{1g}(O_h)$ grondtoestand hoekafhankelijke $2p3d$ RIXS-spectra laat zien, in tegenstelling tot de $2p$ XAS-spectra, waar hoekafhankelijkheid afwezig is. Daarnaast wordt een model voorgesteld om de intensiteitscorrectie voor het verzadigings- en zelfabsorptie-effect te beschrijven. De energie- en hoekafhankelijkheden worden goed verklaard door het opnemen van een dergelijk verzadigingseffect. Het laat ook zien dat hoog-energieverlies-banden in het RIXS spectrum minder worden beïnvloed door het verzadigingseffect, wat aangeeft dat normaliseren op de fluorescentiekenmerk een goede benadering zou kunnen zijn om de intensiteitsratios te bespreken. Hoewel sommige verschillen blijven bestaan in de uiteindelijke simulaties, tonen de resultaten aan dat de hoekafhankelijke $2p3d$ RIXS een dieper inzicht kan verschaffen in de fundamentele eigenschappen van sterk gecorreleerde oxidematerialen.

De experimentele geometrie biedt niet alleen symmetrieselectiviteit maar ook impulsselectiviteit. In hoofdstuk 5 heb ik de impulsafhankelijkheid van $2p3d$ RIXS van LaCoO_3 bij 20K bestudeerd. Aanzienlijke dispersies van de aangeslagen toestand met intermediaire-spin ($^3T_{1g}$) werden waargenomen. De experimentele gegevens komen goed overeen met de theoretische interpretatie in het experimenteel toegankelijke deel van de Brillouin-zone en hun extrapolatie wijst naar

een belangrijke rol van intermediaire-spin excitaties voor de laag-energetische fysica van het materiaal. De resultaten laten zien dat LaCoO_3 niet moet worden gezien als een statische verzameling ionen in bepaalde atomaire toestanden maar eerder als een gas van mobiele bosonische excitonen (intermediaire-spin excitaties) boven vacuüm (lage-spin grondtoestand). De hoge-spin toestanden spelen de rol van sterk gebonden en vrijwel onbeweeglijke bi-excitonen. Deze beschrijving verklaart waarom de spintoestanderde met de daarmee geassocieerde Co-O bindingslengtedisproportionering niet wordt waargenomen in LaCoO_3 , ondanks de lage energie van hoge-spin excitaties.

In hoofdstuk 6 heb ik de $2p3d$ RIXS spectra van de gemengde-valentie oxides Co_3O_4 en $(\text{Pr}_{0.925}\text{Y}_{0.075})_{0.7}\text{Ca}_{0.3}\text{CoO}_3$ onderzocht. De chemische plaatsselectiviteit van $2p3d$ RIXS biedt de mogelijkheid om de verschillende covalente ionen in materialen met gemengde valentie te volgen. Voor Co_3O_4 wordt duidelijk een ${}^4\text{A}_1$ naar ${}^4\text{T}_2$ overgang voor de tetrahedrale Co^{2+} bij 0.5 eV waargenomen, die buiten de resolutie van traditionele optische absorptiespectroscopie ligt. Op basis van clusterberekeningen wordt de elektronische structuur van de grondtoestand van de Co^{2+} ionen en Co^{3+} ionen in Co_3O_4 bevestigd als respectievelijk hoge-spin ${}^4\text{A}_{1g}(\text{T}_d)$ en lage-spin ${}^1\text{A}_{1g}(\text{O}_h)$ toestanden. De spectra suggereren ook dat zowel Co^{2+} als Co^{3+} sterk gehybridiseerd zijn met de liganden. Door het selecteren van de karakteristieke kenmerken van elke configuratie, geven de partiële fluorescentieopbrengstabsorptiespectra de mogelijkheid om de chemische sites te differentiëren. Voor $(\text{Pr}_{0.925}\text{Y}_{0.075})_{0.7}\text{Ca}_{0.3}\text{CoO}_3$ presenteerde ik de temperatuurafhankelijke Co $2p3d$ RIXS-resultaten. Onder de overgangstemperatuur wordt een gemengde toestand van lage-spin, intermediaire-spin en hoge-spin toestanden gepresenteerd. Met name de bijdrage van de lage-spin toestand is veel minder dan algemeen aangenomen. Naarmate de temperatuur toeneemt, wordt er meer intermediaire-spin toestand gevonden. Dit geeft aan dat de isolator-metaalovergang aan van $(\text{Pr}_{0.925}\text{Y}_{0.075})_{0.7}\text{Ca}_{0.3}\text{CoO}_3$ sterk correleert met een spin-toestands-overgang gekenmerkt door de overgang van lage-spin/hoge-spin naar intermediaire-spin/intermediaire-spin.

Uit verschillende $2p3d$ RIXS-metingen, liet ik zien dat $2p3d$ RIXS zowel de elektronische structuur als de complexe interacties kan onthullen. $2p3d$ RIXS-metingen kunnen ook hybridisatie-anisotropie en het bindingstype aantonen. De techniek is in staat om de verhouding tussen de metaal-op-metaal (MM) en metaal-naar-ligand (ML) ladingsoverdracht te bepalen, inclusief de magnetische eigenschappen van geavanceerde materialen. Deze ladingsoverdracht en spininteracties spelen een belangrijke rol in dunne films met meerdere lagen, bijvoorbeeld de uitwisselingsbias in $\text{LaNiO}_3/\text{LaMnO}_3$ superlattices of ladingsoverdracht in het

isopolaire grensvlak tussen LaTiO_3 en LaFeO_3 ^[265]. Bovendien kan $2p3d$ RIXS mogelijk de paramagnons van hematiet ($\alpha\text{-Fe}_2\text{O}_3$) onderzoeken. De hoogenergetische termen (intra-atomaire interacties en octaëdrische kristalvelden) bepalen de 6A_1 grondtoestand. Deze grondtoestand wordt mogelijk beïnvloed door $3d$ spin-baankoppeling, symmetrievervormingen en inter-atomaire uitwisselingsinteracties. De grondtoestand 6A_1 kan echter niet beïnvloed worden door de eerste twee interacties, waardoor deze alleen afhankelijk is van de inter-atomaire uitwisseling die magnonexcitatie oplevert. Deze situatie is vergelijkbaar met de $3d^8$ grondtoestand van NiO ^[248]. De magnonexcitatie kunnen aan trillingen worden gekoppeld, waardoor de q -afhankelijke studie van $2p3d$ RIXS in systemen met ijzer(III) in de hoge-spin toestand gevoelig is voor de verspreiding van fononmagnon-excitatie.

De kracht van RIXS heeft veel aandacht gekregen en de experimentele resolutie is aanzienlijk verbeterd van ~ 500 meV tot ~ 20 meV met hoge helderheid^[25, 266–268]. Efficiëntere instrumenten met een goede resolutie bieden een groot potentieel om te kijken naar de lage-energie-fonon-excitatie, spin-baankoppeling, spin-flip-excitatie en orbitale excitatie, die de concurrentie kunnen onthullen die wordt geïnduceerd door ladings-, spin- en orbitaalinteracties. Ook zullen er veel geavanceerdere metingen beschikbaar zijn in de toekomst, b.v. enkellaagse monstermetingen^[269], röntgenemissiepolarisatieanalyse^[269], dispersie in drie dimensies^[270], chemische interacties^[271, 272] en ultrasnelle tijd-opgeloste experimenten^[273–275]. Via verschillende experimentele benaderingen kan RIXS dieper ingaan op de tijdsafhankelijkheid en ruimtelijke afhankelijkheid van interacties. Om de nieuwe bevindingen te interpreteren, worden verschillende simulatiemethodes voorgesteld om de kloof tussen de cluster-multiplet-berekening en de ab initio éénelektronexcitatiemodellen te overbruggen^[202, 251, 276–279]. Aan de hand van de theoretische voorspellingen en simulaties, kunnen spannendere problemen van overgangsmetaaloxiden worden opgelost met behulp van RIXS.

Acknowledgements

This PhD thesis cannot be accomplished without many helps and supports from dozens of people. First of all, I wish to give my gratefulness to my promoter Prof. Frank de Groot. It is my great pleasure to work under your supervision. Thank you for guiding me on my researching topic. You have also helped me improve my language skill, introduced many nice collaborators, and shared the new science information. In addition, I would like to thank you for sharing many good plans and the visiting spots for the holidays. I always remember that you introduce the masterpiece “potato eaters” from Vincent van Gogh in the first day we met, where a person in the painting has the same family name as you.

I will never forget to show my thanks to all the members in Frank’s Group, the Rayman team. Due to many high-intense and time-consuming of the synchrotron and conference trips, we are close connected to each other. I enjoy spending the time with you together very much. All these memories will be treasured in my heart. Matti van Schooneveld, thank you for teaching me about making a good article structure. Mario Delgado-Jaime, you are really helping a lot on the data analyzing. I have learned a lot from you about how to treat the spectra properly. You are also the most generous chef in our group. I very enjoyed the meal you shared with us. Myrtille Hunault, thank you for suggestions and discussions about numerous different theoretical simulation approaches. It is indeed helpful for the general understanding. Mahnaz Ghiasi, thanks for the comments about the VISA application and job hunting. With your suggestions, many practical issues passed easily. Yohei Uemura, although you are the latest colleague I met in the group, I would like to thank you for your kindness and consideration. You always brought good rice back from Japan for me. Piter Miedema, you have already finished before I came but you always helped a lot when we visited BESSY. I also appreciate on your accompany in the many trips. I will not forgot we shell the budget together at a souvenir shop in Oxford. Boyang Liu, you are really my comforter in the group although you did nothing. But it was great to have friend abroad who can chat and discuss in the common mother tongue is great. In many days, we

ACKNOWLEDGEMENTS

discussed a lot in not only science but also the experience in the Netherlands. A lot of cheerful memories were created with you. Patric Zimmermann, you always suggests us that try to avoid using the social media through the internet. I will keep it in mind. Mustafa Al Samarai, I can remember that you helped me a lot in the first week of my PhD. There were many practical documents to be treated. But with you help, all the issues were done quickly, such as applying the bank account and the health insurance. I also thank you for introducing the environment of Utrecht university and Utrecht city to me. Marte van der Linden, thank you for becoming an accomplice of eating chocolate in the office. You also gave many good advice on the presenting skill. I indeed learned a lot from you. I would also like to give my big thanks for your help on designing my thesis cover, you have successfully bring my abstract idea into concrete drawing. Hebatalla Elnaggar, I want to thank you for many supports on the simulations and discussions. With your helps, the works became more understandable and valuable. Ties Haarman, I appreciate your transparent Matlab code for analyzing the date. I also thank you for your interests in visiting my home town, it was my pleasure to introduce Tainan to you. Ahmed Ismail, I would like to thank you sharing a lot of the fantastic researching ideas. Federica Frati, many thanks to you about the participation in many of my experiments during your first year of PhD. I know it is quite tough to work in the synchrotron with only two team members. But with your supports, many works were done smoothly. Many thanks should be given to our technicians and secretaries in the inorganic chemistry and catalysis group as well. Your helps on the practical problems for the experiments and the official documents reduced a lot of complex tasks for me.

For the works, I should share also the credits to my collaborators. With your generous supports, many topics in the thesis became more successful. Prof. Dijing Huang, thank you and your group members Dr. Hsiao-Yu Huang, Dr. Jun Okamoto, and Dr. Wen-Bin Wu. You helped a lot for the resonant inelastic X-ray scattering measurements in Taiwan Light Source. Many valuable discussions were made during the experiments and conferences with you. Thanks for the group of Prof. Stefan Schuppeler in ANKA, the group of Prof. Thorsten Schmitt in SLS, the group of Prof. Nick Brookes in ESRF. You have provided many experimental supports in the synchrotron as well. Thank you for all the kind supports which led the experiments went smoothly without any troubles. The works also rely on many good sample providers. I want to thank Prof. Gertjan Koster and Jaap Geessinck for your support on fabricating many LaCoO_3 films in different strains and appreciate Yorick Birkholzer's helps on characterized the films. Also many thanks for Dr. Zdeněk Jirák, Prof. Hiroyuki Fujishiro and Dr. Keisuke Tomiyasu

provided their good quality $(\text{Pr}_{0.925}\text{Y}_{0.075})_{0.7}\text{Ca}_{0.3}\text{CoO}_3$ compound and LaCoO_3 single crystal. Prof. Chao-Hung Du, thank you for sending the student Yu-Hui Liang to help me characterized the orientation of samples. Furthermore, it is my pleasure to work with many theoreticians as Prof. Jan Kuneš, Dr. Atsushi Hariki, Dr. Andrii Sotnikov, and Dr. Robert J. Green. Many fantastic ideas and a lot of fundamental knowledge were enlightened by you. The contents of the thesis were improved under the discussion with you.

In the end, I want to give the greatest thanks to God that He gave opportunity for me to pursuit the Doctor degree in Utrecht. Before 2014, I never expected that I am able to study in the Netherlands. To live and to work abroad indeed is a great challenge for me because of the language skill and the culture biases. This is one of my big step in lifelong learning. Fortunately, the challenge becomes easier with all the accompanies from the friends I met. Many thanks to the people who are not mentioned and to you who is reading this thesis.

ACKNOWLEDGEMENTS

List of Publications

First Author Publications

R.-P. Wang, J. Geessinck, H. Elnaggar, K. Tomiyasu, J. Okamoto, B. Liu, C.-H. Du, D. J. Huang, G. Koster, and F. M. F. de Groot, “*Angular Dependence and Self-absorption of 2p3d RIXS in LaCoO₃*”, in preparation

R.-P. Wang, T. Haarman, B. Liu, A. Hariki, J. Okamoto, H. Y. Huang, W. B. Wu, D. J. Huang, S. Schuppler, F. M. F. de Groot, “*The electronic structure of the Co²⁺ and Co³⁺ ions in Co₃O₄ using 2p3d RIXS*”, in preparation

R.-P. Wang, J. Geessinck, H. Elnaggar, K. Tomiyasu, J. Okamoto, B. Liu, C.-H. Du, D. J. Huang, G. Koster, and F. M. F. de Groot, “*Low energy orbital excitations in strained LaCoO₃ flms*”, submitted to Phys. Rev. B

R.-P. Wang, A. Hariki, A. Sotnikov, F. Frati, J. Okamoto, H. Y. Huang, A. Singh, D. J. Huang, K. Tomiyasu, C. H. Du, J. Kuneš, and F. M. F. de Groot, “*Excitonic dispersion of the intermediate spin state in LaCoO₃ revealed by resonant inelastic x-ray scattering*”, **Phys. Rev. B** **98**,035149 (2018)

R.-P. Wang, B. Liu, R. J. Green, M. U. Delgado-Jaime, M. Ghiasi, T. Schmitt, M. M. van Schooneveld, and F. M. F. de Groot, “*Charge-transfer analysis of 2p3d resonant inelastic Xray scattering of cobalt sulfide and halides*”, **J. Phys. Chem. C** **121**, 24919 (2017)

Other Publications

H. Elnaggar, R.-P. Wang, S. Lafuerza, E. Paris, A. C. Komarek, H. Guo, Y. Tseng, D. McNally, F. Frati, M. W. Haverkort, M. Sikora, T. Schmitt, and F. M. F. de Groot, “*Trimeron correlations above the Verwey temperature in Fe₃O₄?*”, submitted to Phys. Rev. Lett.

A. Singh, H. Y. Huang, Y. Y. Chin, Y. F. Liao, T. C. Huang, J. Okamoto, W. B. Wu, H. J. Lin, K. D. Tsuei, R.-P. Wang, F. M. F. de Groot, C. N. Kuo, H. F. Liu, C. S. Lue, C. T. Chen, D. J. Huang, and A. Chainani, “*Electronic structure investigation of a charge density wave coupled to a metal-to-metal transition in Ce₃Co₄Sn₁₃*”, **Phys. Rev. B** **98**, 235136 (2018)

B. Liu, E. N. Glass, R.-P. Wang, Y. Cui, Y. Harada, D. J. Huang, S. Schuppler, C. L. Hill,

and F. M. F. de Groot, “Cobalt-to-vanadium charge transfer in polyoxometalate water oxidation catalysts revealed by 2p3d resonant inelastic X-ray scattering”, **Phys. Chem. Chem. Phys.** **20**, 4554 (2018)

K. Tomiyasu, J. Okamoto, H. Y. Huang, Z. Y. Chen, E. P. Sinaga, W. B. Wu, Y. Y. Chu, A. Singh, R.-P. Wang, F. M. F. de Groot, A. Chainani, S. Ishihara, C. T. Chen, and D. J. Huang, “Coulomb Correlations Intertwined with Spin and Orbital Excitations in LaCoO_3 ”, **Phys. Rev. Lett.** **119**, 196402 (2017)

B. Liu, C. Piamonteze, M. U. Delgado-Jaime, R.-P. Wang, J. Heidler, J. Dreiser, R. Chopdekar, F. Nolting, and F. M. F. de Groot, “Sum rule distortions in fluorescence-yield x-ray magnetic circular dichroism”, **Phys. Rev. B** **96**, 054446 (2017)

H. Y. Huang, Z. Y. Chen, R.-P. Wang, F. M. F. de Groot, W. B. Wu, J. Okamoto, A. Chainani, A. Singh, Z.-Y. Li, J.-S. Zhou, H.-T. Jeng, G. Y. Guo, J.-G. Park, L. H. Tjeng, C. T. Chen, and D. J. Huang, “Jahn-Teller distortion driven magnetic polarons in magnetite”, **Nat. Commun.** **8**, 15929 (2017)

M. Ghiasi, M. U. Delgado-Jaime, A. Malekzadeh, R.-P. Wang, P. S. Miedema, M. Beye, and F. M. F. de Groot, “Mn and Co charge and spin evolutions in $\text{LaMn}_{1-x}\text{Co}_x\text{O}_3$ nanoparticles”, **J. Phys. Chem. C** **120**, 8167 (2016)

B. Liu, R.-P. Wang, E. N. Glass, C. L. Hill, T. Cuk, J. Okamoto, D. J. Huang, M. M. van Schooneveld, and F. M. F. de Groot, “Distorted tetrahedral Co^{II} in $\text{K}_5\text{H}[\text{CoW}_{12}\text{O}_{40}]_x\text{H}_2\text{O}$ probed by 2p3d resonant inelastic X-ray scattering”, **Inorg. Chem.** **55**, 10152 (2016)

Conference Contributions

Resonant inelastic X-ray scattering of LaCoO_3 single crystal and films (Poster)

- 17th International Conference on X-ray Absorption Fine Structure (2018)
- 10th International Conference on Inelastic X-ray Scattering (2017)
- Towards Oxide-Based Electronics (2017 spring)

Charge transfer multiplet analysis of CoF_2 , CoCl_2 , CoBr_2 and CoS_x 2p3d RIXS spectra (Oral)

- 39th International conference on Vacuum Ultraviolet and X-ray Physics (2017)
- EUSpec Winter School on core level spectroscopies (2016)

About the Author

Ru-Pan Wang was born on September 10th, 1988 in Tainan, Taiwan. He grew up with great interest in science and started his bachelor in the autumn of 2006 in the Department of Physics in National Tsing Hua University, Taiwan. He continued his master degree in physics and focused on the research of resonant X-ray scattering (RXS) under the supervision of Prof. Dijing Huang. After the military service, he started his long journey in resonant inelastic X-ray scattering (RIXS) with Prof. Huang and later joined the group of Prof. Frank de Groot for pursuing his PhD degree. He focused on the research about the structure/charge ordering as well as the electronic configurations using RIXS and RXS in combination with quantum many body calculations.

BIBLIOGRAPHY

Bibliography

- [1] L. J. P. Ament, M. van Veenendaal, T. P. Devereaux, J. P. Hill, and J. van den Brink, *Rev. Mod. Phys.* **83**, 705 (2011).
- [2] G. Ghiringhelli, A. Piazzalunga, C. Dallera, T. Schmitt, V. N. Strocov, J. Schlappa, L. Patthey, X. Wang, H. Berger, and M. Grioni, *Phys. Rev. Lett.* **102**, 027401 (2009).
- [3] M. Moretti Sala, V. Bisogni, C. Aruta, G. Balestrino, H. Berger, N. B. Brookes, G. M. de Luca, D. D. Castro, M. Grioni, M. Guarise, et al., *New J. Phys.* **13**, 043026 (2011).
- [4] M. M. van Schooneveld, R. Kurian, A. Juhin, K. Zhou, J. Schlappa, V. N. Strocov, T. Schmitt, and F. M. F. de Groot, *J. Phys. Chem. C* **116**, 15218 (2012).
- [5] M. Magnuson, S. Butorin, J.-H. Guo, and J. Nordgren, *Phys. Rev. B* **65**, 205106 (2002).
- [6] H. Y. Huang, Z. Y. Chen, R.-P. Wang, F. M. F. de Groot, W. B. Wu, J. Okamoto, A. Chainani, A. Singh, Z.-Y. Li, J. S. Zhou, et al., *Nat. Commun.* **8**, 15929 (2017).
- [7] B. Liu, R.-P. Wang, E. N. Glass, C. L. Hill, T. Cuk, J. Okamoto, D. J. Huang, M. M. van Schooneveld, and F. M. F. de Groot, *Inorg. Chem.* **55**, 10152 (2016).
- [8] S. G. Chiuzbăian, T. Schmitt, M. Matsubara, A. Kotani, G. Ghiringhelli, C. Dallera, A. Tagliaferri, L. Braicovich, V. Scagnoli, N. B. Brookes, et al., *Phys. Rev. B* **78**, 245102 (2008).
- [9] S. M. Butorin, J.-H. Guo, M. Magnuson, and J. Nordgren, *Phys. Rev. B* **55**, 4242 (1997).
- [10] A. Agui, T. Uozumi, M. Mizumaki, and T. Käämbre, *Phys. Rev. B* **79**, 092402 (2009).

- [11] G. Fabbris, D. Meyers, J. Okamoto, J. Pellicciari, A. S. Disa, Y. Huang, Z.-Y. Chen, W. B. Wu, C. T. Chen, S. Ismail-Beigi, et al., *Phys. Rev. Lett.* **117**, 147401 (2016).
- [12] J. Schlappa, T. Schmitt, F. Vernay, V. N. Strocov, V. Ilakovac, B. Thielemann, H. M. Rønnow, S. Vanishri, A. Piazzalunga, X. Wang, et al., *Phys. Rev. Lett.* **103**, 047401 (2009).
- [13] L. Braicovich, L. J. P. Ament, V. Bisogni, F. Forte, C. Aruta, G. Balestrino, N. B. Brookes, G. M. De Luca, P. G. Medaglia, F. M. Granozio, et al., *Phys. Rev. Lett.* **102**, 167401 (2009).
- [14] L. Braicovich, J. van den Brink, V. Bisogni, M. Moretti Sala, L. J. P. Ament, N. B. Brookes, G. M. De Luca, M. Salluzzo, T. Schmitt, V. N. Strocov, et al., *Phys. Rev. Lett.* **104**, 077002 (2010).
- [15] H. Y. Huang, C. J. Jia, Z. Y. Chen, K. Wohlfeld, B. Moritz, T. P. Devereaux, W. B. Wu, J. Okamoto, W. S. Lee, M. Hashimoto, et al., *Sci. Rep.* **6**, 19657 (2016).
- [16] G. Fabbris, D. Meyers, L. Xu, V. M. Katukuri, L. Hozoi, X. Liu, Z.-Y. Chen, J. Okamoto, T. Schmitt, A. Uldry, et al., *Phys. Rev. Lett.* **118**, 156402 (2017).
- [17] A. Pietzsch, F. Hennies, P. S. Miedema, B. Kennedy, J. Schlappa, T. Schmitt, V. N. Strocov, and A. Föhlisch, *Phys. Rev. Lett.* **114**, 088302 (2015).
- [18] S. Moser, S. Fatale, P. Krüger, H. Berger, P. Bugnon, A. Magrez, H. Niwa, J. Miyawaki, Y. Harada, and M. Gioni, *Phys. Rev. Lett.* **115**, 096404 (2015).
- [19] H. A. Kramers and W. Heisenberg, *Z. Phys.* **31**, 681 (1925).
- [20] M. W. Haverkort, *Phys. Rev. Lett.* **105**, 167404 (2010).
- [21] Y. Y. Peng, G. Dellea, M. Minola, M. Conni, A. Amorese, D. Di Castro, G. M. De Luca, K. Kummer, M. Salluzzo, X. Sun, et al., *Nat. Phys.* **13**, 1201 (2017).
- [22] Y. Lu, D. Betto, K. Fürsich, H. Suzuki, H.-H. Kim, G. Cristiani, G. Logvenov, N. B. Brookes, E. Benckiser, M. W. Haverkort, et al., *Phys. Rev. X* **8**, 031014 (2018).

- [23] H. S. Fung, C. T. Chen, L. J. Huang, C. H. Chang, S. C. Chung, D. J. Wang, T. C. Tseng, and K. L. Tsang, *AIP Conference Proceedings* **705**, 655 (2004).
- [24] C. H. Lai, H. S. Fung, W. B. Wu, H. Y. Huang, H. W. Fu, S. W. Lin, S. W. Huang, C. C. Chiu, D. J. Wang, L. J. Huang, et al., *J. Synchrotron Rad.* **21**, 325 (2014).
- [25] D. J. Huang and C. T. Chen, *Synchrotron Radiation News* **31**, 3 (2018).
- [26] D. J. Griffiths, *Introduction to Quantum Mechanics* (Upper Saddle River, NJ : Pearson Prentice Hall, 2005).
- [27] J. C. Slater, *Phys. Rev.* **34**, 1293 (1929).
- [28] R. D. Cowan, *The Theory of Atomic Structure and Spectra* (University of California Press: Berkeley, CA, 1981).
- [29] F. de Groot and A. Kotani, *Core Level Spectroscopy of Solids* (CRC Press, 2008).
- [30] F. M. F. de Groot, J. C. Fuggle, B. T. Thole, and G. A. Sawatzky, *Phys. Rev. B* **42**, 5459 (1990).
- [31] A. Uldry, F. Vernay, and B. Delley, *Phys. Rev. B* **85**, 125133 (2012).
- [32] M. van Veenendaal, *Phys. Rev. Lett.* **96**, 117404 (2006).
- [33] W. L. Roth, *Phys. Rev.* **110**, 1333 (1958).
- [34] H. P. Rooksby and N. C. Tombs, *Nature* **167**, 364 (1951).
- [35] La Blanchetais, C. H., *J. Phys. Radium* **12**, 765 (1951).
- [36] M. D. Reichtin and B. L. Averbach, *Phys. Rev. Lett.* **26**, 1483 (1971).
- [37] P. S. Silinsky and M. S. Seehra, *Phys. Rev. B* **24**, 419 (1981).
- [38] J. P. Picard, G. Baud, J. P. Besse, and R. Chevalier, *J. Less Common. Met.* **75**, 99 (1980).
- [39] T. D. Sparks, A. Gurlo, M. W. Gaultois, and D. R. Clarke, *Phys. Rev. B* **98**, 024108 (2018).
- [40] W. H. Bragg, *Nature* **95**, 561 (1915).

- [41] W. H. Bragg, *Philos. Mag.* **30**, 305 (1915).
- [42] W. H. Bragg and G. B. Brown, *Proc. Royal Soc. Lond.* **110**, 34 (1926).
- [43] J. W. D. Martens, W. L. Peeters, H. M. van Noort, and M. Erman, *J. Phys. Chem. Solids* **46**, 411 (1985).
- [44] C. A. F. Vaz, E. I. Altman, and V. E. Henrich, *Phys. Rev. B* **81**, 104428 (2010).
- [45] N. Du, H. Zhang, B. Chen, J. Wu, X. Ma, Z. Liu, Y. Zhang, D. Yang, X. Huang, and J. Tu, *Adv. Mater.* **19**, 4505 (2007).
- [46] R. N. Singh, D. Mishra, Anindita, A. S. K. Sinha, and A. Singh, *Electrochem. Commun.* **9**, 1369 (2007).
- [47] A. J. Esswein, M. J. McMurdo, P. N. Ross, A. T. Bell, and T. D. Tilley, *J. Phys. Chem. C* **113**, 15068 (2009).
- [48] F. Jiao and H. Frei, *Angew. Chem. Int. Ed.* **48**, 1841 (2009).
- [49] V. Artero, M. Chavarot-Kerlidou, and M. Fontecave, *Angew. Chem. Int. Ed.* **50**, 7238 (2011).
- [50] L. Xi, P. D. Tran, S. Y. Chiam, P. S. Bassi, W. F. Mak, H. K. Mulmudi, S. K. Batabyal, J. Barber, J. S. C. Loo, and L. H. Wong, *J. Phys. Chem. C* **116**, 13884 (2012).
- [51] X. Zhang, Y.-S. Chen, P. V. Kamat, and S. Ptasinska, *J. Phys. Chem. C* **122**, 13894 (2018).
- [52] W. Wang and J. Xu, *ACS Appl. Mater. Interfaces* **7**, 415 (2015).
- [53] I. D. Belova, Y. E. Roginskaya, R. R. Shifrina, S. G. Gagarin, Y. V. Plekhanov, and Y. N. Venevtsev, *Solid State Commun.* **47**, 577 (1983).
- [54] J. G. Cook and M. P. van der Meer, *Thin Solid Films* **144**, 65 (1986).
- [55] K. M. E. Miedzinska, B. R. Hollebone, and J. G. Cook, *J. Phys. Chem. Solids* **48**, 649 (1987).
- [56] X. Wang, X. Chen, L. Gao, H. Zheng, Z. Zhang, and Y. Qian, *J. Phys. Chem. B* **108**, 16401 (2004).
- [57] A. F. Lima, *J. Phys. Chem. Solids* **75**, 148 (2014).

- [58] D. L. Wood and J. P. Remeika, *J. Chem. Phys.* **46**, 3595 (1967).
- [59] N. Mironova, V. Skvortsova, and U. Ulmanis, *Solid State Commun.* **91**, 731 (1994).
- [60] W. L. Roth, *J. Phys. Chem. Solids* **25**, 1 (1964).
- [61] Y. Ikedo, J. Sugiyama, H. Nozaki, H. Itahara, J. H. Brewer, E. J. Ansaldo, G. D. Morris, D. Andreica, and A. Amato, *Phys. Rev. B* **75**, 054424 (2007).
- [62] A. M. Hibberd, H. Q. Doan, E. N. Glass, F. M. F. de Groot, C. L. Hill, and T. Cuk, *J. Phys. Chem. C* **119**, 4173 (2015).
- [63] M. M. van Schooneveld, R. W. Gosselink, T. M. Eggenhuisen, M. A. Samarai, C. Monney, K. J. Zhou, T. Schmitt, and F. M. F. de Groot, *Angew. Chem. Int. Ed.* **52**, 1170 (2013).
- [64] J. B. Goodenough, *J. Phys. Chem. Solid* **6**, 287 (1958).
- [65] P. M. Raccah and J. B. Goodenough, *Phys. Rev.* **155**, 932 (1967).
- [66] R. R. Heikes, R. C. Miller, and R. Mazelsky, *Physica* **30**, 1600 (1964).
- [67] V. G. Bhide, D. S. Rajoria, G. R. Rao, and C. N. R. Rao, *Phys. Rev. B* **6**, 1021 (1972).
- [68] S. Stølen, F. Grønvold, H. Brinks, T. Atake, and H. Mori, *Phys. Rev. B* **55**, 14103 (1997).
- [69] J. Baier, S. Jodlauk, M. Kriener, A. Reichl, C. Zobel, H. Kierspel, A. Freimuth, and T. Lorenz, *Phys. Rev. B* **71**, 014443 (2005).
- [70] S. Yamaguchi, Y. Okimoto, and Y. Tokura, *Phys. Rev. B* **54**, R11022 (1996).
- [71] N. Menyuk, K. Dwight, and P. M. Raccah, *J. Phys. Chem. Solids* **28**, 549 (1967).
- [72] K. Asai, P. Gehring, H. Chou, and G. Shirane, *Phys. Rev. B* **40**, 10982 (1989).
- [73] Y. Tokura, Y. Okimoto, S. Yamaguchi, H. Taniguchi, T. Kimura, and H. Takagi, *Phys. Rev. B* **58**, R1699 (1998).
- [74] Y. Tanabe and S. Sugano, *J. Phys. Soc. Jpn.* **9**, 766 (1954).

BIBLIOGRAPHY

- [75] M. Zhuang, W. Zhang, and N. Ming, *Phys. Rev. B* **57**, 10705 (1998).
- [76] S. Mukhopadhyay, M. W. Finnis, and N. M. Harrison, *Phys. Rev. B* **87**, 125132 (2013).
- [77] S. R. Barman and D. D. Sarma, *Phys. Rev. B* **49**, 13979 (1994).
- [78] K. Asai, O. Yokokura, N. Nishimori, H. Chou, J. M. Tranquada, G. Shirane, S. Higuchi, Y. Okajima, and K. Kohn, *Phys. Rev. B* **50**, 3025 (1994).
- [79] M. Abbate, J. C. Fuggle, A. Fujimori, L. H. Tjeng, C. T. Chen, R. Potze, G. A. Sawatzky, H. Eisaki, and S. Uchida, *Phys. Rev. B* **47**, 16124 (1993).
- [80] M. A. Korotin, S. Y. Ezhov, I. V. Solovyev, V. I. Anisimov, D. I. Khomskii, and G. A. Sawatzky, *Phys. Rev. B* **54**, 5309 (1996).
- [81] K. Knížek, P. Novák, and Z. Jirák, *Phys. Rev. B* **71**, 054420 (2005).
- [82] K. Asai, A. Yoneda, O. Yokokura, J. M. Tranquada, G. Shirane, and K. Kohn, *J. Phys. Soc. Jpn.* **67**, 290 (1998).
- [83] P. G. Radaelli and S.-W. Cheong, *Phys. Rev. B* **66**, 094408 (2002).
- [84] T. Saitoh, T. Mizokawa, A. Fujimori, M. Abbate, Y. Takeda, and M. Takano, *Phys. Rev. B* **55**, 4257 (1997).
- [85] S. Yamaguchi, Y. Okimoto, and Y. Tokura, *Phys. Rev. B* **55**, R8666 (1997).
- [86] C. Zobel, M. Kriener, D. Bruns, J. Baier, M. Grüninger, T. Lorenz, P. Reutler, and A. Revcolevschi, *Phys. Rev. B* **66**, 020402 (2002).
- [87] S. Noguchi, S. Kawamata, K. Okuda, H. Nojiri, and M. Motokawa, *Phys. Rev. B* **66**, 094404 (2002).
- [88] T. Vogt, J. A. Hriljac, N. C. Hyatt, and P. Woodward, *Phys. Rev. B* **67**, 140401 (2003).
- [89] G. Maris, Y. Ren, V. Volotchaev, C. Zobel, T. Lorenz, and T. T. M. Palstra, *Phys. Rev. B* **67**, 224423 (2003).
- [90] A. Ishikawa, J. Nohara, and S. Sugai, *Phys. Rev. Lett.* **93**, 136401 (2004).
- [91] Y. Kobayashi, T. S. Naing, M. Suzuki, M. Akimitsu, K. Asai, K. Yamada, J. Akimitsu, P. Manuel, J. M. Tranquada, and G. Shirane, *Phys. Rev. B* **72**, 174405 (2005).

- [92] K. Knížek, Z. Jirák, J. Hejtmánek, M. Veverka, M. Maryško, G. Maris, and T. T. Palstra, *Eur. Phys. J. B* **47**, 213 (2005).
- [93] Y. Kobayashi, T. S. Naing, M. Suzuki, M. Akimitsu, K. Asai, K. Yamada, J. Akimitsu, P. Manuel, J. M. Tranquada, and G. Shirane, *Physica B* **378**, 532 (2006).
- [94] M. Medarde, C. Dallera, M. Grioni, J. Voigt, A. Podlesnyak, E. Pomjakushina, K. Conder, T. Neisius, O. Tjernberg, and S. N. Barilo, *Phys. Rev. B* **73**, 054424 (2006).
- [95] Z. Ropka and R. J. Radwanski, *Phys. Rev. B* **67**, 172401 (2003).
- [96] A. Podlesnyak, S. Streule, J. Mesot, M. Medarde, E. Pomjakushina, K. Conder, A. Tanaka, M. W. Haverkort, and D. I. Khomskii, *Phys. Rev. Lett.* **97**, 247208 (2006).
- [97] M. W. Haverkort, Z. Hu, J. C. Cezar, T. Burnus, H. Hartmann, M. Reuther, C. Zobel, T. Lorenz, A. Tanaka, N. B. Brookes, et al., *Phys. Rev. Lett.* **97**, 176405 (2006).
- [98] G. Vankó, J. Rueff, A. Mattila, Z. Németh, and A. Shukla, *Phys. Rev. B* **73**, 024424 (2006).
- [99] D. P. Kozlenko, N. O. Golosova, Z. Jirák, L. S. Dubrovinsky, B. N. Savenko, M. G. Tucker, Y. Le Godec, and V. P. Glazkov, *Phys. Rev. B* **75**, 064422 (2007).
- [100] L. Craco and E. Müller-Hartmann, *Phys. Rev. B* **77**, 045130 (2008).
- [101] S. K. Pandey, A. Kumar, S. Patil, V. R. R. Medicherla, R. S. Singh, K. Maiti, D. Prabhakaran, A. T. Boothroyd, and A. V. Pimpale, *Phys. Rev. B* **77**, 045123 (2008).
- [102] S. K. Pandey, A. Kumar, S. Banik, A. K. Shukla, S. R. Barman, and A. V. Pimpale, *Phys. Rev. B* **77**, 113104 (2008).
- [103] K. Tomiyasu, J. Okamoto, H. Y. Huang, Z. Y. Chen, E. P. Sinaga, W. B. Wu, Y. Y. Chu, A. Singh, R.-P. Wang, F. M. F. de Groot, et al., *Phys. Rev. Lett.* **119**, 196402 (2017).
- [104] K. Knížek, Z. Jirák, J. Hejtmánek, and P. Novák, *J. Phys. Condens. Matter* **18**, 3285 (2006).

BIBLIOGRAPHY

- [105] K. Knížek, Z. Jirák, J. Hejtmánek, P. Henry, and G. André, *J. Appl. Phys.* **103**, 07B703 (2008).
- [106] K. Knížek, Z. Jirák, J. Hejtmánek, P. Novák, and W. Ku, *Phys. Rev. B* **79**, 014430 (2009).
- [107] J. Kuneš and V. Křápek, *Phys. Rev. Lett.* **106**, 256401 (2011).
- [108] W. C. Koehler and E. O. Wollan, *J. Phys. Chem. Solids.* **2**, 100 (1957).
- [109] K. Tomiyasu, T. Nomura, Y. Kobayashi, S. Ishihara, S. Ohira-Kawamura, and M. Kofu, arXiv (2018).
- [110] A. Doi, J. Fujioka, T. Fukuda, S. Tsutsui, D. Okuyama, Y. Taguchi, T. Arima, A. Q. R. Baron, and Y. Tokura, *Phys. Rev. B* **90**, 081109 (2014).
- [111] M. M. Altarawneh, G.-W. Chern, N. Harrison, C. D. Batista, A. Uchida, M. Jaime, D. G. Rickel, S. A. Crooker, C. H. Mielke, J. B. Betts, et al., *Phys. Rev. Lett.* **109**, 037201 (2012).
- [112] A. Ikeda, T. Nomura, Y. H. Matsuda, A. Matsuo, K. Kindo, and K. Sato, *Phys. Rev. B* **93**, 220401 (2016).
- [113] A. Sotnikov and J. Kuneš, *Sci. Rep.* **6**, 30510 (2016).
- [114] D. Fuchs, C. Pinta, T. Schwarz, P. Schweiss, P. Nagel, S. Schuppler, R. Schneider, M. Merz, G. Roth, and H. V. Löhneysen, *Phys. Rev. B* **75**, 144402 (2007).
- [115] D. Fuchs, E. Arac, C. Pinta, S. Schuppler, R. Schneider, and H. v. Löhneysen, *Phys. Rev. B* **77**, 014434 (2008).
- [116] J. Fujioka, Y. Yamasaki, H. Nakao, R. Kumai, Y. Murakami, M. Nakamura, M. Kawasaki, and Y. Tokura, *Phys. Rev. Lett.* **111**, 027206 (2013).
- [117] J. Fujioka, Y. Yamasaki, A. Doi, H. Nakao, R. Kumai, Y. Murakami, M. Nakamura, M. Kawasaki, T. Arima, and Y. Tokura, *Phys. Rev. B* **92**, 195115 (2015).
- [118] J. W. Freeland, J. X. Ma, and J. Shi, *Appl. Phys. Lett.* **93**, 212501 (2008).
- [119] Rivas-murias, B. and Lucas, I. and Jime, P., *Nano Lett.* **16**, 1736 (2016).
- [120] D. Meng, H. Guo, Z. Cui, C. Ma, J. Zhao, J. Lu, H. Xu, Z. Wang, X. Hu, Z. Fu, et al., *Proc. Natl. Acad. Sci.* **115**, 2873 (2018).

- [121] G. E. Sterbinsky, P. J. Ryan, J.-W. Kim, E. Karapetrova, J. X. Ma, J. Shi, and J. C. Woicik, *Phys. Rev. B* **85**, 020403 (2012).
- [122] K. Gupta and P. Mahadevan, *Phys. Rev. B* **79**, 020406 (2009).
- [123] H. Hsu, P. Blaha, and R. M. Wentzcovitch, *Phys. Rev. B* **85**, 140404 (2012).
- [124] V. V. Mehta, N. Biskup, C. Jenkins, E. Arenholz, M. Varela, and Y. Suzuki, *Phys. Rev. B* **91**, 144418 (2015).
- [125] Y. Yokoyama, Y. Yamasaki, M. Taguchi, Y. Hirata, K. Takubo, J. Miyawaki, Y. Harada, D. Asakura, J. Fujioka, M. Nakamura, et al., *Phys. Rev. Lett.* **120**, 206402 (2018).
- [126] H. Zhang, J. Zhang, H. Yang, Q. Lan, D. Hong, S. Wang, X. Shen, T. Khan, R. Yu, J. Sun, et al., *Appl. Mater. Interfaces* **8**, 18328 (2016).
- [127] W. S. Choi, J. H. Kwon, H. Jeon, J. E. Hamann-Borrero, A. Radi, S. Macke, R. Sutarto, F. He, G. A. Sawatzky, V. Hinkov, et al., *Nano Lett.* **12**, 4966 (2012).
- [128] J.-H. Kwon, W. S. Choi, Y.-K. Kwon, R. Jung, J.-M. Zuo, H. N. Lee, and M. Kim, *Chem. Mater.* **26**, 2496 (2014).
- [129] N. Biškup, J. Salafranca, V. Mehta, M. P. Oxley, Y. Suzuki, S. J. Pennycook, S. T. Pantelides, and M. Varela, *Phys. Rev. Lett.* **112**, 087202 (2014).
- [130] M. Merz, P. Nagel, C. Pinta, A. Samartsev, H. V. Löhneysen, M. Wissinger, S. Uebe, A. Assmann, D. Fuchs, and S. Schuppler, *Phys. Rev. B* **82**, 174416 (2010).
- [131] A. O. Fumega and V. Pardo, *Phys. Rev. Materials* **1**, 054403 (2017).
- [132] Z. Jiráček, J. Hejtmánek, K. Knížek, and M. Veverka, *Phys. Rev. B* **78**, 014432 (2008).
- [133] J. Wu and C. Leighton, *Phys. Rev. B* **67**, 174408 (2003).
- [134] K. Knížek, Z. Jiráček, J. Hejtmánek, and P. Novák, *J. Magn. Magn. Mater.* **322**, 1221 (2010).
- [135] K. Muta, Y. Kobayashi, and K. Asai, *J. Phys. Soc. Jpn.* **71**, 2784 (2002).
- [136] S. Tsubouchi, T. Kyômen, M. Itoh, P. Ganguly, M. Oguni, Y. Shimojo, Y. Morii, and Y. Ishii, *Phys. Rev. B* **66**, 052418 (2002).

- [137] S. Tsubouchi, T. Kyômen, M. Itoh, and M. Oguni, *Phys. Rev. B* **69**, 144406 (2004).
- [138] J. Hejtmánek, E. Šantavá, K. Knížek, M. Maryško, Z. Jirák, T. Naito, H. Sasaki, and H. Fujishiro, *Phys. Rev. B* **82**, 165107 (2010).
- [139] J. C. Zahner and H. G. Drickamer, *J. Chem. Phys.* **35**, 1483 (1961).
- [140] M. E. Lines, *Phys. Rev.* **137**, A982 (1965).
- [141] C. A. Ramos, A. R. King, and V. Jaccarino, *Phys. Rev. B* **40**, 7124 (1989).
- [142] J. A. Barreda-Argüeso, S. López-Moreno, M. N. Sanz-Ortiz, F. Aguado, R. Valiente, J. González, F. Rodríguez, A. H. Romero, A. Muñoz, L. Nataf, et al., *Phys. Rev. B* **88**, 214108 (2013).
- [143] J. A. Barreda-Argüeso, F. Aguado, J. González, R. Valiente, L. Nataf, M. N. Sanz-Ortiz, and F. Rodríguez, *J. Phys. Chem. C* **120**, 18788 (2016).
- [144] J. Zaanen, G. A. Sawatzky, and J. W. Allen, *Phys. Rev. Lett.* **55**, 418 (1985).
- [145] R. W. G. Wyckoff, *Crystal Structures* (John Wiley, New York, 1963).
- [146] J. W. Stout and S. A. Reed, *J. Am. Chem. Soc.* **76**, 5279 (1954).
- [147] M. M. R. Costa, J. A. Paixão, M. J. M. de Almeida, and L. C. R. Andrade, *Acta Cryst.* **B49**, 591 (1993).
- [148] L. G. van Uitert, H. J. Williams, R. C. Sherwood, and J. J. Rubin, *J. Appl. Phys.* **36**, 1029 (1965).
- [149] R. Newman and R. M. Chrenko, *Phys. Rev.* **115**, 1147 (1959).
- [150] K. Okada and A. Kotani, *J. Phys. Soc. Jpn.* **61**, 4619 (1992).
- [151] A. Kikas, R. Ruus, A. Saar, E. Nõmmiste, T. Käämbre, and S. Sundin, *J. Electron Spectrosc. Relat. Phenom.* **103**, 745 (1999).
- [152] G. van der Laan, J. Zaanen, G. A. Sawatzky, R. Karnatak, and J.-M. Esteva, *Phys. Rev. B* **33**, 4253 (1986).
- [153] G. van der Laan, J. Zaanen, G. A. Sawatzky, R. Karnatak, and J.-M. Esteva, *Solid State Commun.* **56**, 673 (1985).
- [154] V. Kinsinger, R. Zimmermann, S. Hüfner, and P. Steiner, *Z. Phys. B: Condens. Matter* **89**, 21 (1992).

- [155] J. W. Stout and E. Catalano, *Phys. Rev.* **92**, 1575 (1953).
- [156] E. Catalano and J. W. Stout, *J. Chem. Phys.* **23**, 1803 (1955).
- [157] P. Martel, R. A. Cowley, and R. W. H. Stevenson, *J. Appl. Phys.* **39**, 1116 (1968).
- [158] J. Stremper, U. Rütt, S. P. Bayrakci, T. Brückel, and W. Jauch, *Phys. Rev. B* **69**, 014417 (2004).
- [159] M. K. Wilkinson, J. W. Cable, E. O. Wollan, and W. C. Koehler, *Phys. Rev.* **113**, 497 (1959).
- [160] J. W. Stout and L. M. Matarrese, *Rev. Mod. Phys.* **25**, 338 (1953).
- [161] P. G. Russell, D. S. McClure, and J. W. Stout, *Phys. Rev. Lett.* **16**, 176 (1966).
- [162] C. A. Ramos, D. Lederman, A. R. King, and V. Jaccarino, *Phys. Rev. Lett.* **65**, 2913 (1990).
- [163] D. J. Lockwood, G. Mischler, M. C. Schmidt, and I. W. Johnstone, *J. Phys. C: Solid State Phys.* **12**, 1955 (1979).
- [164] R. M. Macfarlane, *Phys. Rev. Lett.* **25**, 1454 (1970).
- [165] R. F. Blunt, *J. Chem. Phys.* **44**, 2317 (1966).
- [166] L. J. Zimring and J. W. Stout, *J. Chem. Phys.* **51**, 4197 (1969).
- [167] J. Ferguson, D. L. Wood, and K. Knox, *J. Chem. Phys.* **39**, 881 (1963).
- [168] K. E. Lawson, *J. Chem. Phys.* **44**, 4159 (1966).
- [169] J. T. Hougen, G. E. Leroi, and T. C. James, *J. Chem. Phys.* **34**, 1670 (1961).
- [170] E. C. Hsu and J. W. Stout, *J. Chem. Phys.* **59**, 502 (1973).
- [171] J. C. Christie, I. W. Johnstone, G. D. Jones, and K. Zdansky, *Phys. Rev. B* **12**, 4656 (1975).
- [172] J. Jiménez-Mier, G. M. Herrera-Pérez, P. Olalde-Velasco, D. L. Ederer, and T. Schuler, *Rev. Mex. Fis.* **54**, 30 (2008).
- [173] Y. Tamenori, *J. Synchrotron Radiat.* **20**, 419 (2013).

- [174] D. K. Bora, X. Cheng, M. Kapilashrami, P. A. Glans, Y. Luo, and J.-H. Guo, *J. Synchrotron Radiat.* **22**, 1450 (2015).
- [175] F. M. F. de Groot, *Coord. Chem. Rev.* **249**, 31 (2005).
- [176] S. M. Butorin, D. C. Mancini, J.-H. Guo, N. Wassdahl, J. Nordgren, M. Nakazawa, S. Tanaka, T. Uozumi, A. Kotani, Y. Ma, et al., *Phys. Rev. Lett.* **77**, 574 (1996).
- [177] G. Ghiringhelli, M. Matsubara, C. Dallera, F. Fracassi, R. Gusmeroli, A. Piazzalunga, A. Tagliaferri, N. B. Brookes, A. Kotani, and L. Braicovich, *J. Phys. Condens. Matter* **17**, 5397 (2005).
- [178] A. Kotani, M. Matsubara, T. Uozumi, G. Ghiringhelli, F. Fracassi, C. Dallera, A. Tagliaferri, N. B. Brookes, and L. Braicovich, *Radiat. Phys. Chem.* **75**, 1670 (2006).
- [179] M. Matsubara, T. Uozumi, A. Kotani, and J. C. Parlebas, *J. Phys. Soc. Jpn.* **74**, 2052 (2005).
- [180] V. N. Strocov, T. Schmitt, U. Flechsig, T. Schmidt, A. Imhof, Q. Chen, J. Raabe, R. Betemps, D. Zimoch, J. Krempasky, et al., *J. Synchrotron Radiat.* **17**, 631 (2010).
- [181] G. Ghiringhelli, A. Piazzalunga, X. Wang, A. Bendounan, H. Berger, F. Bottegoni, N. Christensen, C. Dallera, M. Grioni, J. C. Grivel, et al., *Eur. Phys. J. Special Topics* **169**, 199 (2009).
- [182] E. Z. Kurmaev, A. L. Ankudinov, J. J. Rehr, L. D. Finkelstein, P. F. Karimov, and A. Moewesc, *J. Electron Spectrosc. Relat. Phenom.* **148**, 1 (2005).
- [183] X. Meng, J. Deng, J. Zhu, H. Bi, E. Kan, and X. Wang, *Sci. Rep.* **6**, 21717 (2016).
- [184] F. Tao, Y.-Q. Zhao, G.-Q. Zhang, and H.-L. Li, *Electrochem. Commun.* **9**, 1282 (2007).
- [185] N. Kornienko, J. Resasco, N. Becknell, C.-M. Jiang, Y.-S. Liu, K. Nie, X. Sun, J. Guo, S. R. Leone, and P. Yang, *J. Am. Chem. Soc.* **137**, 7448 (2015).
- [186] D. Merki, S. Fierro, H. Vrubel, and X. Hu, *Chem. Sci.* **2**, 1262 (2011).
- [187] M. S. Faber, K. Park, M. Cabán-Acevedo, P. K. Santra, and S. Jin, *J. Phys. Chem. Lett.* **4**, 1843 (2013).

- [188] C. Sugiura, Y. Gohshi, and I. Suzuki, *Phys. Rev. B* **10**, 338 (1974).
- [189] B. D. McCloskey, A. Valery, A. C. Luntz, S. R. Gowda, G. M. Wallraff, J. M. Garcia, T. Mori, and L. E. Krupp, *J. Phys. Chem. Lett.* **4**, 2989 (2013).
- [190] J. C. Fuggle and N. Mårtensson, *J. Electron Spectrosc. Relat. Phenom.* **21**, 275 (1980).
- [191] G. Ghiringhelli, A. Piazzalunga, C. Dallera, G. Trezzi, L. Braicovich, T. Schmitt, V. N. Strocov, R. Betemps, L. Patthey, X. Wang, et al., *Rev. Sci. Instrum.* **77**, 113108 (2006).
- [192] M. M. van Schooneveld and S. DeBeer, *J. Electron Spectrosc. Relat. Phenom.* **198**, 31 (2015).
- [193] R. J. Green, D. A. Zatsepin, D. J. St. Onge, E. Z. Kurmaev, N. V. Gavrilov, A. F. Zatsepin, and A. Moewes, *J. Appl. Phys.* **115**, 103708 (2014).
- [194] P. W. Anderson, *Phys. Rev.* **124**, 41 (1961).
- [195] R. D. Cowan, *J. Opt. Soc. Am.* **149**, 295 (1968).
- [196] B. T. Thole, G. van der Laan, and P. H. Butler, *Chem. Phys. Lett.* **149**, 295 (1988).
- [197] R. J. Green, *PhD Thesis* (University of Saskatchewan, 2013).
- [198] E. Stavitski and F. M. F. de Groot, *Micron* **41**, 687 (2010).
- [199] P. Glatzel, *Computer Code* (European Synchrotron Radiation Facility, Grenoble, France., 2012).
- [200] M. U. Delgado-Jaime, J. Zhang, K.; Vura-Weis, and F. M. F. de Groot, *J. Synchrotron Rad.* **23**, 1264 (2016).
- [201] S. P. Cramer, F. M. F. de Groot, Y. Ma, C. T. Chen, F. Sette, C. A. Kipke, D. M. Eichhorn, M. K. Chan, W. H. Armstrong, E. Libby, et al., *J. Am. Chem. Soc.* **113**, 7937 (1991).
- [202] M. W. Haverkort, M. Zwierzycki, and O. K. Andersen, *Phys. Rev. B* **85**, 165113 (2012).
- [203] F. M. F. de Groot, M. A. Arrio, P. Sainctavit, C. Carrier, and C. T. Chen, *Solid State Comm.* **92**, 991 (1994).

- [204] F. M. F. de Groot, R. Ruus, and M. Elango, *Phys. Rev. B* **51**, 14062 (1995).
- [205] M. O. Krause and J. H. Oliver, *J. Phys. Chem. Ref. Data* **8**, 329 (1979).
- [206] E. C. Wasinger, F. M. F. de Groot, B. Hedman, K. O. Hodgson, and E. I. Solomon, *J. Am. Chem. Soc.* **125**, 12894 (2003).
- [207] P. S. Miedema, F. Borgatti, F. Offi, G. Panaccione, and F. M. F. de Groot, *J. Electron Spectrosc. Relat. Phenom.* **203**, 8 (2015).
- [208] E. Z. Kurmaev, J. A. McLeod, A. Buling, N. A. Skorikov, A. Moewes, M. Neumann, M. A. Korotin, Y. A. Izyumov, N. Ni, and P. C. Canfield, *Phys. Rev. B* **80**, 054508 (2009).
- [209] E. Z. Kurmaev, J. A. McLeod, N. A. Skorikov, L. D. Finkelstein, A. Moewes, Y. A. Izyumov, and C. S., *J. Phys. Condens. Matter* **21**, 345701 (2009).
- [210] J. A. McLeod, A. Buling, R. J. Green, T. D. Boyko, N. A. Skorikov, E. Z. Kurmaev, M. Neumann, L. D. Finkelstein, N. Ni, A. Thaler, et al., *J. Phys. Condens. Matter* **24**, 215501 (2012).
- [211] J.-Q. Yan, J. S. Zhou, and J. B. Goodenough, *Phys. Rev. B.* **69**, 134409 (2004).
- [212] L. Qiao, J. H. Jang, D. J. Singh, Z. Gai, H. Xiao, A. Mehta, R. K. Vasudevan, A. Tselev, Z. Feng, H. Zhou, et al., *Nano Lett.* **15**, 4677 (2015).
- [213] R.-P. Wang, B. Liu, R. J. Green, M. U. Delgado-Jaime, M. Ghiasi, T. Schmitt, M. M. van Schooneveld, and F. M. F. de Groot, *J. Phys. Chem. C* **121**, 24919 (2017).
- [214] R.-P. Wang, A. Hariki, A. Sotnikov, F. Frati, J. Okamoto, H. Y. Huang, A. Singh, D. J. Huang, K. Tomiyasu, C. H. Du, et al., *Phys. Rev. B* **98**, 035149 (2018).
- [215] A. Harada, T. Taniyama, Y. Takeuchi, T. Sato, T. Kyômen, and M. Itoh, *Phys. Rev. B* **75**, 184426 (2007).
- [216] H. Gercek, *Int. J. Rock Mech. Min. Sci.* **44**, 1 (2007).
- [217] A. Herklotz, A. D. Rata, L. Schultz, and K. Dörr, *Phys. Rev. B* **79**, 092409 (2009).

- [218] A. D. Rata, A. Herklotz, L. Schultz, and K. Dörr, *Eur. Phys. J. B* **76**, 215 (2010).
- [219] M. Khalid, A. Setzer, M. Ziese, P. Esquinazi, D. Spemann, A. Pöpl, and E. Goering, *Phys. Rev. B* **81**, 214414 (2010).
- [220] O. Lobacheva, M. Chavarha, Y. M. Yiu, T. K. Sham, and L. V. Goncharova, *J. Appl. Phys* **116**, 013901 (2014).
- [221] H. Gretarsson, J. P. Clancy, Y. Singh, P. Gegenwart, J. P. Hill, J. Kim, M. H. Upton, A. H. Said, D. Casa, T. Gog, et al., *Phys. Rev. B* **87**, 220407 (2013).
- [222] G. E. Sterbinsky, R. Nanguneri, J. X. Ma, J. Shi, E. Karapetrova, J. C. Woicik, H. Park, J.-W. Kim, and P. J. Ryan, *Phys. Rev. Lett.* **120**, 197201 (2018).
- [223] J. Jaklevic, J. A. Kirby, M. P. Klein, A. S. Robertson, G. S. Brown, and P. Eisenberger, *Solid State Commun.* **23**, 679 (1977).
- [224] E. Zschech, L. Tröger, D. Arvanitis, H. Michaelis, U. Grimm, and K. Baberschke, *Solid State Commun.* **82**, 1 (1992).
- [225] L. Tröger, D. Arvanitis, K. Baberschke, H. Michaelis, U. Grimm, and E. Zschech, *Phys. Rev. B* **46**, 3283 (1992).
- [226] S. Eisebitt, T. Böske, J.-E. Rubensson, and W. Eberhardt, *Phys. Rev. B* **47**, 14103 (1993).
- [227] V. Chakarian, Y. U. Idzerda, and C. T. Chen, *Phys. Rev. B* **57**, 5312 (1998).
- [228] R. Nakajima, J. Stöhr, and Y. U. Idzerda, *Phys. Rev. B* **59**, 6421 (1999).
- [229] A. J. Achkar, T. Z. Regier, H. Wadati, Y.-J. Kim, H. Zhang, and D. G. Hawthorn, *Phys. Rev. B* **83**, 081106 (2011).
- [230] J. Luo, G. T. Trammell, and J. P. Hannon, *Phys. Rev. Lett.* **71**, 287 (1993).
- [231] A. Juhin, C. Brouder, and F. de Groot, *Cent. Eur. J. Phys.* **12**, 323 (2014).
- [232] B. Liu, E. N. Glass, R. Wang, Y. Cui, Y. Harada, D. J. Huang, S. Schuppler, C. L. Hill, and F. M. F. de Groot, *Phys. Chem. Chem. Phys.* **20**, 4554 (2018).
- [233] M. W. Haverkort, N. Hollmann, I. P. Krug, and A. Tanaka, *Phys. Rev. B* **82**, 094403 (2010).

- [234] J. J. Lee, B. Moritz, W. S. Lee, M. Yi, C. J. Jia, A. P. Sorini, K. Kudo, Y. Koike, K. J. Zhou, C. Monney, et al., *Phys. Rev. B* **89**, 041104 (2014).
- [235] P. Merchant, B. Normand, K. W. Krämer, M. Boehm, D. F. McMorrow, and C. Rüegg, *Nat. Phys.* **10**, 373 (2014).
- [236] J. F. Afonso and J. Kuneš, *Phys. Rev. B* **95**, 115131 (2017).
- [237] J. Kuneš and P. Augustinský, *Phys. Rev. B* **90**, 235112 (2014).
- [238] T. Yamaguchi, K. Sugimoto, and Y. Ohta, *J. Phys. Soc. Jpn.* **86**, 043701 (2017).
- [239] A. Chainani, M. Mathew, and D. D. Sarma, *Phys. Rev. B* **46**, 9976 (1992).
- [240] T. Arima, Y. Tokura, and J. B. Torrance, *Phys. Rev. B* **48**, 17006 (1993).
- [241] S. Yamaguchi, Y. Okimoto, H. Taniguchi, and Y. Tokura, *Phys. Rev. B* **53**, R2926 (1996).
- [242] T. Sommer, M. Vojta, and K. W. Becker, *Eur. Phys. J. B* **23**, 329 (2001).
- [243] P. Blaha, K. Schwarz, G. Madsen, D. Kvasnicka, and J. Luitz, *WIEN2k, An Augmented Plane Wave + Local Orbitals Program for Calculating Crystal Properties (Karlheinz Schwarz, Techn. Universitat Wien, Austria, 2001), ISBN 3-9501031-1-2* (2008).
- [244] J. Kuneš, R. Arita, P. Wissgott, A. Toschi, H. Ikeda, and K. Held, *Comput. Phys. Commun.* **181**, 1888 (2010).
- [245] A. A. Mostofi, J. R. Yates, G. Pizzi, Y.-S. Lee, I. S., D. Vanderbilt, and N. Marzari, *Comput. Phys. Commun.* **185**, 2309 (2014).
- [246] J. R. Schrieffer and P. A. Wolff, *Phys. Rev.* **149**, 491 (1966).
- [247] J. F. Afonso, A. Sotnikov, and J. Kuneš, *J. Phys. Condens. Matter* **30**, 135603 (2018).
- [248] F. M. F. de Groot, P. Kuiper, and G. A. Sawatzky, *Phys. Rev. B* **57**, 14584 (1998).
- [249] M. Karolak, M. Izquierdo, S. L. Molodtsov, and A. I. Lichtenstein, *Phys. Rev. Lett.* **115**, 046401 (2015).
- [250] G. Khaliullin, *Phys. Rev. Lett.* **111**, 197201 (2013).

- [251] A. Hariki, M. Winder, and J. Kuneš, *Phys. Rev. Lett.* **121**, 126403 (2018).
- [252] J. Chen, X. Wu, and A. Selloni, *Phys. Rev. B* **83**, 245204 (2011).
- [253] M. Maryško, Z. Jiráček, K. Knížek, P. Novák, J. Hejtmánek, T. Naito, H. Sasaki, and H. Fujishiro, *J. Appl. Phys.* **109**, 07E127 (2011).
- [254] S. Lee, Y. H. Matsuda, T. Naito, D. Nakamura, and S. Takeyama, *J. Phys. Soc. Jpn.* **84**, 044703 (2015).
- [255] J. L. García-Muñoz, C. Frontera, A. J. Barón-González, S. Valencia, J. Blasco, R. Feyerherm, E. Dudzik, R. Abrudan, and F. Radu, *Phys. Rev. B* **84**, 045104 (2011).
- [256] H. Fujishiro, T. Naito, D. Takeda, N. Yoshida, T. Watanabe, K. Nitta, J. Hejtmánek, K. Knížek, and Z. Jiráček, *Phys. Rev. B* **87**, 155153 (2013).
- [257] H. Fujishiro, Y. Noda, K. Akuzawa, T. Naito, A. Ito, T. Goto, M. Maryško, Z. Jiráček, J. Hejtmánek, and K. Nitta, *J. Appl. Phys.* **121**, 115104 (2017).
- [258] F. Guillou, K. Kummer, Y. Bréard, L. Hervé, and V. Hardy, *Phys. Rev. B* **95**, 174445 (2017).
- [259] J. Hejtmánek, Z. Jiráček, O. Kaman, K. Knížek, E. Šantavá, K. Nitta, T. Naito, and H. Fujishiro, *Eur. Phys. J. B* **86**, 305 (2013).
- [260] A. Ikeda, S. Lee, T. T. Terashima, Y. H. Matsuda, M. Tokunaga, and T. Naito, *Phys. Rev. B* **94**, 115129 (2016).
- [261] Z. Hu, H. Wu, M. W. Haverkort, H. H. Hsieh, H. J. Lin, T. Lorenz, J. Baier, A. Reichl, I. Bonn, C. Felser, et al., *Phys. Rev. Lett.* **92**, 207402 (2004).
- [262] V. Kumar, R. Kumar, D. K. Shukla, S. K. Arora, I. V. Shvets, K. Singh, and R. Kumar, *Mater. Chem. Phys.* **147**, 617 (2014).
- [263] A. Sotnikov and J. Kuneš, *Phys. Rev. B* **96**, 245102 (2017).
- [264] M. Gibert, P. Zubko, R. Scherwitzl, J. Íñiguez, and J. Triscone, *Nat. Mater.* **11**, 195 (2012).
- [265] J. E. Kleibecker, Z. Zhong, H. Nishikawa, J. Gabel, A. Müller, F. Pfaff, M. Sing, K. Held, R. Claessen, G. Koster, et al., *Phys. Rev. Lett.* **113**, 237402 (2014).

- [266] N. B. Brookes, F. Yakhou-Harris, K. Kummer, A. Fondacaro, J. C. Cezar, D. Betto, E. Velez-Fort, A. Amorese, G. Ghiringhelli, L. Braicovich, et al., *Nucl. Instrum. Methods A* **903**, 175 (2018).
- [267] J. Dvorak, I. Jarrige, V. Bisogni, S. Coburn, and W. Leonhardt, *Rev. Sci. Instrum.* **87**, 115109 (2016).
- [268] I21, Daimond Light Source.
- [269] Y. Y. Peng, E. W. Huang, R. Fumagalli, M. Minola, Y. Wang, X. Sun, Y. Ding, K. Kummer, X. J. Zhou, N. B. Brookes, et al., *Phys. Rev. B* **98**, 144507 (2018).
- [270] D. Betto, Y. Y. Peng, S. B. Porter, G. Berti, A. Calloni, G. Ghiringhelli, and N. B. Brookes, *Phys. Rev. B* **96**, 020409 (2017).
- [271] J. Norell, R. M. Jay, M. Hantschmann, S. Eckert, M. Guo, K. J. Gaffney, P. Wernet, M. Lundberg, A. Föhlisch, and M. Odelius, *Phys. Chem. Chem. Phys.* **20**, 7243 (2018).
- [272] B. Liu, M. M. van Schooneveld, Y.-T. Cui, J. Miyawaki, Y. Harada, T. O. Eschemann, K. P. de Jong, M. U. Delgado-Jaime, and F. M. F. de Groot, *J. Phys. Chem. C* **121**, 17450 (2017).
- [273] M. Beye, P. Wernet, C. Schüssler-Langeheine, and A. Föhlisch, *J. Electron Spectrosc. Relat. Phenom.* **188**, 172 (2013).
- [274] J. Vura-Weis, C.-M. Jiang, C. Liu, H. Gao, J. M. Lucas, F. M. F. de Groot, P. Yang, A. P. Alivisatos, and S. R. Leone, *J. Phys. Chem. Lett.* **4**, 3667 (2013).
- [275] M. P. M. Dean, Y. Cao, X. Liu, S. Wall, D. Zhu, R. Mankowsky, V. Thampy, X. M. Chen, J. G. Vale, D. Casa, et al., *Nat. Mater.* **15**, 601 (2016).
- [276] P. Krüger, *J. Phys. Conference Series* **190**, 012006 (2009).
- [277] I. Josefsson, K. Kunnus, S. Schreck, A. Föhlisch, F. de Groot, P. Wernet, and M. Odelius, *J. Phys. Chem. Lett.* **3**, 3565 (2012).
- [278] J. Lüder, J. Schött, B. Brena, M. W. Haverkort, P. Thunström, O. Eriksson, B. Sanyal, I. Di Marco, and Y. O. Kvashnin, *Phys. Rev. B* **96**, 245131 (2017).
- [279] P. Krüger, *Radiat. Phys. Chem.* p. in press (2019).